Electronic supporting information for

A reactivity model for oxidative addition to palladium enables quantitative predictions for catalytic cross-coupling reactions

Jingru Lu, Sofia Donnecke, Irina Paci,* David C. Leitch*

Department of Chemistry, University of Victoria, 3800 Finnerty Rd. Victoria BC, CANADA, V8P 5C2.

*ipaci@uvic.ca; dcleitch@uvic.ca.

Table of Contents

Other Supporting information for this manuscript include the following:

Data S1. (separate file; *.xlsx)
Extended tables in Microsoft Excel format (*.xlsx*) that contain molecular descriptors, predicted $\Delta G^{\ddagger}_{OA}$ calculations, and statistical analysis for multivariate linear regression models.

Data S2. (separate file; *.zip)
Cartesian coordinates files (*.xyz*) for every calculated substrate, palladium complex, phosphine ligand, π-complex intermediate, and transition state. These files are contained in a single *.zip* file, and organized into separate folders.

Data S3. (separate file; *.csv)
Simplified table of comma separated values (*.csv*) that contains molecular descriptors and experimental $\Delta G^{\ddagger}_{OA}$ values for the oxidative addition substrates.

General Considerations

Materials

All solvents, reagents, and organic substrates were used as purchased from commercial suppliers without further purification with the following exceptions. 4-Chloro-6-(piperidin-1-yl)pyrimidine and 4-chloro-6-(pyrrolidin-1-yl)pyrimidine were prepared using published procedures.[1] 4-Chloro-2-methylpyrimidine and 2-Chloro-5-aminopyridine were purified by dissolving the commercial material in THF or chloroform, followed by filtration to remove insoluble impurities; purity of these materials was confirmed by NMR spectroscopy. The 9 aryl triflates were prepared using a published procedure,[2] and the NMR characterization data has been reported in published works.[2-8] Bis(tricyclohexylphosphine)palladium(0) was purchased from Strem Chemicals and used as received. All reactions were performed inside an MBraun glovebox under an N_2 atmosphere.

Analysis and Spectroscopy

All NMR spectra were recorded on either a Bruker AVANCE 300 MHz spectrometer or a Bruker AVANCE NEO 500 MHz spectrometer. All $^{31}P\{^1H\}$ qNMR (quantitative Nuclear Magnetic Resonance) spectra were recorded on the 500 MHZ spectrometer using a $^{31}P\{^1H\}$ NMR parameter set with a relaxation delay (D_1) of 20 s and 64 scans. This delay time was chosen based on the measured T_1 relaxation time for the oxidative addition products generated in a competition reaction between 2-chloro-pyridine and 2-chloro-5-methylpyridine reacting with $Pd(PCy_3)_2$ (Fig. S1). The longest T_1 observed peaks from 0 ppm to 50 ppm was 4.35 s. By setting the delay time D_1 to 20 s and the acquisition time to 1.7 s, there is 5 times the T_1 period between scans to ensure all nuclei giving peaks from 0 ppm to 50 ppm have fully relaxed after each scan. Note that the ^{31}P nuclei from the internal standard triphenylphosphine (dissolved in C_6D_6 in a sealed capillary added to the NMR tube) has a T_1 longer than 13 s; as a result, the signal of PPh_3 has not fully relaxed during a D_1 of 20 s. In our $^{31}P\{^1H\}$ NMR spectroscopy analysis, PPh_3 was only used as a chemical shift standard, and the product ratio in a competition reaction was calculated directly from the peak area ratio of the two oxidative addition products from the ^{31}P qNMR spectrum.

High-resolution electrospray ionization mass spectrometric analysis was performed using a Thermo Scientific Ultimate 3000 ESI-Orbitrap Exactive Plus.

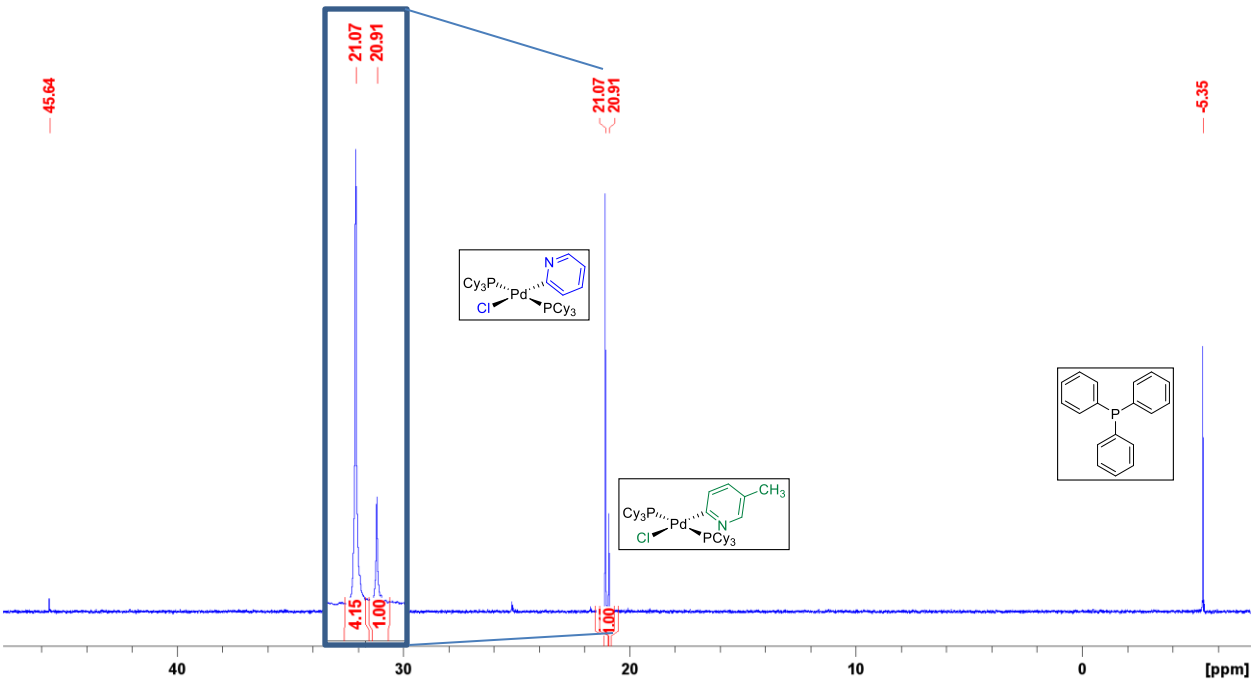

Fig. S1.
$^{31}P\{^{1}H\}$ qNMR spectrum of the competition reaction of 2-chloro-pyridine and 2-chloro-5-methyl-pyridine with $Pd(PCy_3)_2$; T_1 relaxation values were determined for these two Pd species, which was used to inform the delay time setting of 20 s.

Experimental Details for Oxidative Addition Competition Studies

Bis(tricyclohexylphosphine)palladium(0) ($Pd(PCy_3)_2$) was used as the palladium source. A library of 70 (hetero)aryl chlorides and bromides was used as the substrates. THF was used as the reaction solvent. Stock solutions were prepared for each component: the concentration of the substrate stock solutions was 0.375 M, and the concentration of $Pd(PCy_3)_2$ stock solution was 0.0375 M.

To assess each individual (hetero)aryl halide for oxidative addition reactivity in combination with $Pd(PCy_3)_2$ and determine the ^{31}P NMR chemical shift of the resulting Pd(II) product, individual oxidative addition reactions were carried out at room temperature on 1 mL scale. In a 4 mL vial containing a stirbar, an aliquot of the substrate stock solution (400 µL, 0.150 mmol) was diluted with additional reaction solvent (THF, 400 µL), followed by addition of an aliquot of the $Pd(PCy_3)_2$ stock solution (200 µL, 0.00750 mmol). The resulting solution was mixed for 2-18 hours, then a 600 µL sample was transferred to an NMR tube containing a capillary filled with PPh_3 in C_6D_6. A $^{31}P\{^{1}H\}$ NMR spectrum was recorded to confirm the oxidative addition reaction occurred and went to completion, and to identify the ^{31}P chemical shift of the oxidative addition product. The reaction progress was determined after 2 hours by NMR analysis of an aliquot of the solution. If not complete, the remaining reaction solution was stirred overnight for a total reaction time of at least 18 hours before $^{31}P\{^{1}H\}$ NMR analysis.

Competition experiments were performed to obtain the relative activation energies ($\Delta\Delta G^{\ddagger}_{OA}$) between two substrates in palladium oxidative addition (Fig. S2). All reactions were conducted at room temperature on 1 mL scale under *pseudo* first-order conditions by adding the two substrates

in excess but equal amount (0.150 mmol, 1.0 equivalent) to compete with one palladium source (0.0750 mmol, 0.05 equivalent). In order to accurately measure the oxidative addition product ratio in a competition reaction, the ^{31}P NMR chemical shifts of the products must differ by at least 0.1 ppm; appropriate resolution was confirmed prior to competition experiment set-up by comparing the chemical shifts obtained in the aforementioned individual oxidative addition experiments. The competition reactions were prepared similarly to the individual oxidative addition experiments, with 400 µL of each substrate stock solution and 200 µL of $Pd(PCy_3)_2$ stock solution mixed in a small vial. The initial concentration of each substrate was 0.150 M, and the initial concentration of $Pd(PCy_3)_2$ was 0.00750 M. After mixing the reaction solution for 2-18 hours, ^{31}P qNMR spectra were recorded to measure the peak area ratio between two oxidative addition products.

The competition experiments listed in Table S1, entries 92-95 were performed between an aryl bromide and an aryl triflate. Stock solution of tetrabutylammonium was prepared and the concentration was 0.075 M. After mixing the reaction solution for 2 hours, 300 µL of the tetrabutylammonium bromide was added and the reaction solution was stirred for 20 minutes before NMR analysis. Excess amount of tetrabutylammonium bromide was added to convert the oxidative addition product of Pd(II)-triflate species into Pd(II)-bromide species (Fig. S2). Because the Pd(II) oxidative addition product of 4-cyano phenyl triflate is not soluble in THF, stock solution of tetrabutylammonium bromide was also added into the competition reaction mixture that involves 4-cyano phenyl triflate (Table S1, entry 96).

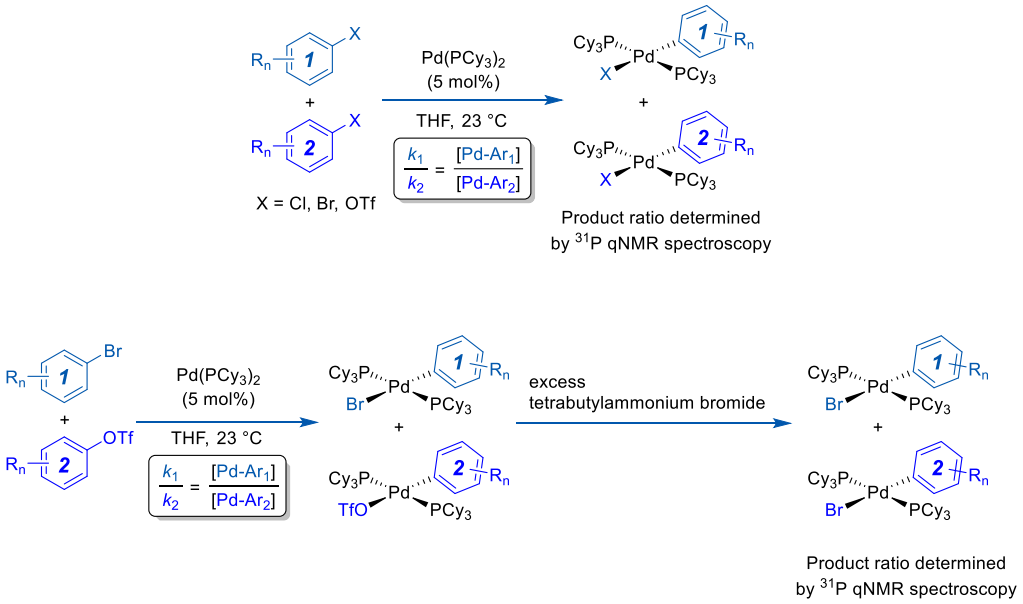

Fig. S2.
Top: General competition experiment design. *Bottom*: Specific design of competition experiments between an aryl bromide and an aryl triflate.

Table S1 contains the ^{31}P NMR chemical shifts and peak area ratios of 98 competition reactions performed with 79 substrates in THF. All ^{31}P NMR chemical shifts are referenced to triphenylphosphine (-6.00 ppm) as an internal chemical shift standard.

Table S1.
^{31}P NMR chemical shifts and the peak area ratios of 98 competition reactions in THF.

Exp No.	Substrate A	^{31}P NMR δ (ppm)	Substrate B	^{31}P NMR δ (ppm)	Peak area ratio[a]
1	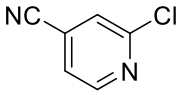 2-chloro-4-cyanopyridine	21.4	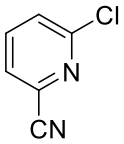 2-chloro-6-cyanopyridine	20.9	4.11
2	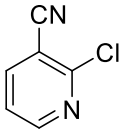 2-chloro-3-cyanopyridine	21.3	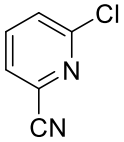 2-chloro-6-cyanopyridine	20.9	6.16
3	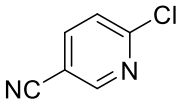 2-chloro-5-cyanopyridine	20.1	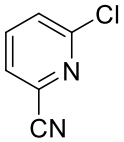 2-chloro-6-cyanopyridine	20.9	12.63
4	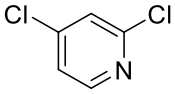 2,4-dichloropyridine	21.1	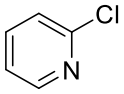 2-chloropyridine	20.5	22.17
5	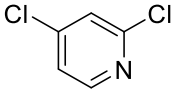 2,4-dichloropyridine	21.1	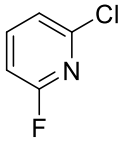 2-chloro-6-fluoropyridine	20.8	25.86
6	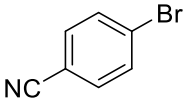 4-bromobenzonitrile	20.1	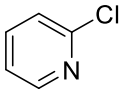 2-chloropyridine	20.5	25.88
7	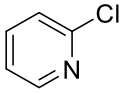 2-chloropyridine	20.5	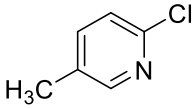 2-chloro-5-methylpyridine	20.3	4.15
8	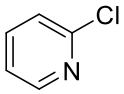 2-chloropyridine	20.4	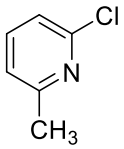 2-chloro-6-methylpyridine	19.8	12.00

9	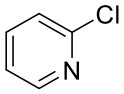 2-chloropyridine	20.5	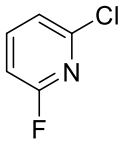 2-chloro-6-fluoropyridine	20.8	1.20
10	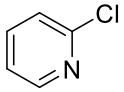 2-chloropyridine	20.5	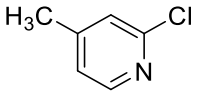 2-chloro-4-methylpyridine	20.7	2.79
11	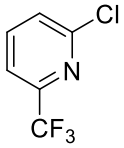 2-chloro-6-trifluoromethyl pyridine	21.3	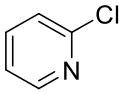 2-chloropyridine	20.4	1.71
12	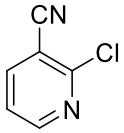 2-chloro-3-cyanopyridine	21.3	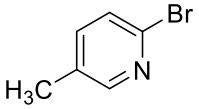 2-bromo-5-methylpyridine	19.3	8.83
13	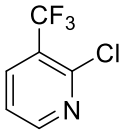 2-chloro-3-trifluoromethyl pyridine	18.5	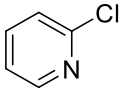 2-chloropyridine	20.5	2.84
14	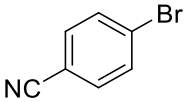 4-bromobenzonitrile	20.1	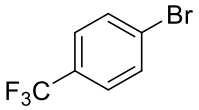 1-bromo-4-trifluoromethyl benzene	19.9	7.93
15	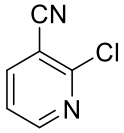 2-chloro-3-cyanopyridine	21.3	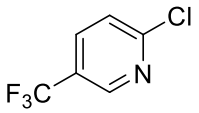 2-chloro-5-trifluoromethyl pyridine	20.9	4.05
16	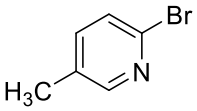 2-bromo-5-methylpyridine	19.3	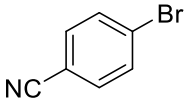 4-bromobenzonitrile	20.1	6.66
17	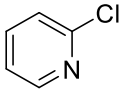 2-chloropyridine	20.5	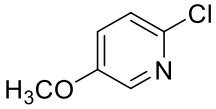 2-chloro-5-methoxy pyridine	20.7	20.06

18	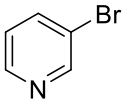 2-bromopyridine	19.5	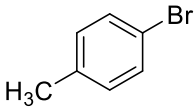 2-bromo-5-methylpyridine	19.3	3.02
19	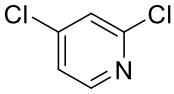 2,4-dichloropyridine	21.1	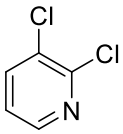 2,3-dichloropyridine	20.8	1.60
20	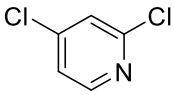 2,4-dichloropyridine	21.1	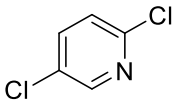 2,5-dichloropyridine	20.8	3.19
21	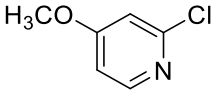 2-chloro-4-methoxy pyridine	20.3	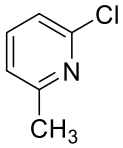 2-chloro-6-methylpyridine	19.7	2.50
22	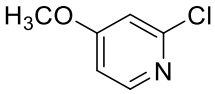 2-chloro-4-methoxy pyridine	20.4	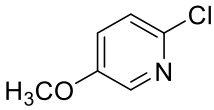 2-chloro-5-methoxy pyridine	20.7	4.25
23	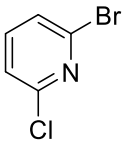 2-bromo-6-chloropyridine	19.6	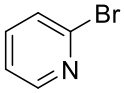 2-bromopyridine	19.4	6.51
24	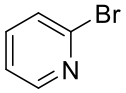 2-bromopyridine	19.4	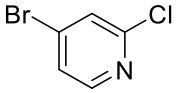 4-bromo-2-chloropyridine	20.2	1.24
25	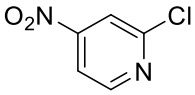 2-chloro-4-nitropyridine	21.5	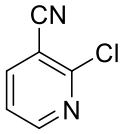 2-chloro-3-cyanopyridine	21.3	1.61
26	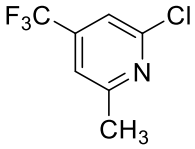 2-chloro-4-trifluoromethyl -6-methylpyridine	20.7	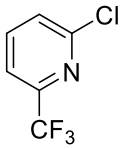 2-chloro-6-trifluoromethyl pyridine	21.3	5.02
27	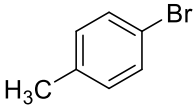 4-bromotoluene	19.5	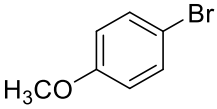 4-bromoanisole	19.8	1.73

28	 2-chloro-3-fluoropyridine	22.7	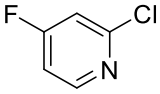 2-chloro-4-fluoropyridine	20.9	7.45
29	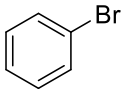 bromobenzene	19.6	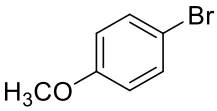 4-bromoanisole	19.8	3.13
30	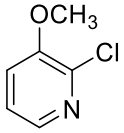 2-chloro-3-methoxy pyridine	21.3	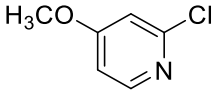 2-chloro-4-methoxy pyridine	20.4	13.04
31	 2-chloro-3-fluoropyridine	22.7	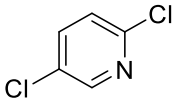 2,5-dichloropyridine	20.8	7.07
32	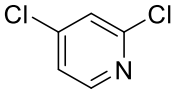 2,4-dichloropyridine	21.1	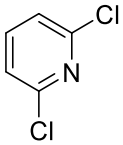 2,6-dichloropyridine	20.6	3.08
33	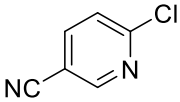 2-chloro-5-cyanopyridine	21.05	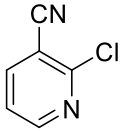 2-chloro-3-cyanopyridine	21.25	2.33
34	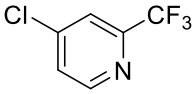 4-chloro-2-trifluoromethyl pyridine	21.25	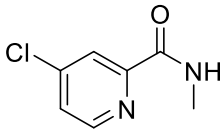 N-Methyl-4-chloropyridine-2-carboxamide	20.85	4.54
35	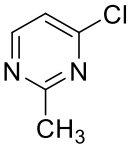 4-chloro-2-methyl-pyrimidine	20.05	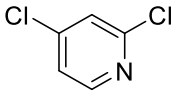 2,4-dichloropyridine	21.05	5.88
36	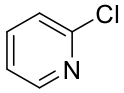 2-chloropyridine	20.45	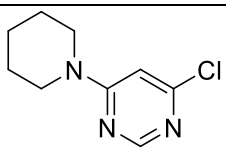 4-Chloro-6-(piperidin-1-yl) pyrimidine	20.05	2.50

37	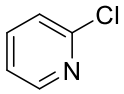 2-chloropyridine	20.45	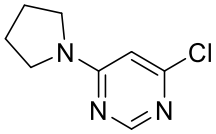 4-Chloro-6-(pyrrolidin-1-yl) pyrimidine	19.95	3.84
38	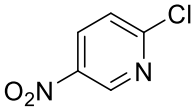 2-chloro-5-nitropyridine	21.25	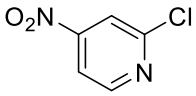 2-chloro-4-nitropyridine	21.55	8.15
39	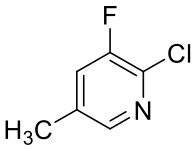 2-chloro-3-fluoro-5-methyl pyridine	22.55	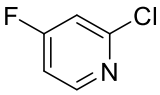 2-chloro-4-fluoropyridine	20.85	1.52
40	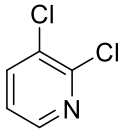 2,3-dichloropyridine	20.75	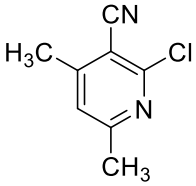 2-chloro-3-cyano-4,6-dimethylpyridine	20.45	2.35
41	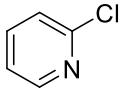 2-chloropyridine	20.45	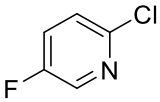 2-chloro-5-fluoropyridine	20.85	1.53
42	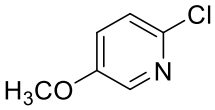 2-chloro-5-methoxypyridine	20.65	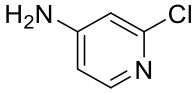 2-chloro-4-aminopyridine	20.05	9.44
43	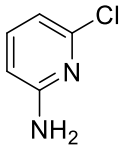 2-chloro-6-aminopyridine	19.45	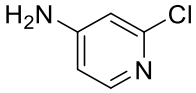 2-chloro-4-aminopyridine	20.05	1.23
44	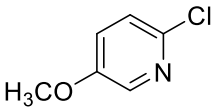 2-chloro-5-methoxypyridine	20.65	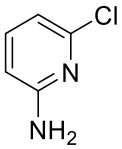 2-chloro-6-aminopyridine	19.45	7.21
45	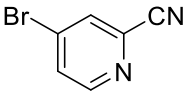 4-bromo-2-cyanopyridine	20.4	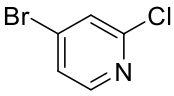 4-bromo-2-chloropyridine	20.2	7.31

46	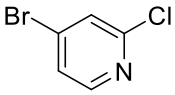 4-bromo-2-chloropyridine	20.2	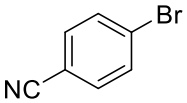 4-bromobenzonitrile	20.1	15.44
47	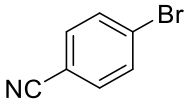 4-bromobenzonitrile	20.0	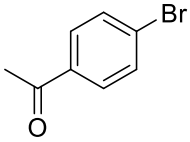 4-bromoacetophenone	19.8	4.96
48	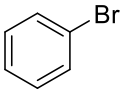 bromobenzene	19.7	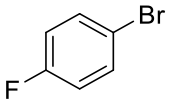 1-bromo-4-fluorobenzene	19.9 (d)	1.03
49	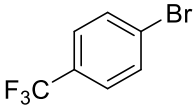 1-bromo-4-trifluoromethyl benzene	19.9	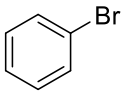 bromobenzene	19.6	19.20
50	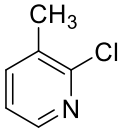 2-chloro-3-methylpyridine	20.7	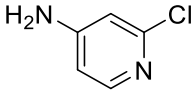 2-chloro-4-aminopyridine	20.1	7.46
51	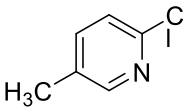 2-chloro-5-methylpyridine	20.3	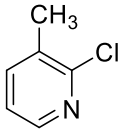 2-chloro-3-methylpyridine	20.7	5.41
52	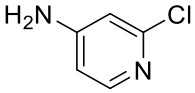 2-chloro-4-aminopyridine	20.1	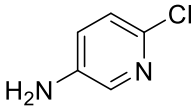 2-chloro-5-aminopyridine	20.2	1.72
53	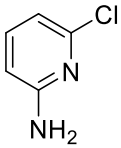 2-chloro-6-aminopyridine	19.5	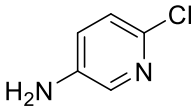 2-chloro-5-aminopyridine	20.2	1.85
54	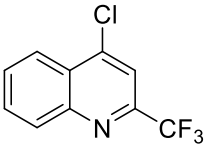 4-chloro-2-trifluoromethyl quinoline	21.6	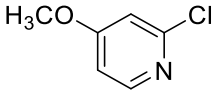 2-chloro-4-methoxypyridine	20.4	3.72

55	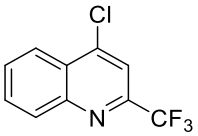 4-chloro-2-trifluoromethylquinoline	21.6	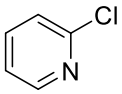 2-chloropyridine	20.5	1.08
56	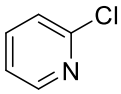 2-chloropyridine	20.5	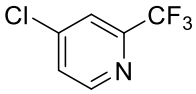 4-chloro-2-trifluoromethyl pyridine	21.4	2.22
57	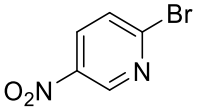 2-bromo-5-nitropyridine	20.2	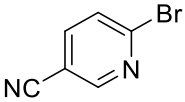 2-bromo-5-cyanopyridine	20.0	1.15
58	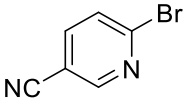 2-bromo-5-cyanopyridine	20.0	 2-bromo-3-cyanopyridine	20.3	2.89
59	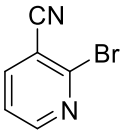 2-bromo-3-cyanopyridine	20.3	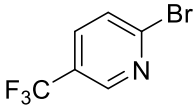 2-bromo-5-trifluoromethyl pyridine	19.9	1.15
60	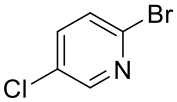 2-bromo-5-chloropyridine	19.8	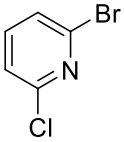 2-bromo-6-chloropyridine	19.6	1.06
61	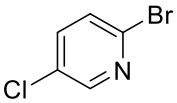 2-bromo-5-chloropyridine	19.8	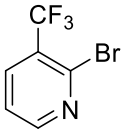 2-bromo-3-trifluoromethyl pyridine	17.7 (d)	7.20
62	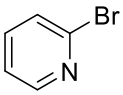 2-bromopyridine	19.4	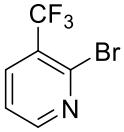 2-bromo-3-trifluoromethyl pyridine	17.7 (d)	1.24
63	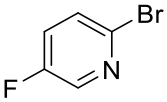 2-bromo-5-fluoropyridine	19.9	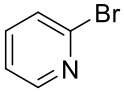 2-bromopyridine	19.4	1.18

64	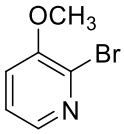 2-bromo-3-methoxypyridine	20.3	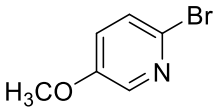 2-bromo-5-methoxypyridine	19.7	4.92
65	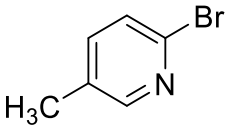 2-bromo-5-methylpyridine	19.3	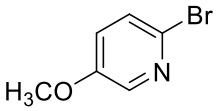 2-bromo-5-methoxypyridine	19.7	3.30
66	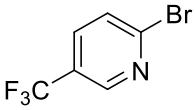 2-bromo-5-trifluoromethyl pyridine	19.9	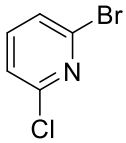 2-bromo-6-chloropyridine	19.6	8.28
67	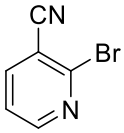 2-bromo-3-cyanopyridine	20.3	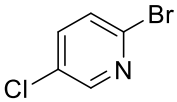 2-bromo-5-chloropyridine	19.8	8.89
68	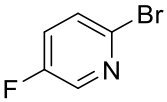 2-bromo-5-fluoropyridine	19.9	 2-bromo-3-trifluoromethyl pyridine	17.6	1.46
69	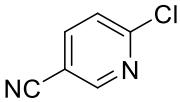 2-chloro-5-cyanopyridine	21.1	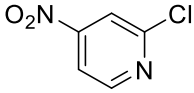 2-chloro-4-nitropyridine	21.6	1.35
70	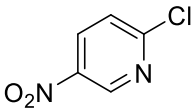 2-chloro-5-nitropyridine	21.3	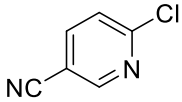 2-chloro-5-cyanopyridine	21.1	6.06
71	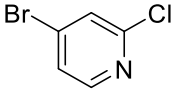 4-bromo-2-chloropyridine	20.2	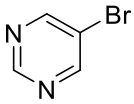 5-bromo-pyrimidine	21.7	3.11
72	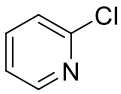 2-chloropyridine	20.5	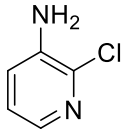 2-chloro-3-aminopyridine	22.9	2.43
73	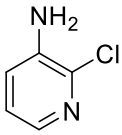 2-chloro-3-aminopyridine	22.9	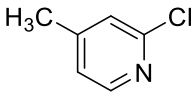 2-chloro-4-methylpyridine	20.7	1.25

74	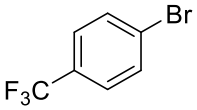 1-bromo-4-trifluoromethyl benzene	19.9	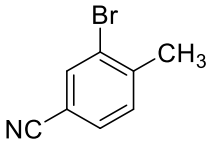 3-bromo-4-methyl -benzonitrile	20.7	15.96
75	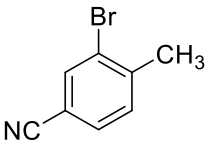 3-bromo-4-methyl -benzonitrile	20.7	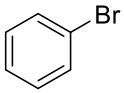 bromobenzene	19.7	2.41
76	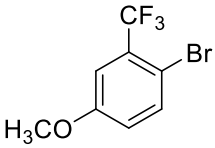 2-bromo-5-methoxy-1-trifluoromethylbenzene	18.1	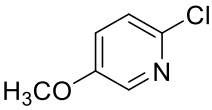 4-bromoanisole	19.8	1.48
77	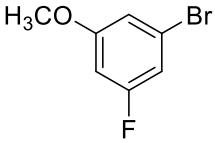 1-bromo-3-fluoro-5-methoxybenzene	19.8	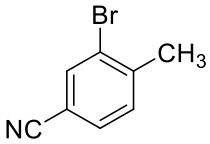 3-bromo-4-methyl benzonitrile	20.7	1.87
78	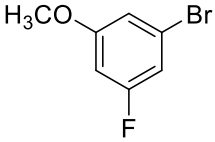 1-bromo-3-fluoro-5-methoxybenzene	19.8	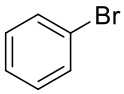 bromobenzene	19.7	3.86
79	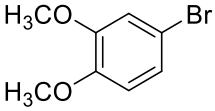 1-bromo-3,4-dimethoxybenzene	19.7	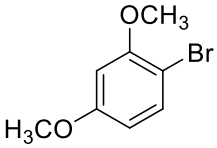 1-bromo-2,4-dimethoxy benzene	21.1	2.93
80	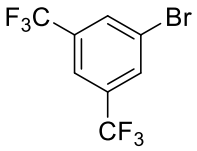 1-bromo-3,5-bis(trifluoromethyl)benzene	20.8	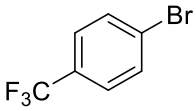 1-bromo-4-trifluoromethyl benzene	19.9	32.25

81	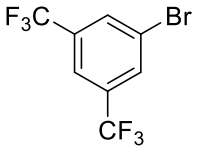 1-bromo-3,5-bis(trifluoromethyl)benzene	20.7	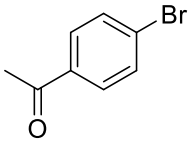 4-bromoacetophenone	19.8	13.48
82	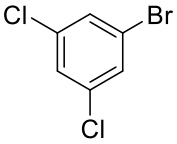 1-bromo-3,5-chlorobenzene	20.3	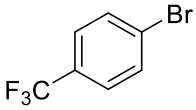 1-bromo-4-trifluoromethyl benzene	19.9	7.23
83	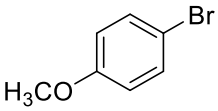 4-bromoanisole	19.7	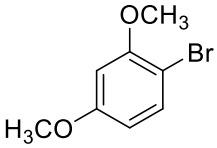 1-bromo-2,4-dimethoxy benzene	21.1	5.52
84	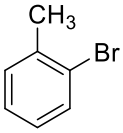 2-bromotoluene	19.8	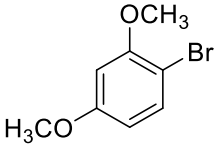 1-bromo-2,4-dimethoxy benzene	21.1	3.73
85	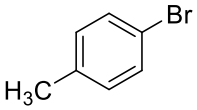 4-bromotoluene	19.5	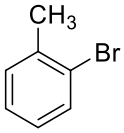 2-bromotoluene	19.8	1.78
86	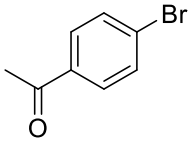 4-bromoacetophenone	19.8	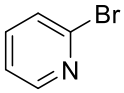 3-bromopyridine	20.6	3.02
87	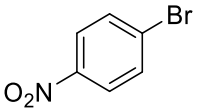 4-bromo-1-nitrobenzene	20.2	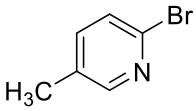 2-bromo-5-methylpyridine	19.3	1.11
88	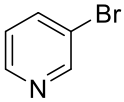 2-bromopyridine	19.5	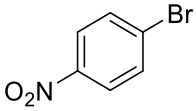 4-bromo-nitrobenzene	20.2	2.43
89	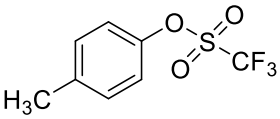 p-Tolyl triflate	22.0	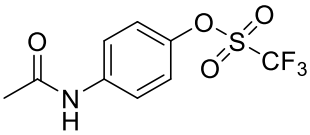 4-acetamidophenyl triflate	22.3	2.56

90	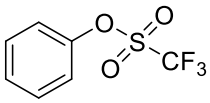 phenyl triflate	22.3	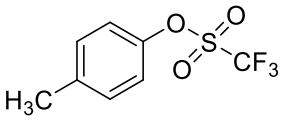 p-Tolyl triflate	22.0	2.43
91	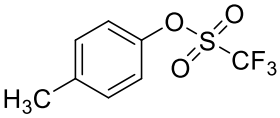 p-Tolyl triflate	22.0	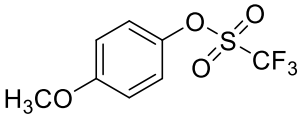 4-methoxyphenyl triflate	22.3	2.09
92[b]	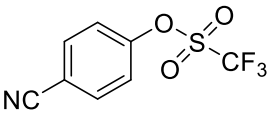 4-cyanophenyl triflate	20.1	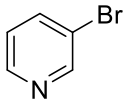 2-bromo-pyridine	19.5	6.65
93[b]	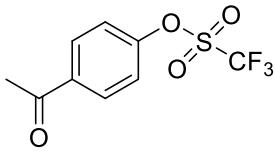 4-acetylphenyl triflate	19.8	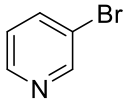 2-bromo-pyridine	19.5	1.17
94[b]	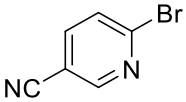 2-bromo-5-cyano-pyridine	20.0	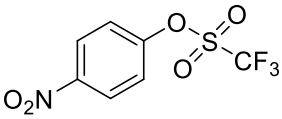 4-nitrophenyl triflate	20.2	4.34
95[b]	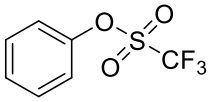 phenyl triflate	19.7	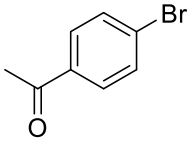 4-bromo-acetophenone	19.9	1.61
96[b]	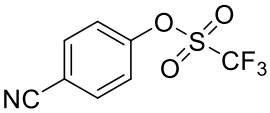 4-cyanophenyl triflate	20.1	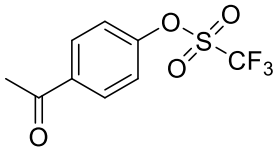 4-acetylphenyl triflate	19.8	5.73
97	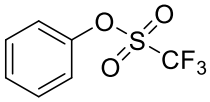 phenyl triflate	22.2	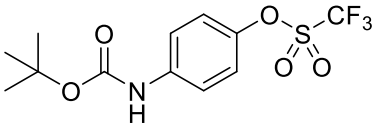 4-(N-Boc-amino)phenyl triflate	22.0	4.13
98	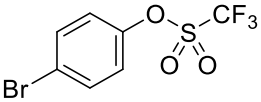 4-bromophenyl triflate	22.4	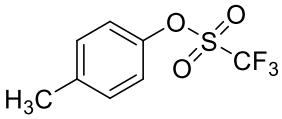 p-Tolyl triflate	22.0	26.03

[a]Peak area ratio = $^{31}P\{^{1}H\}$ qNMR peak area of substrate A oxidative addition product/peak area of substrate B oxidative addition product.

[b]Excess amount of tetrabutylammonium bromide was added to convert Pd(II) triflate species into Pd(II) bromide species.

Figures S3 to S5 contain $^{31}P\{^{1}H\}$ qNMR spectra for three representative competition reactions.

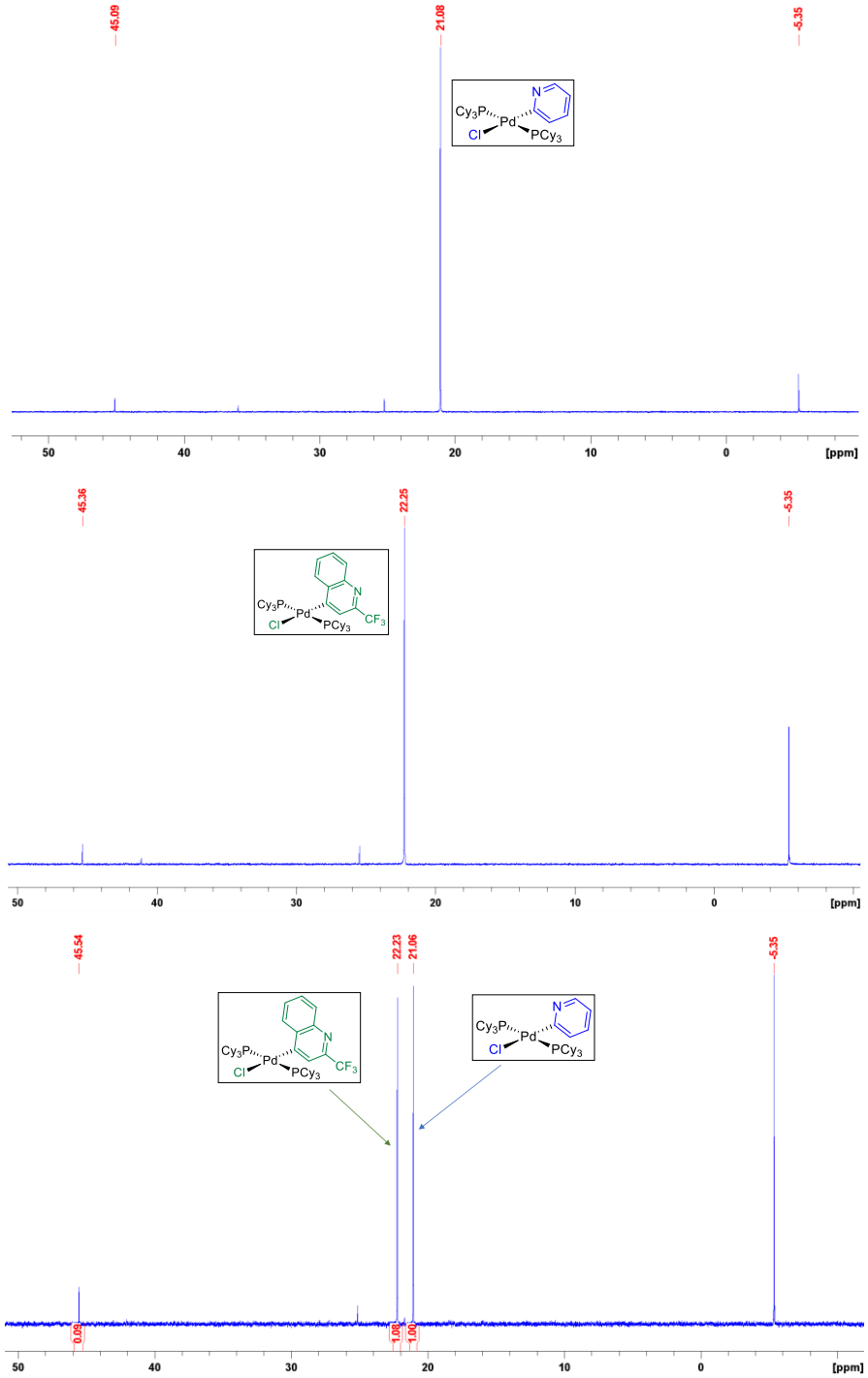

Fig. S3.
Top: $^{31}P\{^{1}H\}$ NMR spectrum of the 2-chloro-pyridine and $Pd(PCy_3)_2$ oxidative addition product; Middle: $^{31}P\{^{1}H\}$ NMR spectrum of the 4-chloro-2-trifluoromethyl-quinoline and $Pd(PCy_3)_2$ oxidative addition product; Bottom: $^{31}P\{^{1}H\}$ qNMR spectrum of the competition reaction of the two above substrates with $Pd(PCy_3)_2$.

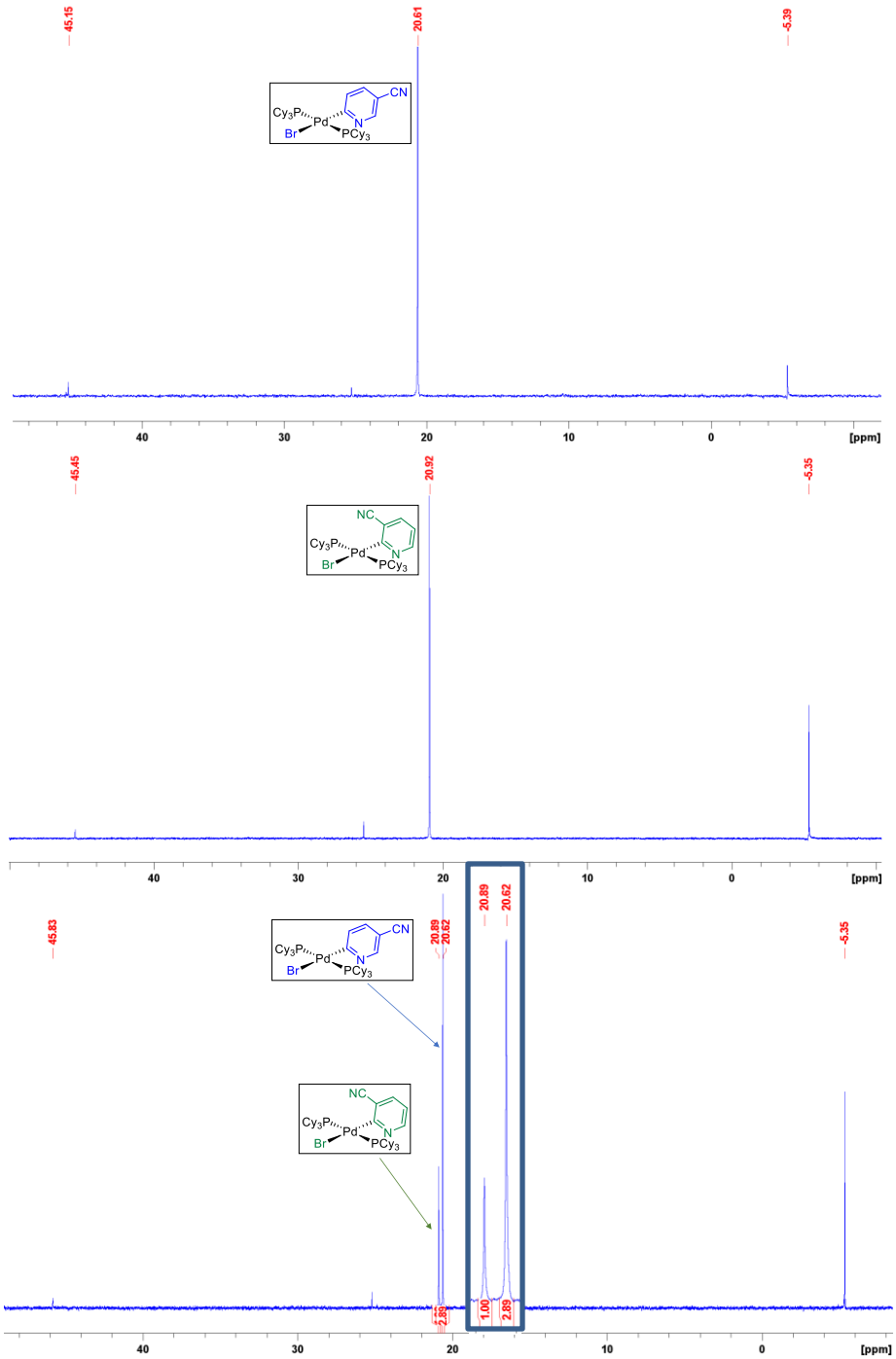

Fig. S4.

Top: $^{31}P\{^{1}H\}$ NMR spectrum of the 2-bromo-5-cyano-pyridine and $Pd(PCy_3)_2$ oxidative addition product; middle: $^{31}P\{^{1}H\}$ NMR spectrum of the 2-bromo-3- cyano-pyridine and $Pd(PCy_3)_2$ oxidative addition product; Bottom: $^{31}P\{^{1}H\}$ qNMR spectrum of the competition reaction of the two above substrates with $Pd(PCy_3)_2$; product peak region expanded in inset.

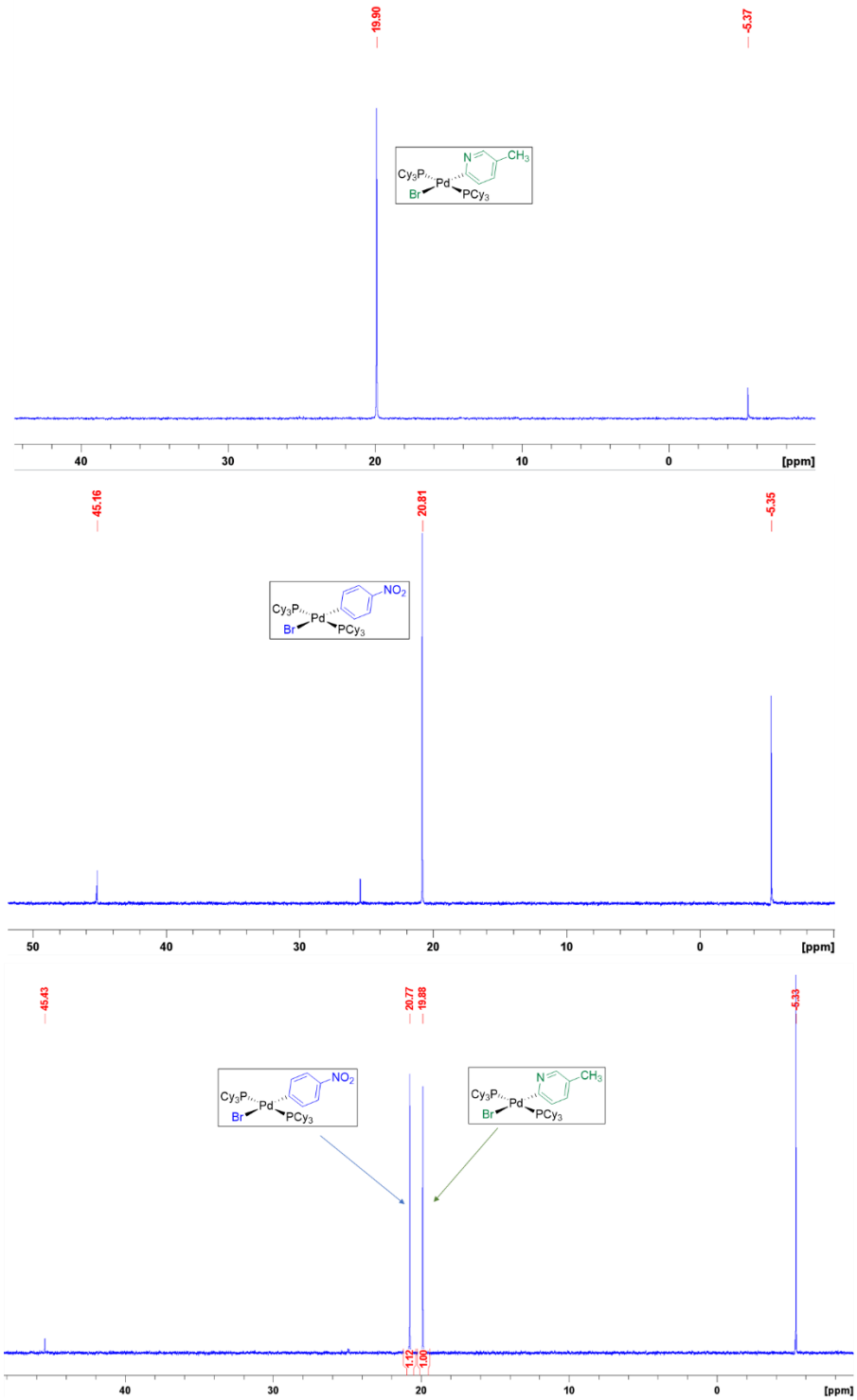

Fig. S5.
Top: $^{31}P\{^{1}H\}$ NMR spectrum of the 2-bromo-5-methyl-pyridine and $Pd(PCy_3)_2$ oxidative addition product; middle: $^{31}P\{^{1}H\}$ NMR spectrum of the 4-bromo-1-nitro-benzene and $Pd(PCy_3)_2$ oxidative addition product; Bottom: $^{31}P\{^{1}H\}$ qNMR spectrum of the competition reaction of the two above substrates with $Pd(PCy_3)_2$.

Calculating Relative $\Delta G^{\ddagger}_{OA}$ for Each Substrate

All of the competition reactions were conducted under *pseudo* first-order conditions, with the two substrates being present in large excess ([substrate]:[Pd source] =20:1). The ratio of the reaction rates can be expressed as Eq (S1):

$$\frac{r_1}{r_2} = \frac{k_1[Pd][Substrate_1]}{k_2[Pd][Substrate_2]} = \frac{k_1[Substrate_1]}{k_2[Substrate_2]} \qquad Eq(S1)$$

The concentrations of the two substrates are assumed to stay constant throughout the reaction; then, Eq (S1) can be simplified to Eq (S2):

$$\frac{r_1}{r_2} = \frac{k_1}{k_2} = \frac{\frac{d[Product_1]}{dt}}{\frac{d[Product_2]}{dt}} = \frac{[Product_1]}{[Product_2]} \qquad Eq(S2)$$

In the $^{31}P\{^1H\}$ qNMR spectroscopy analysis, $\frac{[Product_1]}{[Product_2]}$ is equal to the peak area ratio of the two oxidative addition products from the ^{31}P qNMR spectrum. By substituting the Eyring equation (Eq (S3)):

$$k = \frac{k_B T}{h} \exp\left(-\frac{\Delta G^{\ddagger}}{RT}\right) \qquad Eq(S3)$$

into Eq (S2), the relative activation energy ($\Delta\Delta G^{\ddagger}_{OA}$) of the two oxidative addition reactions from the competition can be calculated by Eq (S4):

$$\frac{k_1}{k_2} = \exp\left(\frac{\Delta G^{\ddagger}{}_2 - \Delta G^{\ddagger}{}_1}{RT}\right) \Rightarrow \Delta\Delta G^{\ddagger}_{OA} = \ln\left(\frac{k_1}{k_2}\right) RT \Rightarrow$$

$$\Delta\Delta G^{\ddagger}_{OA} = \ln\left(\frac{Peak\ area_{Product1}}{Peak\ area_{Product2}}\right) RT \qquad Eq(S4)$$

$$where\ \Delta\Delta G^{\ddagger}_{OA} = \Delta G^{\ddagger}_2 - \Delta G^{\ddagger}_1$$

The experimental $\Delta G^{\ddagger}_{OA}$ for the 79 substrates determined from 98 competition reactions in THF is summarized in Table S2. The most reactive substrate – 2-bromo-5-nitropyridine – is used as the zero point for this scale ($\Delta G^{\ddagger}_{OA}$ set to 0 kJ mol^{-1}), and all other $\Delta G^{\ddagger}_{OA}$ values are given relative to this substrate. Substrates highlighted are those with $\Delta G^{\ddagger}_{OA}$ determined by multiple competition experiments with different substrate pairings. The given $\Delta G^{\ddagger}_{OA}$ values for these substrates are averages of those determined by at least two different competition experiments, and the relative standard deviation (RSD) for these examples is also given.

Table S2.
Observed $\Delta G^{\ddagger}_{OA}$ for 79 substrates determined from competition reactions in THF. The $\Delta G^{\ddagger}_{OA}$ for 2-bromo-5-nitropyridine (first entry) is set to 0.00 kJ mol^{-1}.

Substrate	$\Delta G^{\ddagger}_{OA}$ (kJ/mol)	RSD[a]
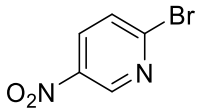 2-bromo-5-nitropyridine	0.00	
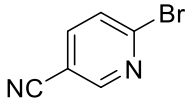 2-bromo-5-cyanopyridine	0.35	
 2-bromo-3-cyanopyridine	2.99	
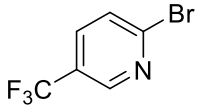 2-bromo-5-trifluoromethylpyridine	3.34	
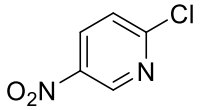 2-chloro-5-nitropyridine	3.85	
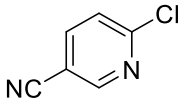 2-chloro-5-cyanopyridine	8.34	
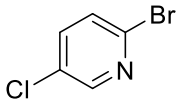 2-bromo-5-chloropyridine	8.43	
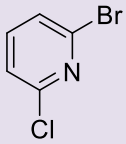 2-bromo-6-chloropyridine	8.59	0.21%
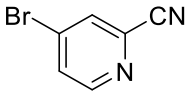 4-bromo-2-cyanopyridine	8.84	
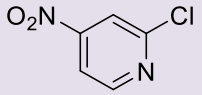 2-chloro-4-nitropyridine	9.14	1.13%

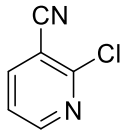 2-chloro-3-cyanopyridine	10.44	
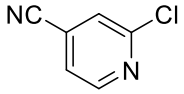 2-chloro-4-cyanopyridine	11.29	
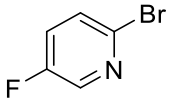 2-bromo-5-fluoropyridine	12.84	
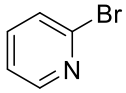 2-bromopyridine	13.26	
 2-bromo-3-trifluoromethylpyridine	13.64	1.86%
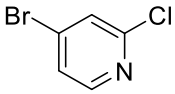 4-bromo-2-chloropyridine	13.79	
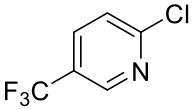 2-chloro-5-trifluoromethylpyridine	13.93	
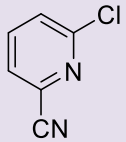 2-chloro-6-cyanopyridine	14.81	1.52%
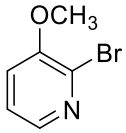 2-bromo-3-methoxypyridine	14.87	
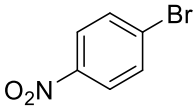 4-bromo-1-nitrobenzene	15.47	
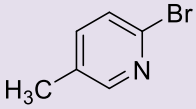 2-bromo-5-methylpyridine	15.87	1.25%

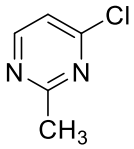 4-chloro-2-methylpyrimidine	16.57	
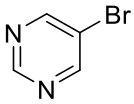 5-bromopyrimidine	16.62	
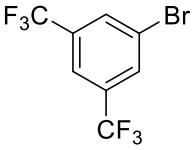 1-bromo-3,5-(bis)trifluoromethylbenzene	18.11	
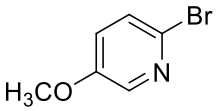 2-bromo-5-methoxypyridine	18.84	
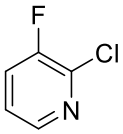 2-chloro-3-fluoropyridine	19.00	
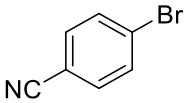 4-bromobenzonitrile	20.60	
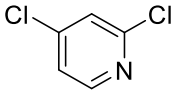 2,4-dichloropyridine	20.98	
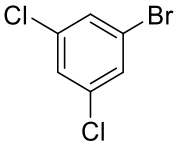 1-bromo-3,5-chlorobenzene	21.33	
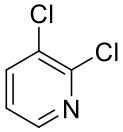 2,3-dichloropyridine	22.16	
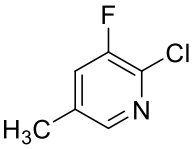 2-chloro-3-fluoro-5-methylpyridine	22.96	

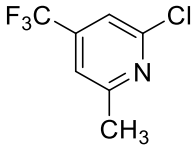 2-chloro-4-trifluormethyl-6-methylpyridine	23.35	
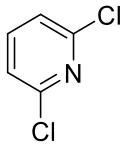 2,6-dichloropyridine	23.79	
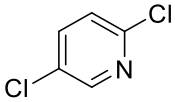 2,5-dichloropyridine	23.87	
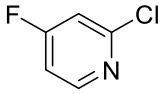 2-chloro-4-fluoropyridine	24.00	
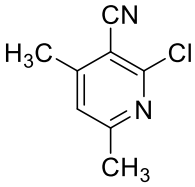 2-chloro-3-cyano-4,6-dimethylpyridine	24.28	
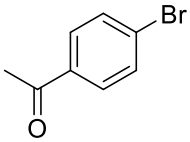 4-bromoacetophenone	24.59	
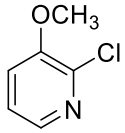 2-chloro-3-methoxypyridine	25.39	
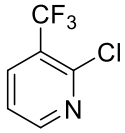 2-chloro-3-trifluoromethylpyridine	26.10	
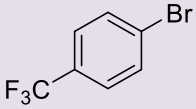 1-bromo-4-trifluoromethylbenzene	26.26	2.70%

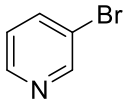 3-bromopyridine	27.34	
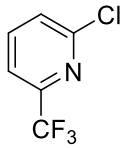 2-chloro-6-trifluoromethylpyridine	27.37	
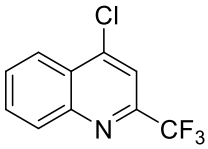 4-chloro-2-trifluoromethylquinoline	28.51	
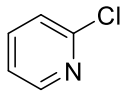 2-chloropyridine	28.70	
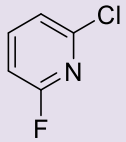 2-chloro-6-fluoropyridine	29.12	0.17%
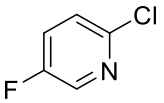 2-chloro-5-fluoropyridine	29.76	
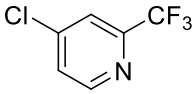 4-chloro-2-trifluoromethylpyridine	30.69	
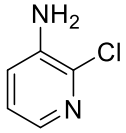 2-chloro-3-aminopyridine	30.91	
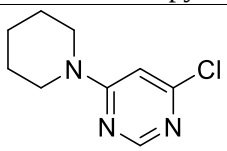 4-chloro-6-(piperidin-1-yl)pyrimidine	30.98	
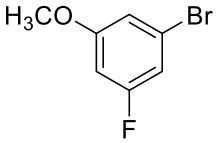 1-bromo-3-fluoro-5-methoxybenzene	31.36	

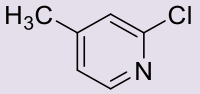 2-chloro-4-methylpyridine	31.36	0.48%
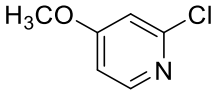 2-chloro-4-methoxypyridine	31.78	
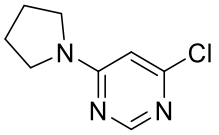 4-Chloro-6-(pyrrolidin-1-yl)pyrimidine	32.05	
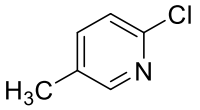 2-chloro-5-methylpyridine	32.25	
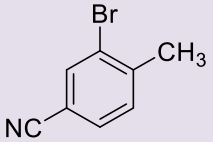 3-bromo-4-methylbenzonitrile	32.92	1.29%
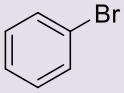 bromobenzene	34.36	3.07%
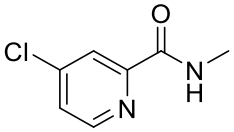 *N*-methyl-4-chloropyridine-2-carboxamide	34.46	
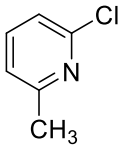 2-chloro-6-methylpyridine	34.48	
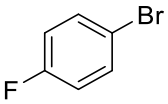 1-bromo-4-fluorobenzene	34.56	
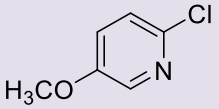 2-chloro-5-methoxypyridine	35.78	1.55%

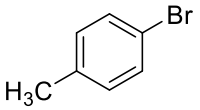 4-bromotoluene	35.96	
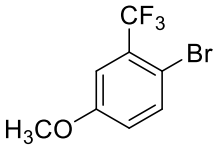 2-bromo-5-methoxy-1-trifluoromethylbenzene	36.35	
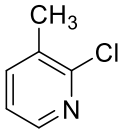 2-chloro-3-methylpyridine	36.45	
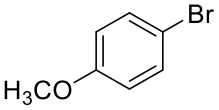 4-bromoanisole	37.32	
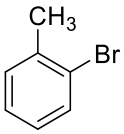 2-bromotoluene	37.39	
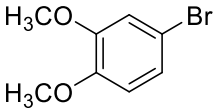 1-bromo-3,4-dimethoxybenzene	38.45	
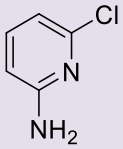 2-chloro-6-aminopyridine	40.80	0.34%
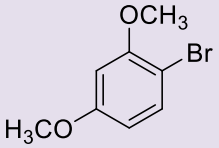 1-bromo-2,4-dimethoxybenzene	41.13	1.56%
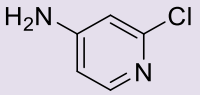 2-chloro-4-aminopyridine	41.41	0.15%
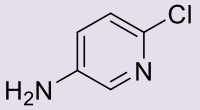 2-chloro-5-aminopyridine	42.55	0.72%

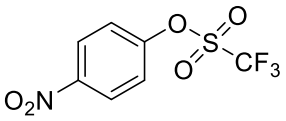 4-nitrophenyl triflate	4.00	
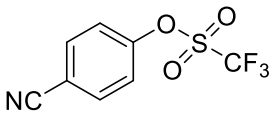 4-cyanophenyl triflate	8.54	
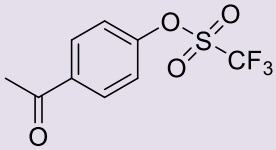 4-acetylphenyl triflate	12.88	0.11%
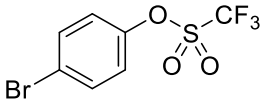 4-bromophenyl triflate	17.49	
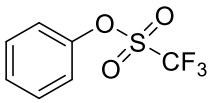 phenyl triflate	23.40	
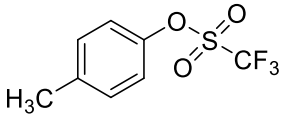 p-Tolyl triflate	25.61	
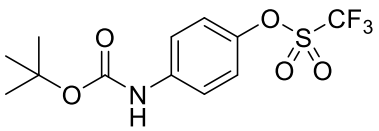 4-(N-Boc-amino)phenyl triflate	26.93	
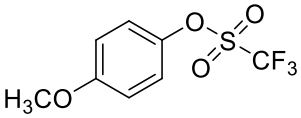 4-methoxyphenyl triflate	27.45	
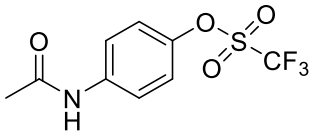 4-acetamidophenyl triflate	27.95	

[a]RSD values determined from the $\Delta G^{\ddagger}_{OA}$ values obtained by independent competition experiments with different substrates (see Table S1).

Assessing Possible Reversibility of Oxidative Addition

Our experimental approach of determining the rate constant ratio from the oxidative addition product ratio is only valid if the oxidative addition reactions are under kinetic control at room temperature; therefore, we conducted a series of experiments to confirm that kinetically controlled product mixtures are formed, with no reversible oxidative addition. We selected 6 pairs of substrates to test for reversibility, and the experimental details and test results are summarized in Table S3.

For each pair of substrates, we first conducted individual oxidative addition reactions for the two substrates separately using the general procedure outlined previously. The reaction solutions were analyzed by $^{31}P\{^{1}H\}$ NMR to confirm that $Pd(PCy_3)_2$ reacted to completion before the next step. Once confirmed complete, the individual reaction solutions were mixed in a 1:1 v/v ratio, resulting in a 1:1 molar ratio of Pd(II) products. Half of the resulting mixture was immediately analyzed by $^{31}P\{^{1}H\}$ qNMR spectroscopy to confirm this 1:1 ratio of the two Pd oxidative addition complexes, while the other half of the mixture was left stirring overnight. After 24 hours, a $^{31}P\{^{1}H\}$ qNMR spectrum of the stirred reaction mixture was recorded, revealing no change to the product ratio. If the product ratio in our competition experiments was thermodynamically controlled through reversible oxidative addition, the 1:1 product mixture would have changed to reflect that ratio. Comparing the results from these 6 reversibility tests to the results from the corresponding competition reactions reveals that the competition product ratio is kinetically controlled.

$^{31}P\{^{1}H\}$ qNMR spectra from one representative reversibility test as well as the $^{31}P\{^{1}H\}$ qNMR spectrum of the corresponding competition reaction are shown in Figure S6.

Table S3.
Test reactions for possible reversibility in oxidative addition competition experiments
.

Exp No.	Substrate A	Substrate B	Initial Product ratio	Product ratio after 24 h	Competition reaction product ratio
1	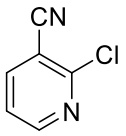 2-chloro-3-cyanopyridine	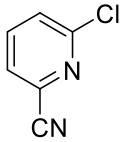 2-chloro-6-cyanopyridine	1.03	1.03	6.16
2	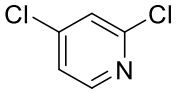 2,4-dichloropyridine	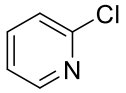 2-chloropyridine	0.97	0.97	22.17
3	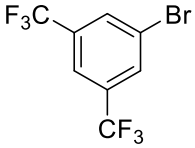 1-bromo-3,5-bis(trifluoromethyl) benzene	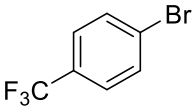 1-bromo-4-trifluoromethyl benzene	1.04	1.04	32.25
4	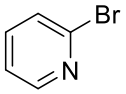 2-bromopyridine	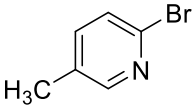 2-bromo-5-methylpyridine	1.00	1.00	3.02
5	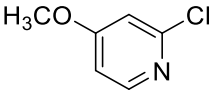 2-chloro-4-methoxypyridine	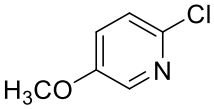 2-chloro-5-methoxypyridine	0.87	0.87	4.25
6	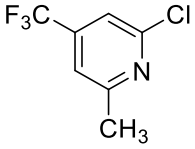 2-chloro-4-trifluoromethyl -6-methylpyridine	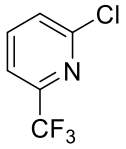 2-chloro-6-trifluoromethyl pyridine	1.04	1.04	5.02

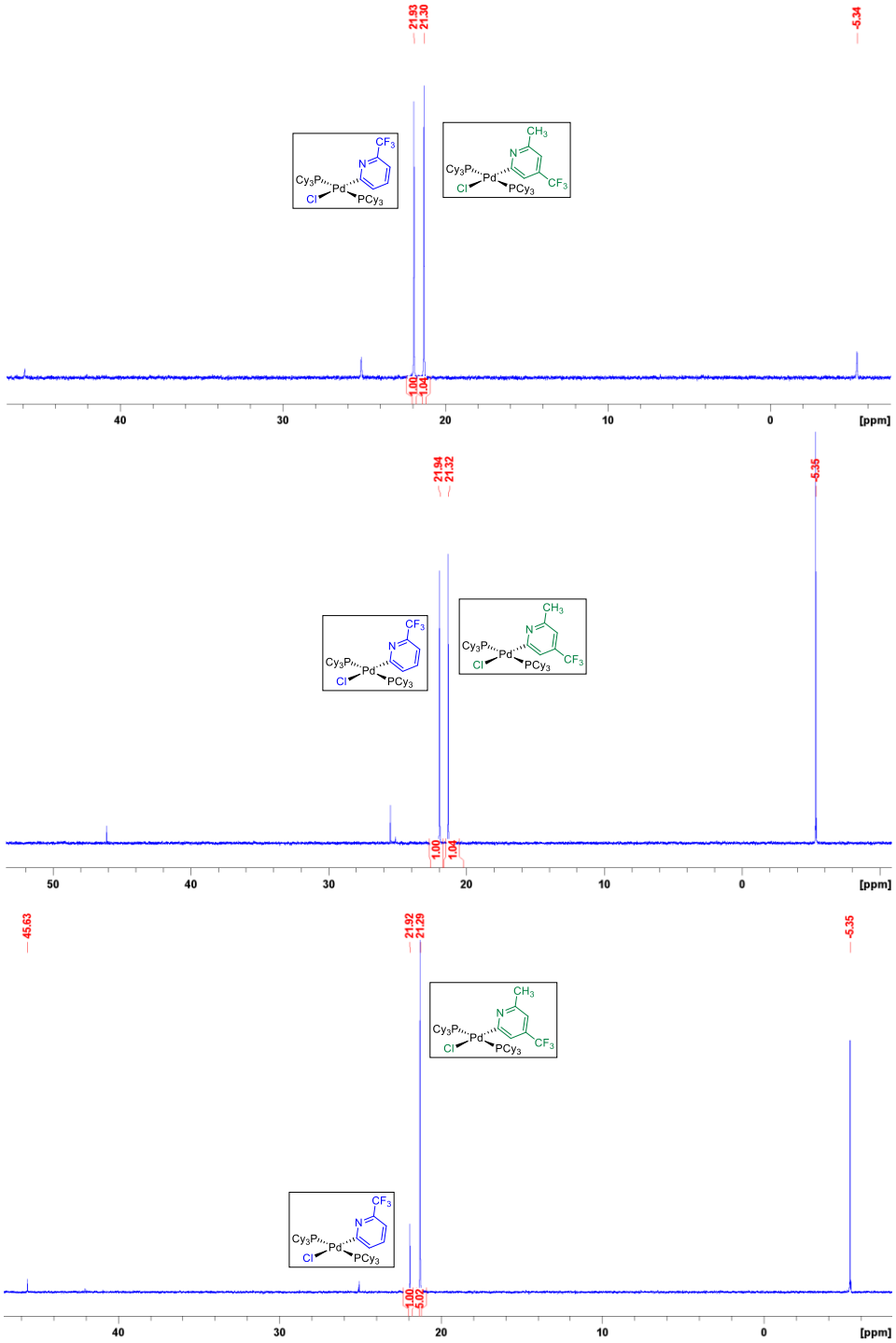

Fig. S6.
$^{31}P\{^{1}H\}$ NMR spectra for the reversibility test of 2-chloro-4-trifluoromethyl-6-methyl-pyridine and 2-chloro-6-trifluoromethyl-pyridine oxidative addition products. Top: $^{31}P\{^{1}H\}$ NMR spectrum of the 1:1 product mixture right after mixing. Middle: $^{31}P\{^{1}H\}$ NMR spectrum of the 1:1 product mixture after 24 hours. Bottom: $^{31}P\{^{1}H\}$ NMR spectrum of the competition reaction outcome.

Preparative Scale Synthesis of Oxidative Addition Complexes

Six representative Pd(II) oxidative addition complexes derived from 2-halopyridine substrates were isolated, purified, and characterized using the following general procedure.

All stock solutions were prepared in the following concentrations in THF: substrate (0.375 M), and $Pd(PCy_3)_2$ (0.0375 M).

In the glovebox, a 20 mL vial containing a stir bar was charged with 300 µL of the substrate stock solution (0.1125 mmol, 1.5 equiv.), 2 mL of the $Pd(PCy_3)_2$ stock solution (0.075 mmol, 1.0 equiv.), and 5 mL of THF. The reaction mixture was stirred at room temperature overnight. A $^{31}P\{^1H\}$ NMR spectrum was recorded to confirm the $Pd(PCy_3)_2$ had reacted to completion. The reaction mixture was then transferred outside glovebox for further purification.

The solvent was evaporated under vacuum using a rotary evaporator. The solid left in the vial was washed with either pentane or diethyl ether (2 x 7 mL) to remove unreacted substrate. The solid was dried under vacuum to give the oxidative addition product, and the isolated yield was recorded.

Pentane was used to wash the products of 2-chloropyridine, 2-chloro-6-trifluoropyridine and 2-bromo-5-chloropyridine with $Pd(PCy_3)_2$. Diethyl ether was used to wash the products of 2-chloro-3-cyanopyridine, 2-chloro-4-nitropyridine and 2-chloro-3-aminopyridine with $Pd(PCy_3)_2$.

<u>Characterization of Isolated Oxidative Addition Complexes</u>

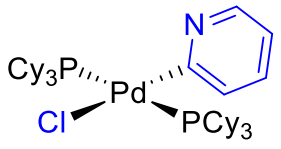

S1

The oxidative addition product **S1** was prepared by the general procedure using 2-chloropyridine. 43.2 mg of a white solid was obtained (73.8% yield)

^1H NMR: (500 MHz, $CDCl_3$): δ 1.01-1.98 (m, 66H, 66 x Cy-H), 6.70 (t, 1H, 1 x Py-H), 7.06 (t, 1H, 1 x Py-H), 7.32 (d, 1H, 1 x Py-H), 8.36 (dd, 1H, 1 x Py-H).

$^{13}C\{^1H\}$ NMR: (126 MHz, $CDCl_3$): δ 25.61-33.71 (36 x Cy), 116.9 (1 x Py), 131.90 (1 x Py), 134.90 (1 x Py), 147.96 (1 x Py), 178.89 (1 x Py).

$^{31}P\{^1H\}$ NMR: (203 MHz, $CDCl_3$): δ 20.26.

HRMS (ESI): $[C_{41}H_{70}P_2PdN]^+$ (target compound minus the chlorine): 744.40128 (calc'd), 744.40204 (found); $[C_{41}H_{70}P_2PdNCl{\cdot}H]^+$ (hydrogen adduct): 780.37796 (calc'd), 780.37888 (found).

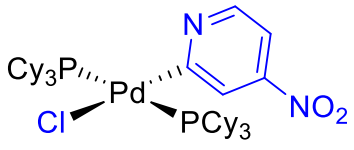

S2

The oxidative addition product **S2** was prepared by the general procedure using 2-chloro-4-nitropyridine. 19.5 mg of a light-yellow solid was obtained (31.5% yield) as the isolated product.

^1H NMR: (300 MHz, $CDCl_3$): δ 0.92-1.82 (m, 66H, 66 x Cy-H), 7.31 (d, 1H, 1 x Py-H), 7.97 (s, 1H, 1 x Py-H), 8.63 (d, 1H, 1 x Py-H).

$^{13}C\{^1H\}$ NMR: (126 MHz, $CDCl_3$): δ 26.49-33.84 (36 x Cy), 108.19 (1 x Py), 124.47 (1 x Py), 149.34 (1 x Py), 149.73 (1 x Py), 186.34 (1 x Py).

$^{31}P\{^1H\}$ NMR: (203 MHz, $CDCl_3$): δ 21.56.

HRMS (ESI): $[C_{41}H_{69}P_2PdN_2O_2]^+$ (target compound minus the chlorine): 789.38636 (calc'd), 789.38722 (found); $[C_{41}H_{69}P_2PdN_2O_2Cl{\cdot}H]^+$ (hydrogen adduct): 825.36304 (calc'd), 825.36395 (found).

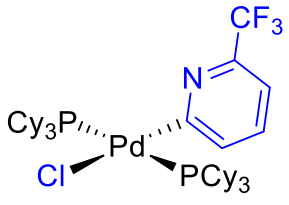

S3

The oxidative addition product was prepared by the general procedure using 2-chloro-6-trifluoromethylpyridine. 29.7 mg of a white solid was obtained (57.3%) as the isolated product.

^1H NMR: (500 MHz, $CDCl_3$): δ 1.02-1.96 (m, 66H, 66 x Cy-H), 7.10 (d, 1H, 1 x Py-H), 7.16 (t, 1H, 1 x Py-H), 7,57 (d, 1H, 1 x Py-H).

$^{13}C\{^1H\}$ NMR: (126 MHz, $CDCl_3$): δ 22.35-33.60 (36 x Cy), 131.46 (1 x Py), 182.33 (1 x Py).

$^{31}P\{^1H\}$ NMR: (203 MHz, $CDCl_3$): δ 21.05.

$^{19}F\{^1H\}$ NMR: (471 MHz, $CDCl_3$): δ 21.05.

HRMS (ESI): $[C_{42}H_{69}P_2PdNF_3]^+$ (target compound minus the chlorine): 812.38867 (calc'd), 812.38996 (found); $[C_{42}H_{69}P_2PdNF_3Cl{\cdot}H]^+$ (hydrogen adduct): 848.36535 (calc'd), 848.36632 (found).

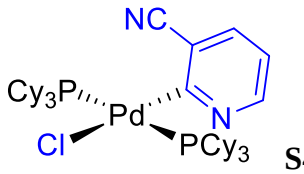

S4

The oxidative addition product **S4** was prepared by the general procedure using 2-chloro-3-cyanopyridine. 42.1 mg of a white solid was obtained (69.7%) as the isolated product.

^1H NMR: (500 MHz, $CDCl_3$): δ 0.99-2.06 (m, 66H, 66 x Cy-H), 6.83 (dd, 1H, 1 x Py-H), 7.47 (d, 1H, 1 x Py-H), 8.60 (dd, 1H, 1 x Py-H).

$^{13}C\{^1H\}$ NMR: (126 MHz, $CDCl_3$): δ 26.51-34.17 (36 x Cy), 116.32 (1 x CN-Py), 120.14 (1 x Py), 121.11 (1 x Py), 137.36 (1 x Py), 150.52 (1 x Py), 186.91 (1 x Py).

$^{31}P\{^1H\}$ NMR: (203 MHz, $CDCl_3$): δ 21.76.

HRMS (ESI): $[C_{42}H_{69}P_2PdN_2]^+$ (major isotopomer, target compound minus the chlorine): 769.39653 (calc'd), 769.39698 (found); $[C_{42}H_{69}P_2PdN_2Cl{\cdot}H]^+$ (hydrogen adduct): 805.37321 (calc'd), 805.37288 (found); $[C_{42}H_{69}P_2PdN_2Cl{\cdot}Na]^+$ (sodium adduct): 827.35516 (calc'd), 827.35502 (found).

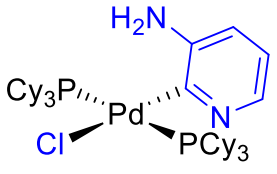

S5

The oxidative addition product **S5** was prepared by the general procedure using 2-chloro-3-aminopyridine. 31.6 mg of a light brown solid was obtained (52.9%) as the isolated product.

^{1}H NMR: (500 MHz, $CDCl_3$): δ 1.04-2.03 (m, 66H, 66 x Cy-H), 4.26 (s, 2H, N*H2*-Py), 6.39 (d, 1H, 1 x Py-H), 6.60 (dd, 1H, 1 x Py-H), 7.96 (d, 1H, 1 x Py-H).

^{13}C{1H} NMR: (126 MHz, $CDCl_3$): δ 27.73-34.15 (36 x Cy), 115.80 (1 x Py), 117.53 (1 x Py), 138.91 (1 x Py), 145.20 (1 x Py), 164.21 (1 x Py).

^{31}P{^{1}H} NMR: (203 MHz, $CDCl_3$): δ 23.20.

HRMS (ESI): $[C_{41}H_{71}P_2PdN_2Cl{\cdot}H]^+$ (major isotopomer, hydrogen adduct): 795.38886 (calc'd), 795.38898 (found).

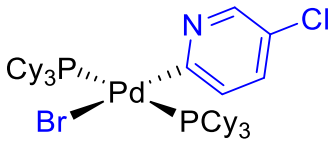

S6

The oxidative addition product **S6** was prepared by the general procedure from 2-bromo-5-chloropyridine. 35.3 mg of a light-yellow solid was obtained (54.8%) as the isolated product.

^{1}H NMR: (500 MHz, $CDCl_3$): δ 1.04-2.00 (m, 66H, 66 x Cy-H), 7.11 (dd, 1H, 1 x Py-H), 7.31 (d, 1H, 1 x Py-H), 8.42 (d, 1H, 1 x Py-H).

^{13}C{^{1}H} NMR: (126 MHz, $CDCl_3$): δ 26.37-35.15 (36 x Cy), 126.31 (1 x Py), 131.42 (1 x Py), 134.57 (1 x Py), 146.34 (1 x Py), 177.87 (1 x Py).

^{31}P{^{1}H} NMR: (203 MHz, $CDCl_3$): δ 19.89.

HRMS (ESI): $[C_{41}H_{69}P_2PdNCl]^+$ (major isotopomer, target compound minus the bromine): 778.36231 (calc'd), 778.36264 (found).

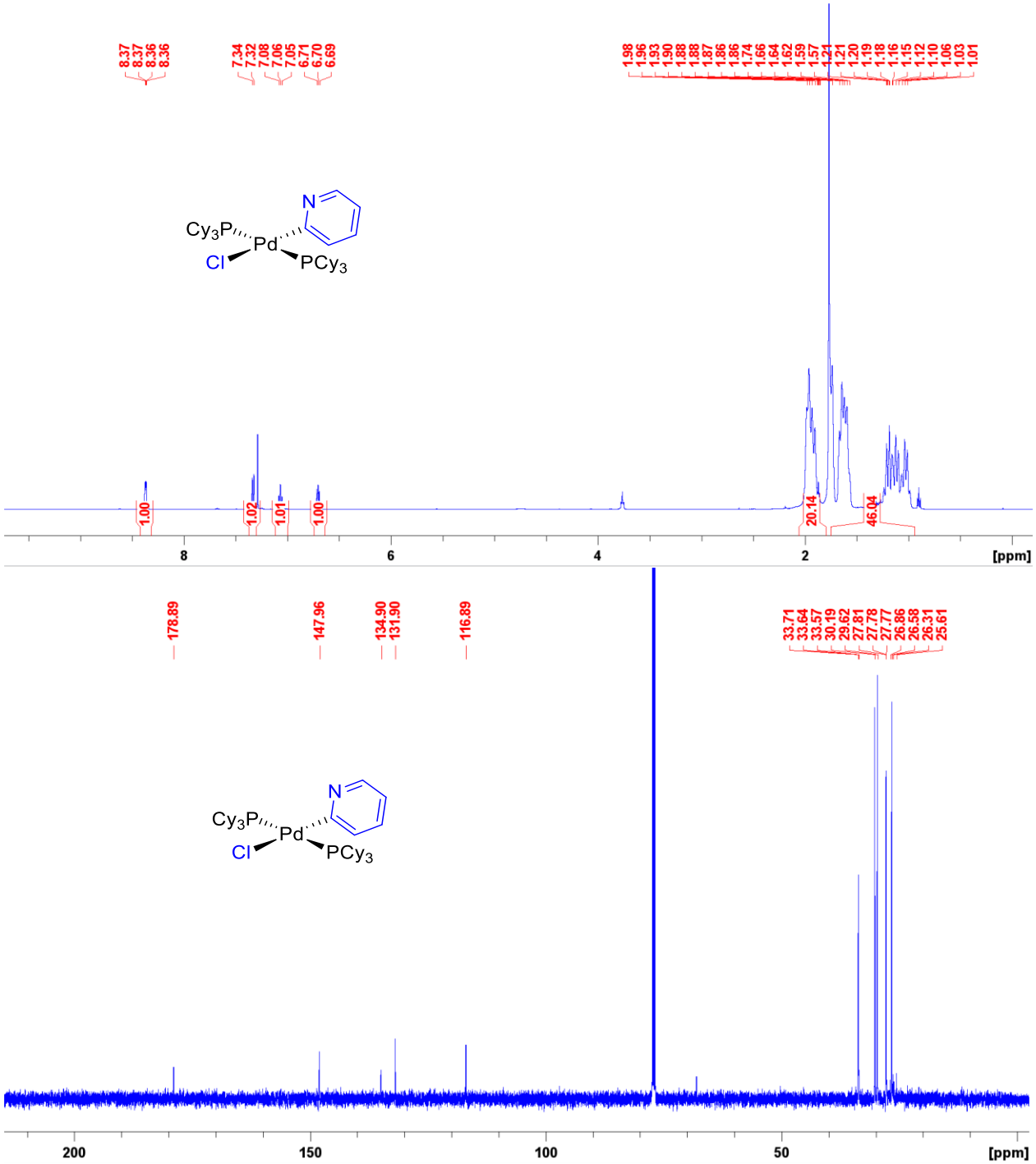

Fig. S7.
^{1}H (500 MHz, $CDCl_3$) and $^{13}C\{^{1}H\}$ (126 MHz, $CDCl_3$) NMR spectra of **S1**.

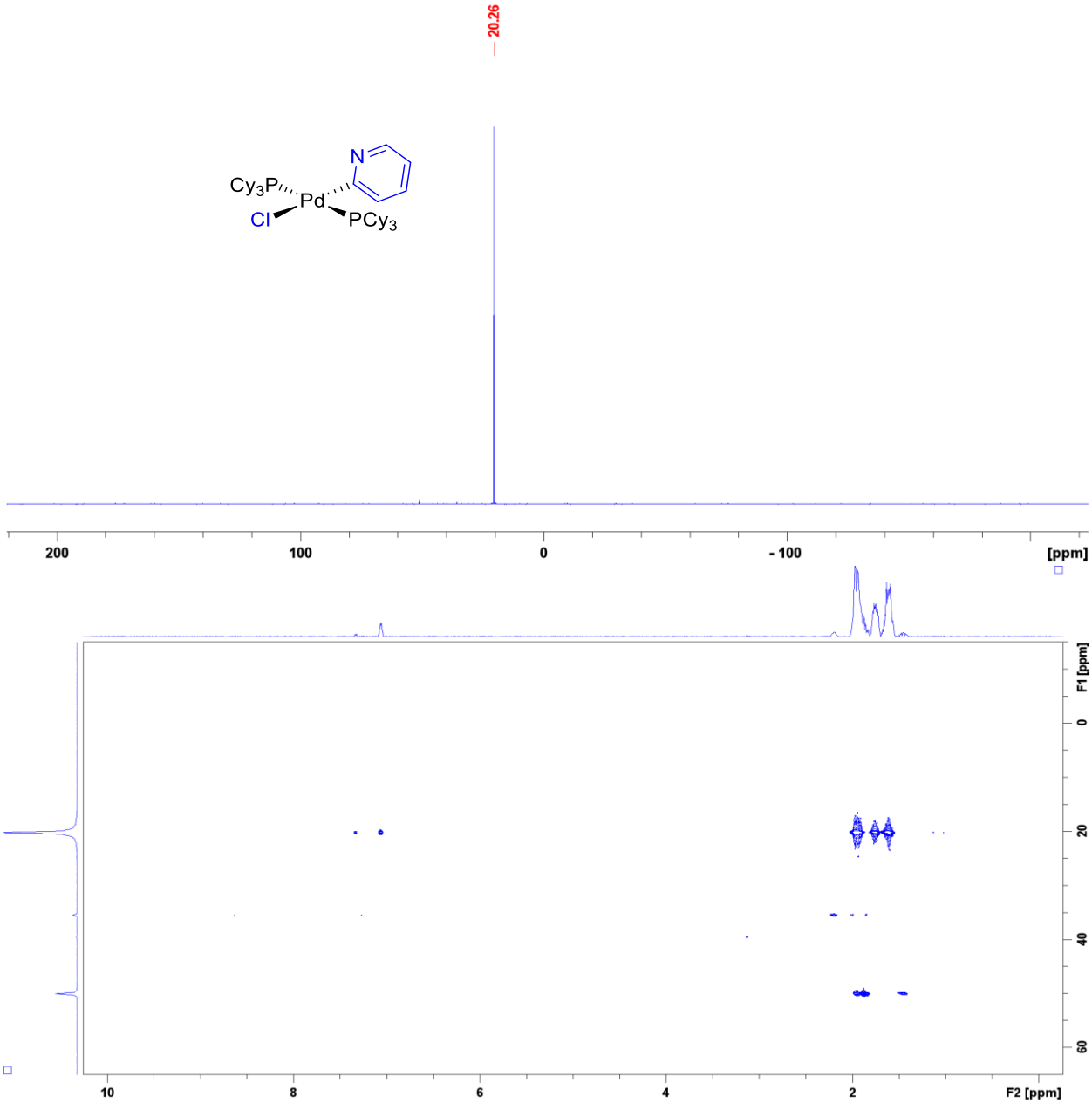

Fig. S8.
$^{31}P\{^{1}H\}$ NMR (203 MHz, $CDCl_3$) spectrum of **S1**, with accompanying long range ^{1}H-^{31}P HMBC NMR spectrum.

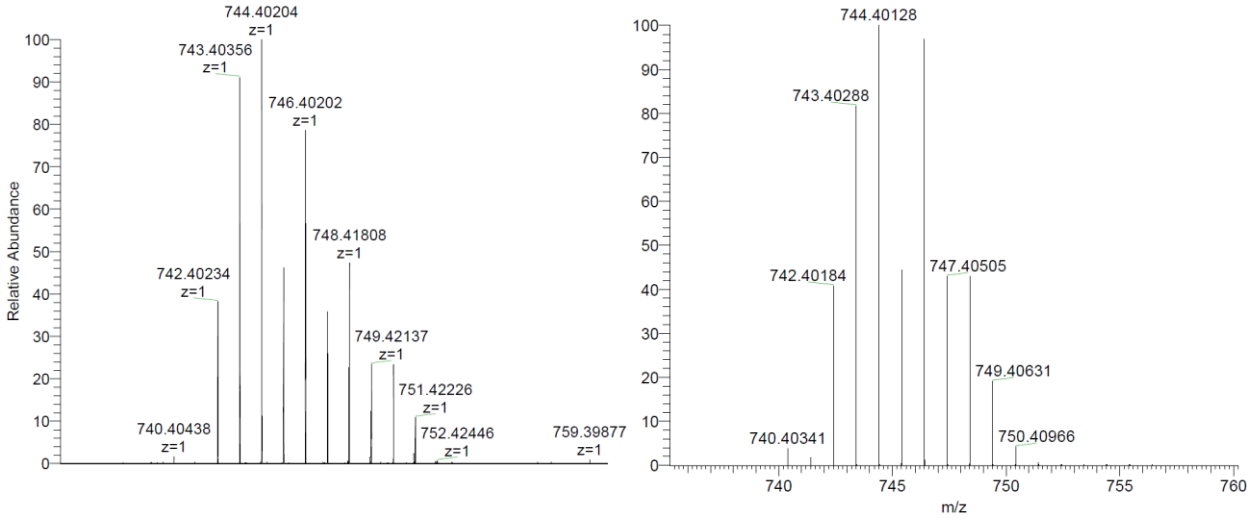

Fig. S9.
Left: Experimental HRMS-ESI spectrum of [**S1**-Cl]$^+$. Right: Calculated HRMS isotope pattern for [**S1**-Cl] $^+$.

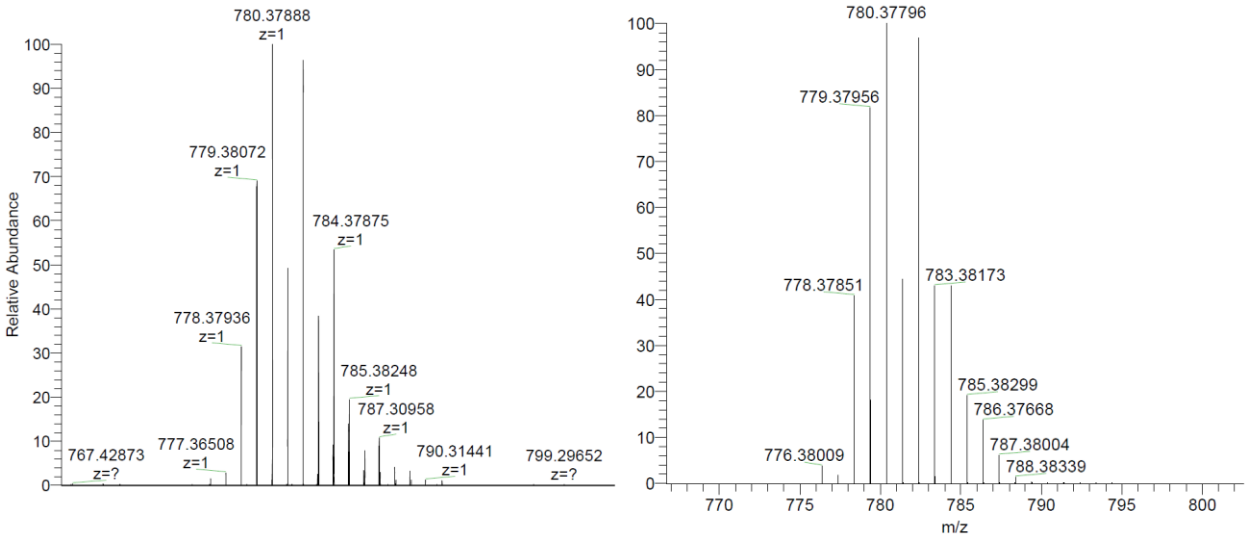

Fig. S10.
Left: Experimental HRMS-ESI spectrum of [**S1**+H]$^+$. Right: Calculated HRMS isotope pattern for [**S1**+H]$^+$.

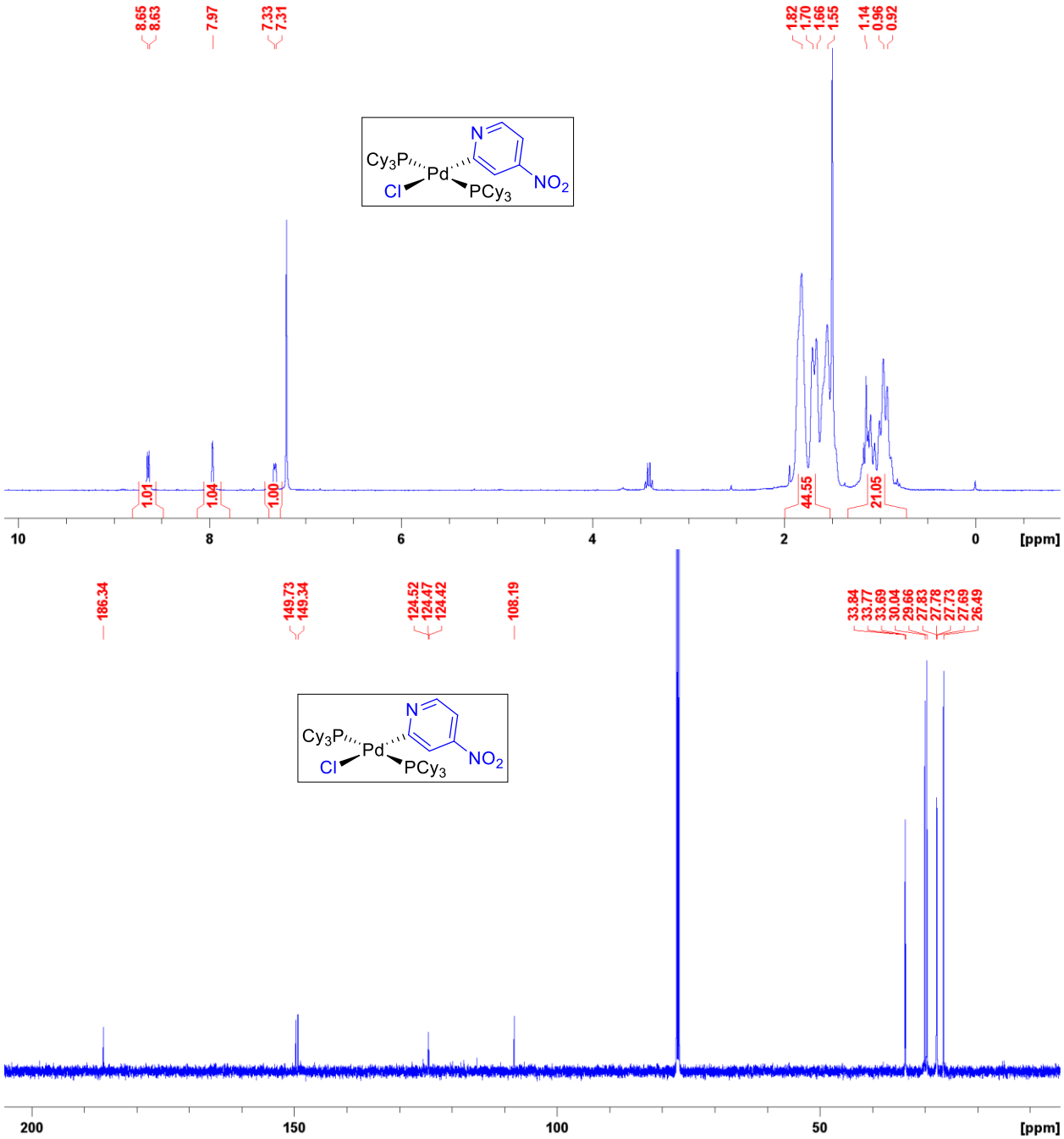

Fig. S11.
^{1}H (500 MHz, $CDCl_3$) and ^{13}C{^{1}H} (126 MHz, $CDCl_3$) NMR spectra of **S2**.

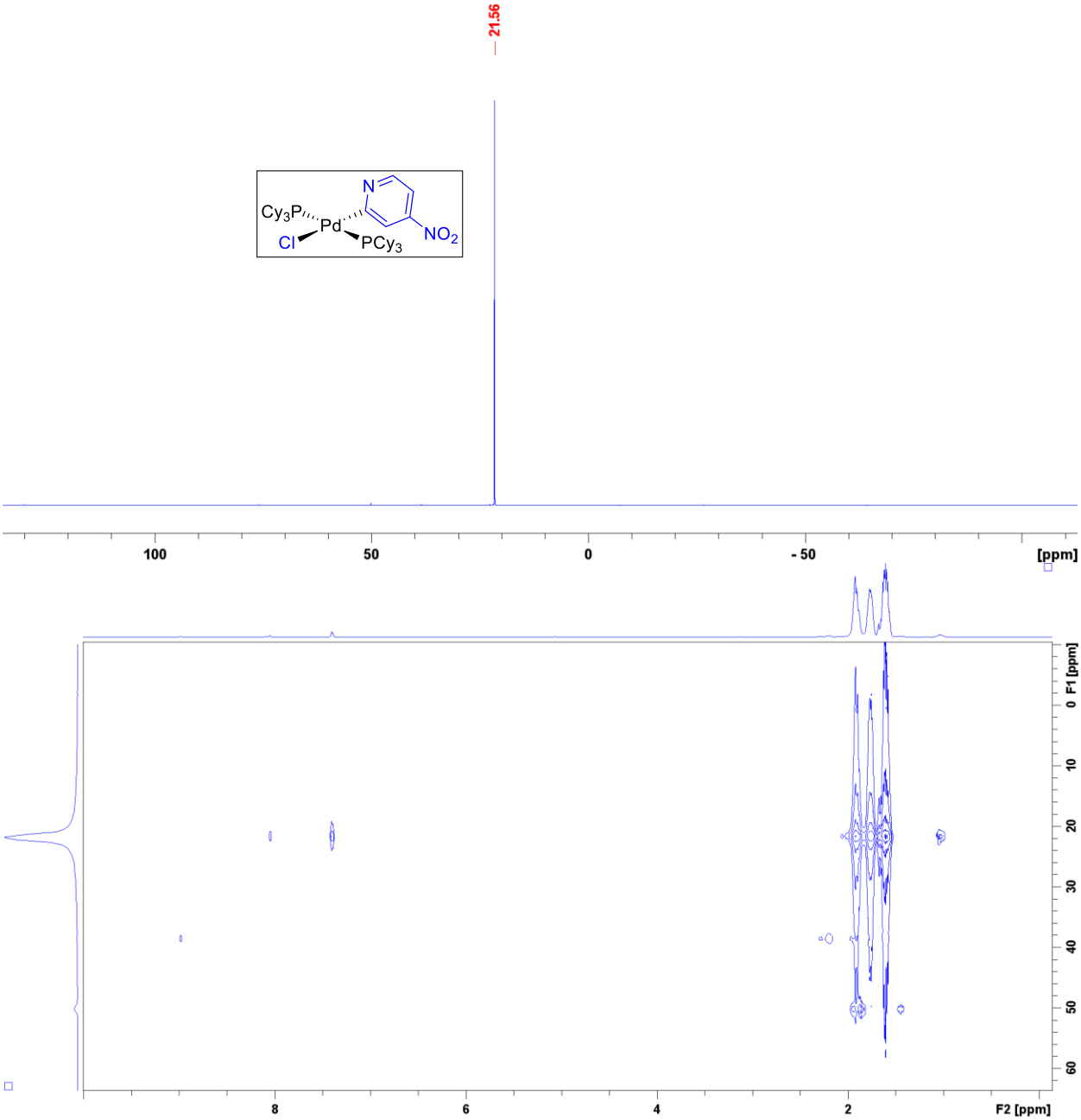

Fig. S12.
$^{31}P\{^{1}H\}$ NMR (203 MHz, $CDCl_3$) spectrum of **S2**, with accompanying long range ^{1}H-^{31}P HMBC NMR spectrum.

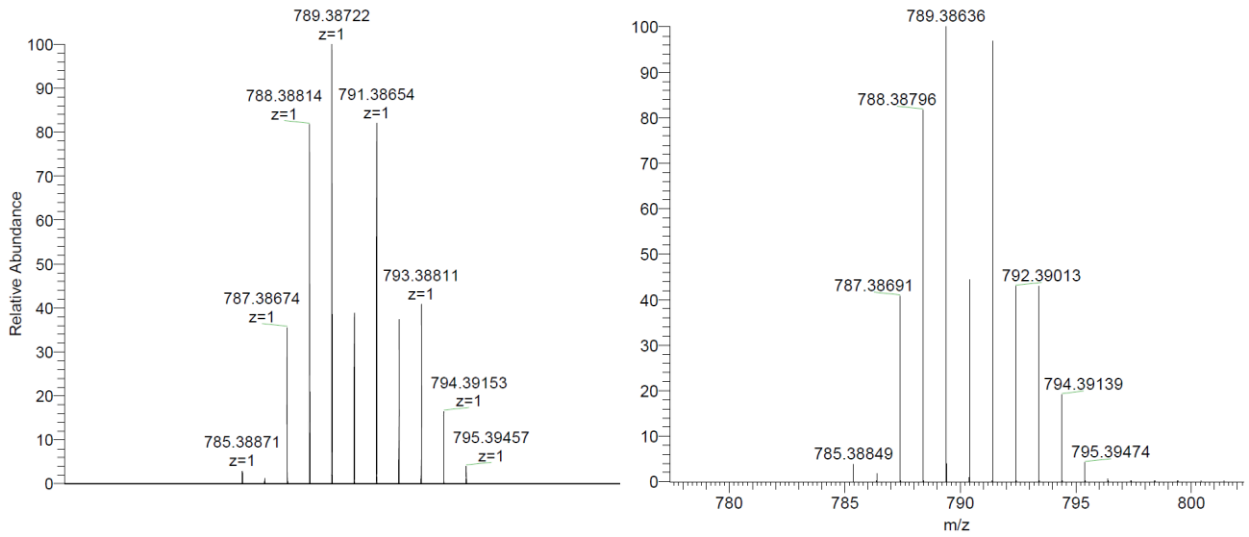

Fig. S13.
Left: Experimental HRMS-ESI spectrum of [**S2**-Cl]$^+$. Right: Calculated HRMS isotope pattern for [**S2**-Cl] $^+$.

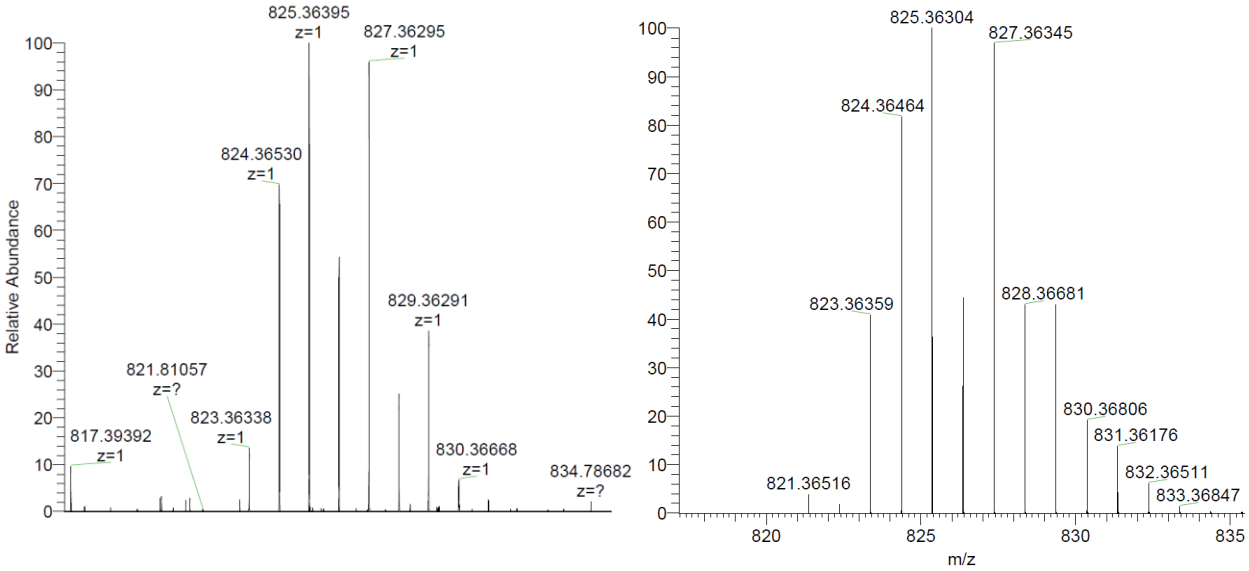

Fig. S14.
Left: Experimental HRMS-ESI spectrum of [**S2**+H]$^+$. Right: Calculated HRMS isotope pattern for [**S2**+H]$^+$.

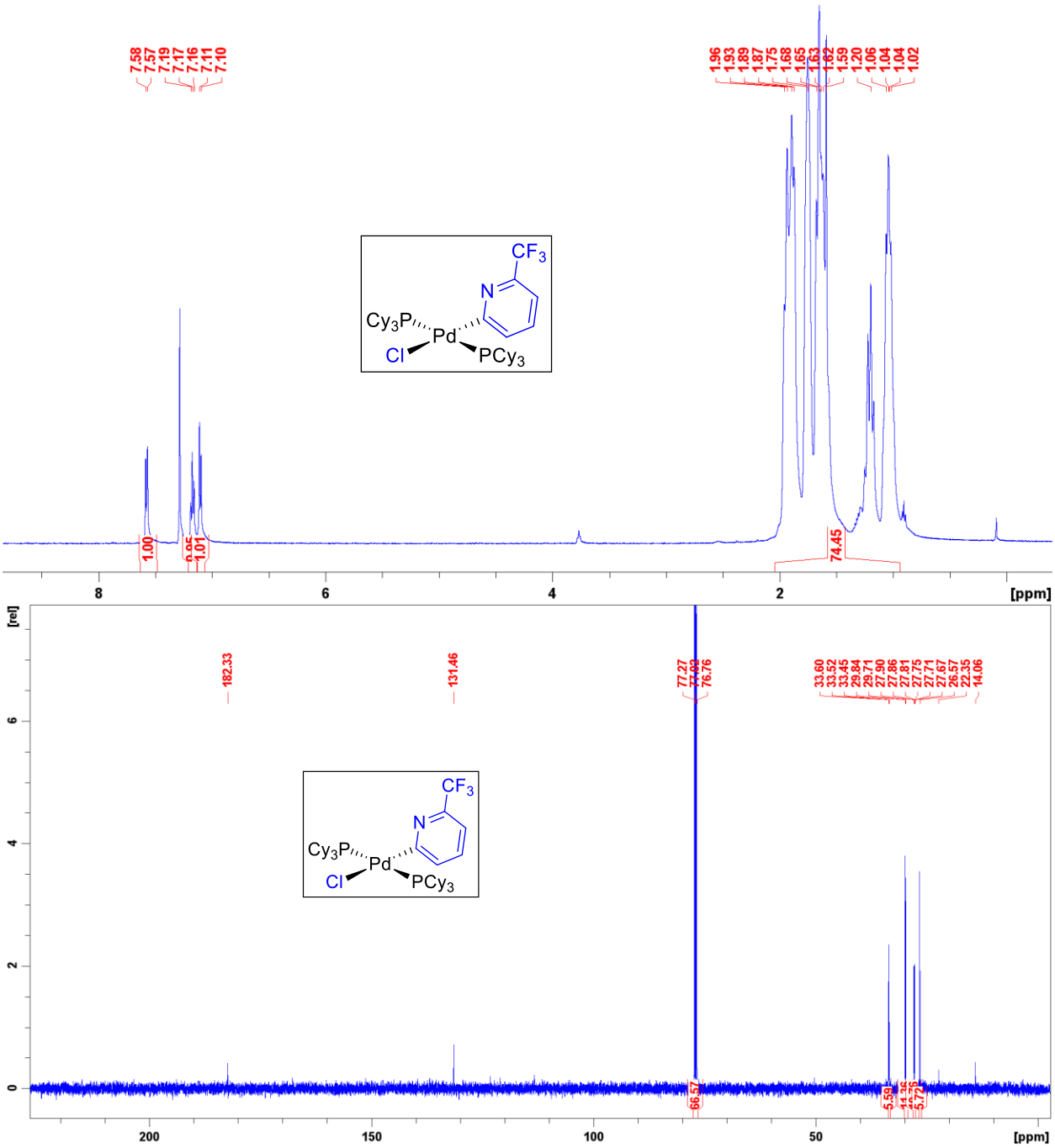

Fig. S15.
^{1}H (500 MHz, $CDCl_3$) and $^{13}C\{^{1}H\}$ (126 MHz, $CDCl_3$) NMR spectra of **S3**.

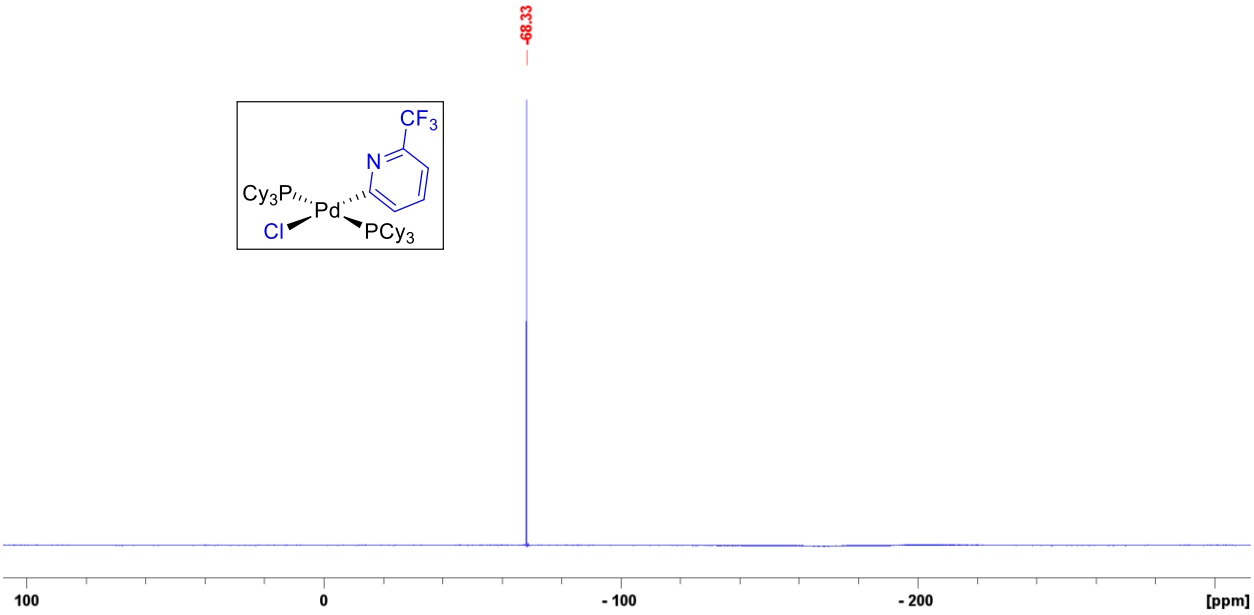

Fig. S16.
$^{19}F\{^{1}H\}$ (471 MHz, $CDCl_3$) NMR spectrum of **S3**.

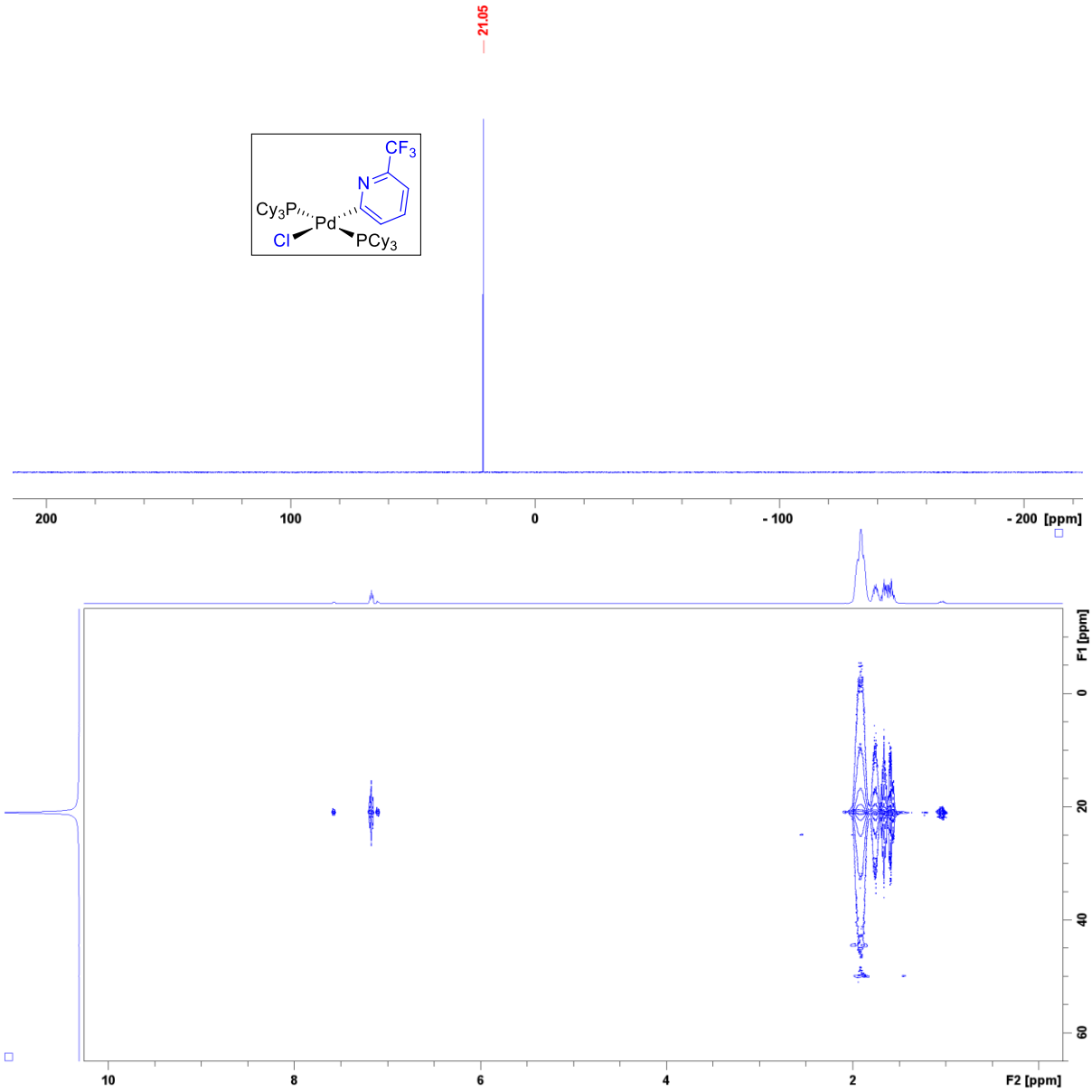

Fig. S17.
$^{31}P\{^{1}H\}$ NMR (203 MHz, $CDCl_3$) spectrum of **S3**, with accompanying long range ^{1}H-^{31}P HMBC NMR spectrum.

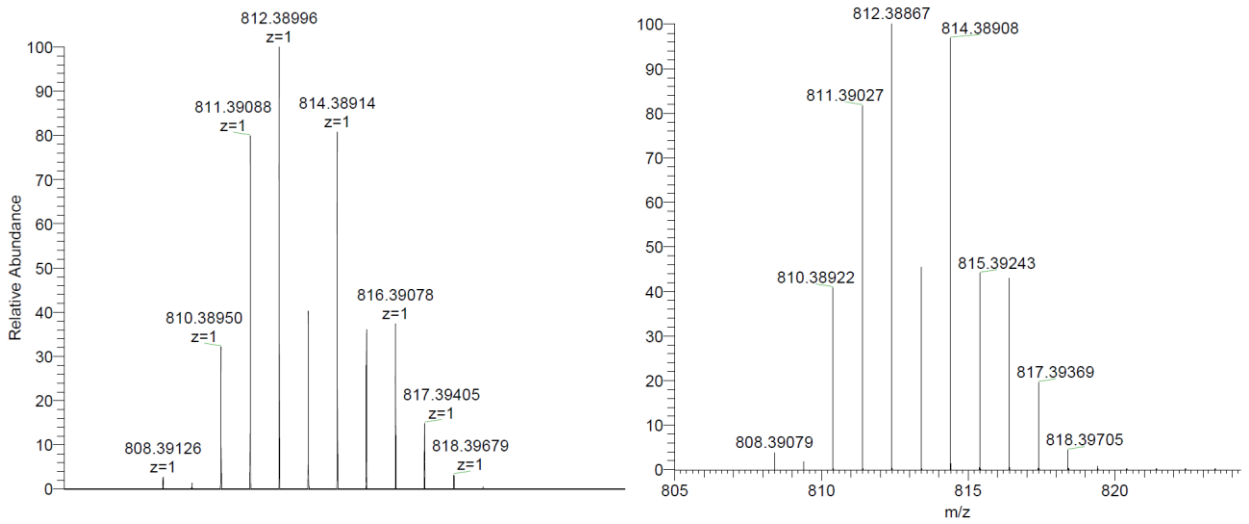

Fig. S18.
Left: Experimental HRMS-ESI spectrum of [**S3**-Cl]$^+$. Right: Calculated HRMS isotope pattern for [**S3**-Cl] $^+$.

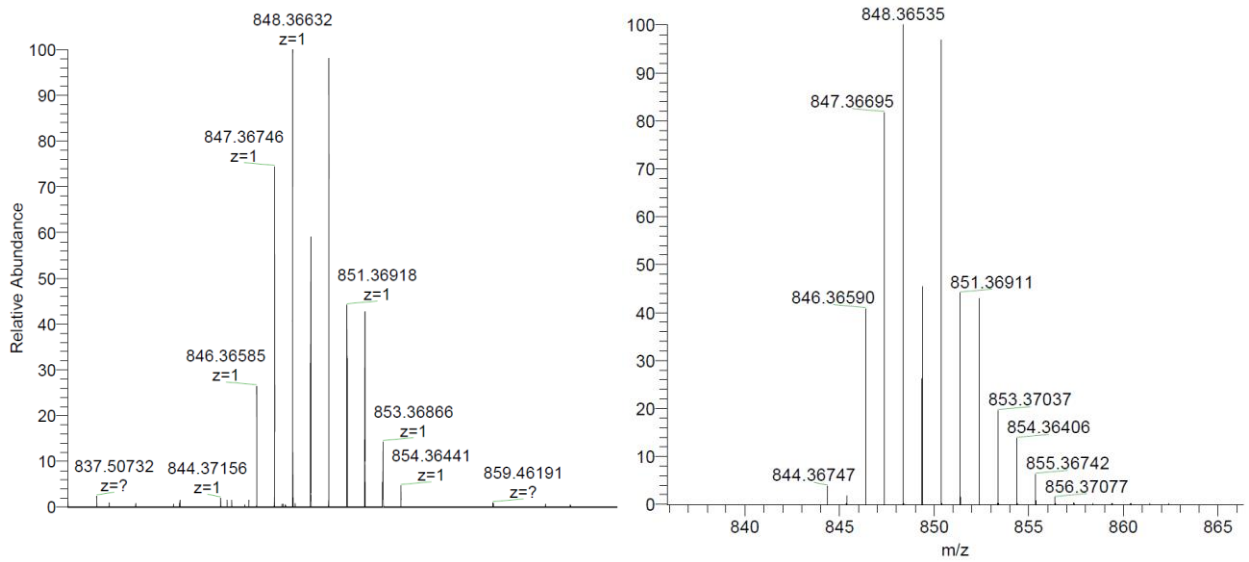

Fig. S19.
Left: Experimental HRMS-ESI spectrum of [**S3**+H]$^+$. Right: Calculated HRMS isotope pattern for [**S3**+H]$^+$.

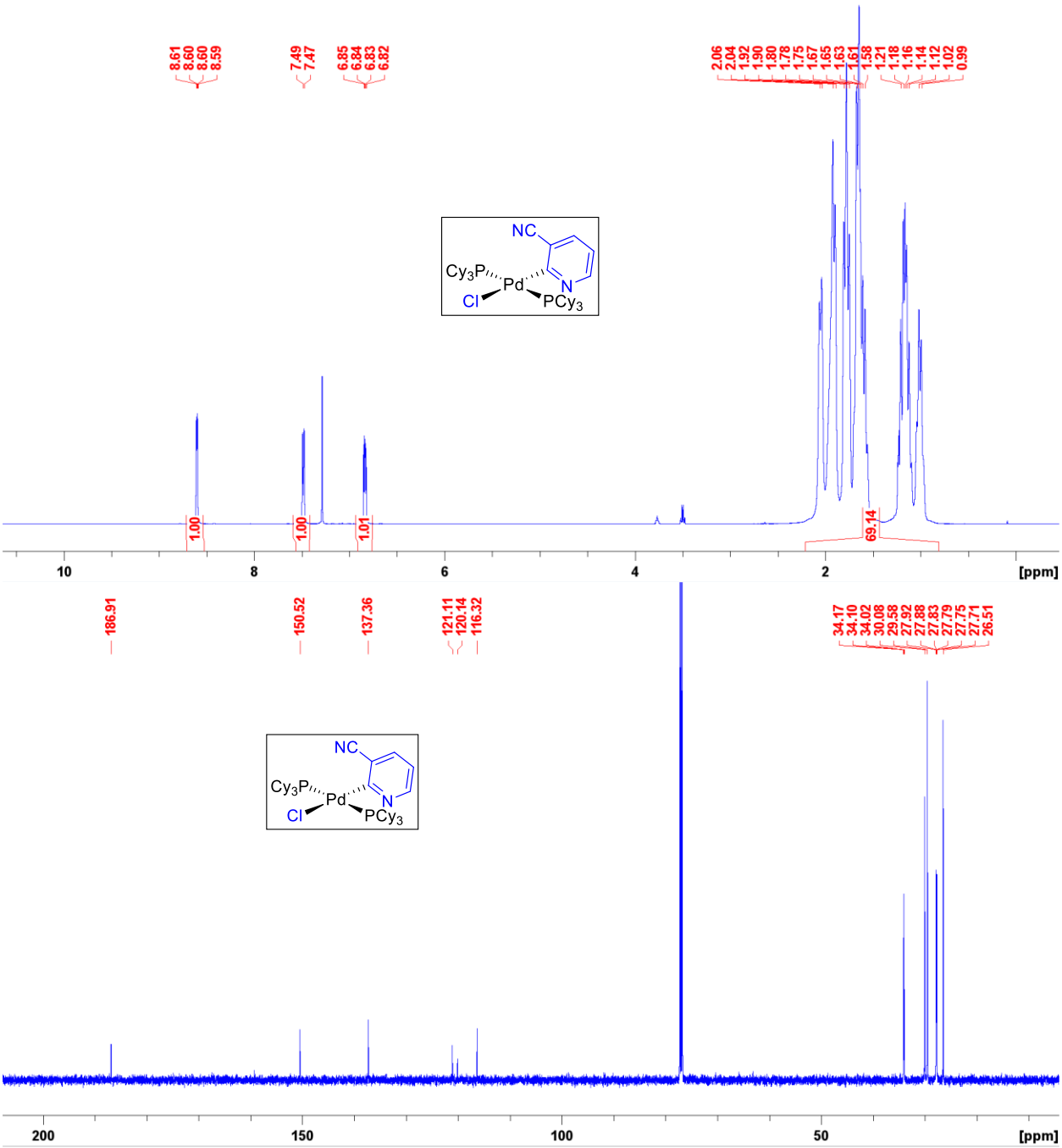

Fig. S20.
^{1}H (500 MHz, $CDCl_3$) and $^{13}C\{^{1}H\}$ (126 MHz, $CDCl_3$) NMR spectra of **S4**.

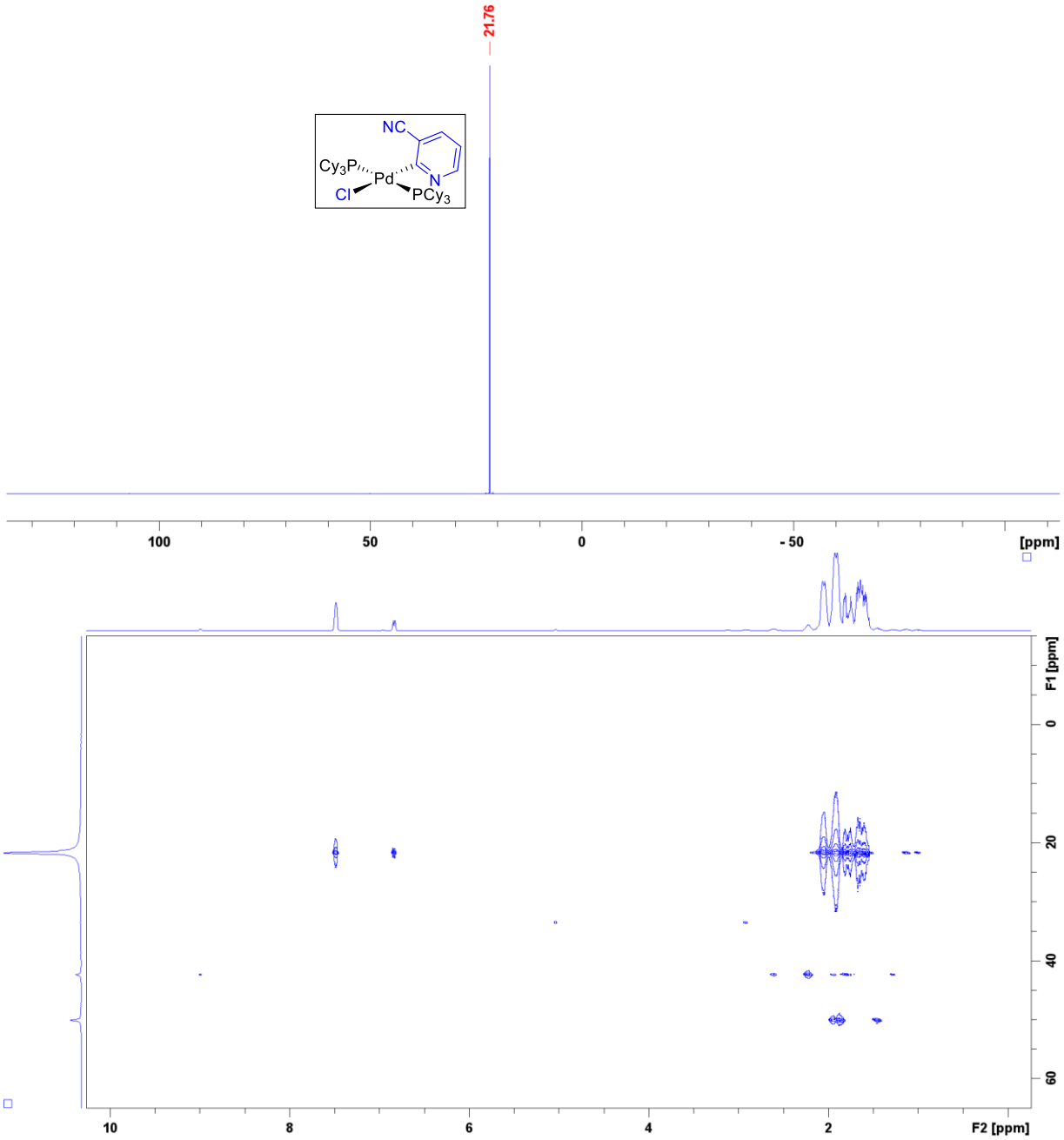

Fig. S21.
$^{31}P\{^{1}H\}$ NMR (203 MHz, $CDCl_3$) spectrum of **S4**, with accompanying long range ^{1}H-^{31}P HMBC NMR spectrum.

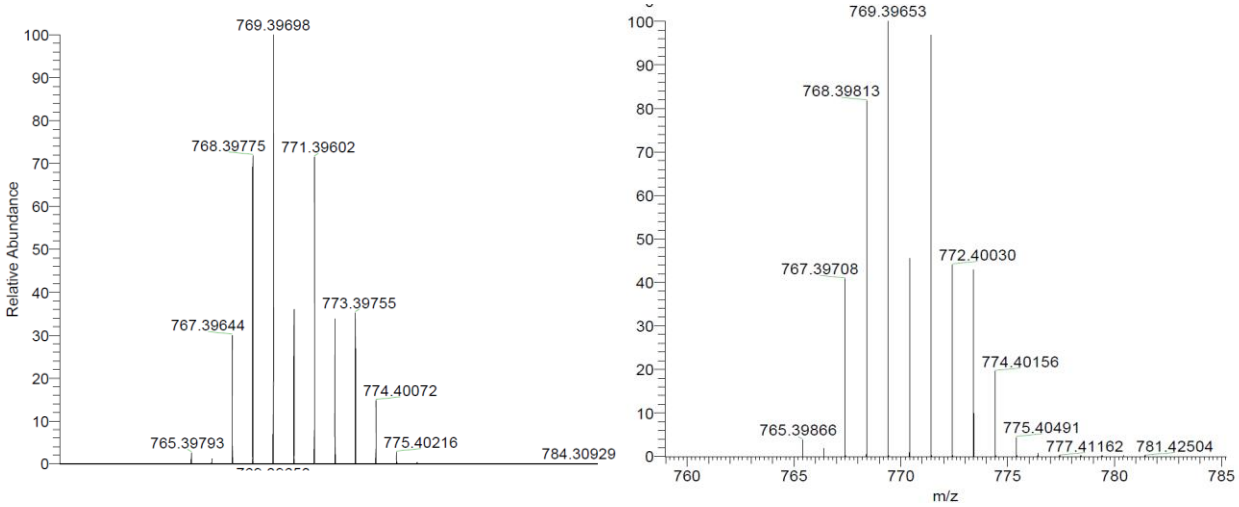

Fig. S22.
Left: Experimental HRMS-ESI spectrum of [**S4**-Cl]$^{+}$. Right: Calculated HRMS isotope pattern for [**S4**-Cl] $^{+}$.

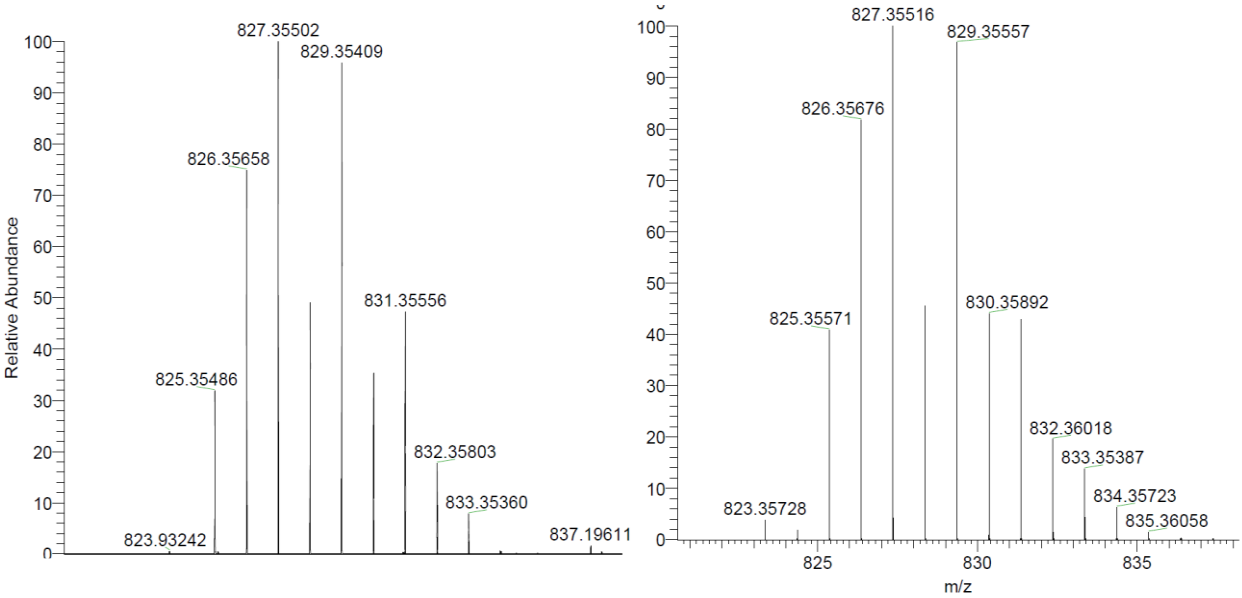

Fig. S23.
Left: Experimental HRMS-ESI spectrum of [**S4**+Na]$^{+}$. Right: Calculated HRMS isotope pattern for [**S4**+Na] $^{+}$.

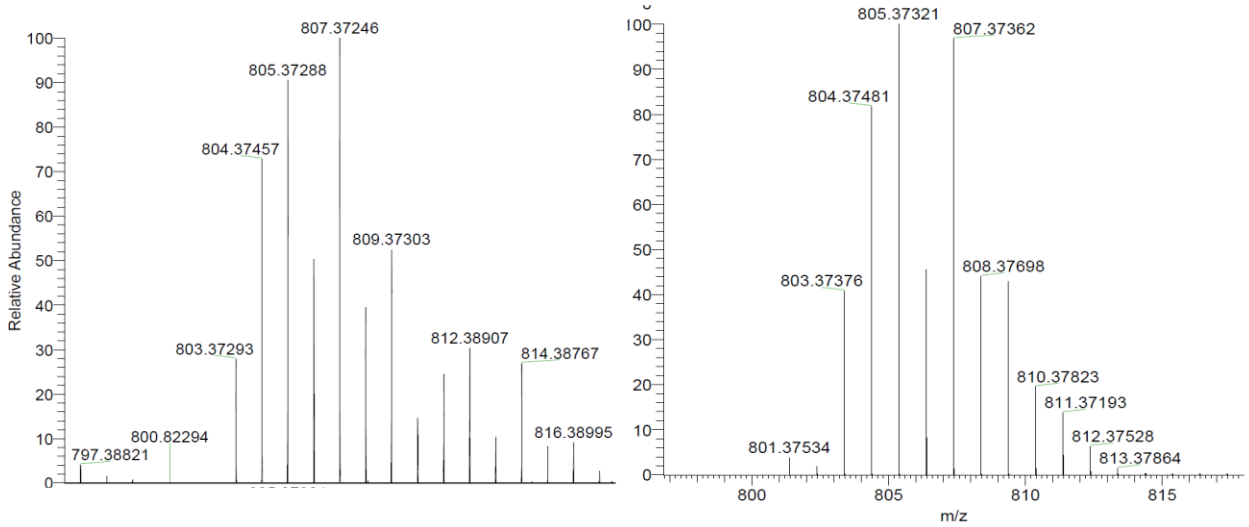

Fig. S24.
Left: Experimental HRMS-ESI spectrum of [**S4**+H]$^+$. Right: Calculated HRMS isotope pattern for [**S4**+H]$^+$.

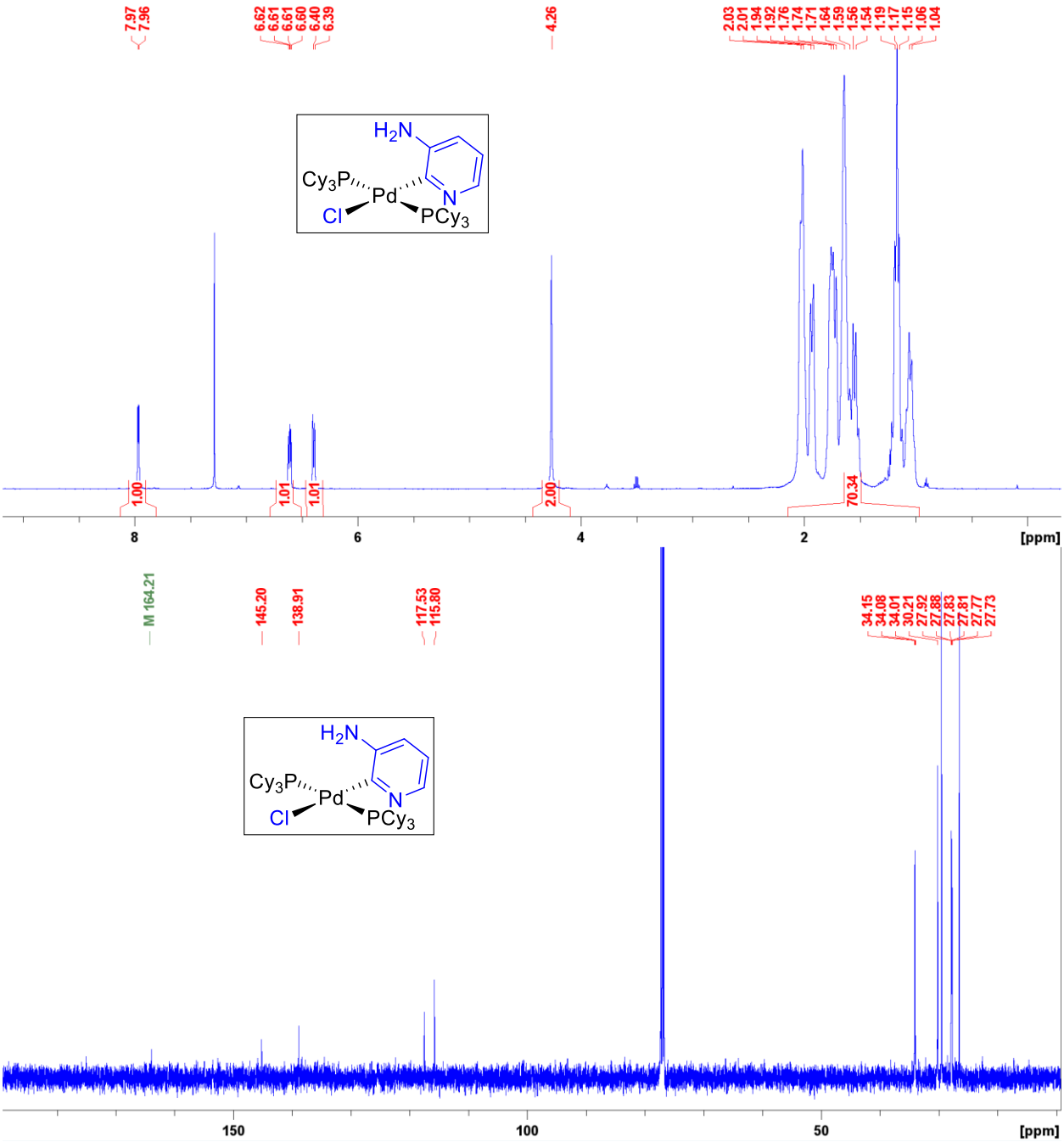

Fig. S25.
^{1}H (500 MHz, $CDCl_3$) and $^{13}C\{^{1}H\}$ (126 MHz, $CDCl_3$) NMR spectra of **S5**.

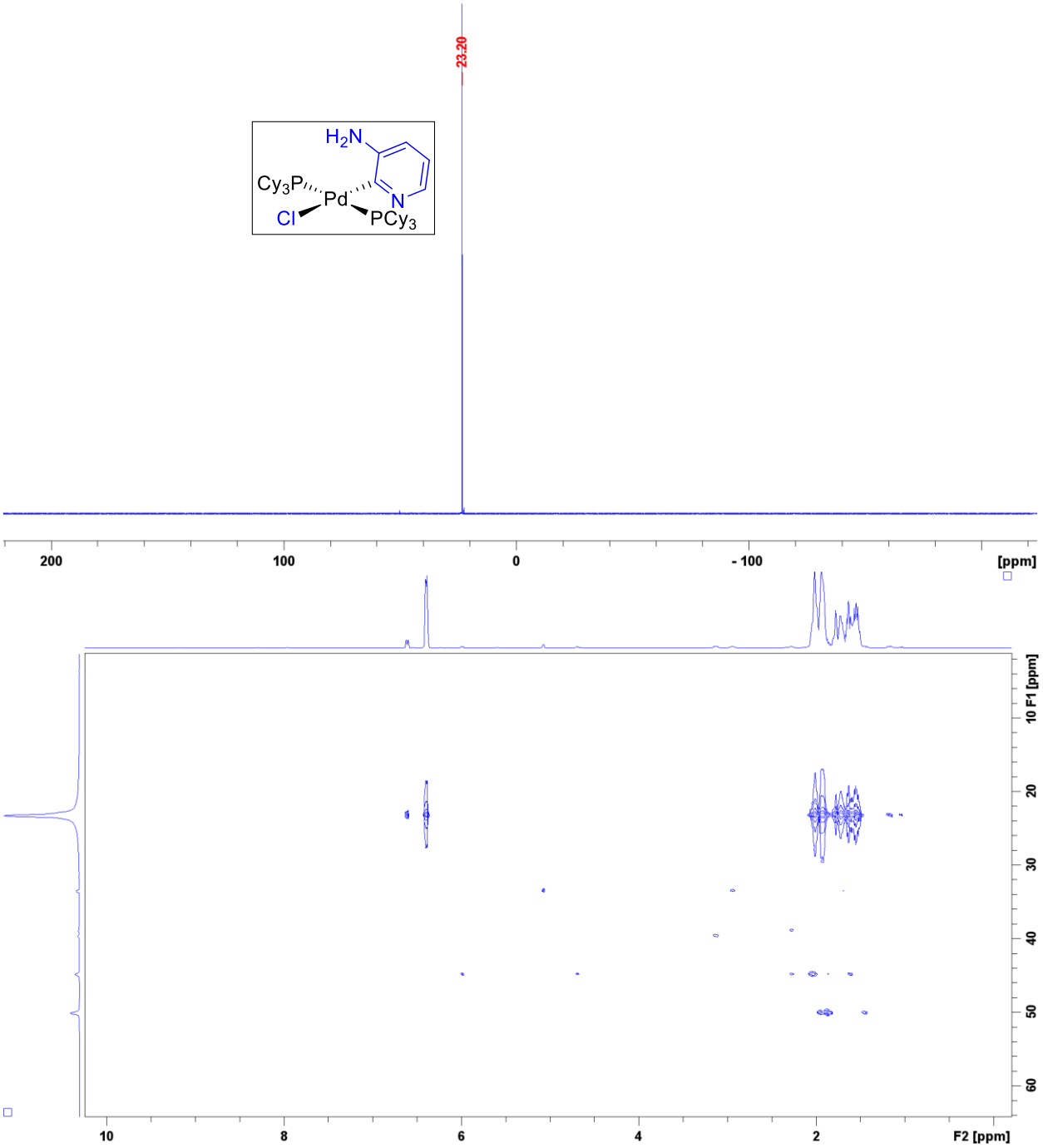

Fig. S26.
$^{31}P\{^{1}H\}$ NMR (203 MHz, $CDCl_3$) spectrum of **S5**, with accompanying long range ^{1}H-^{31}P HMBC NMR spectrum.

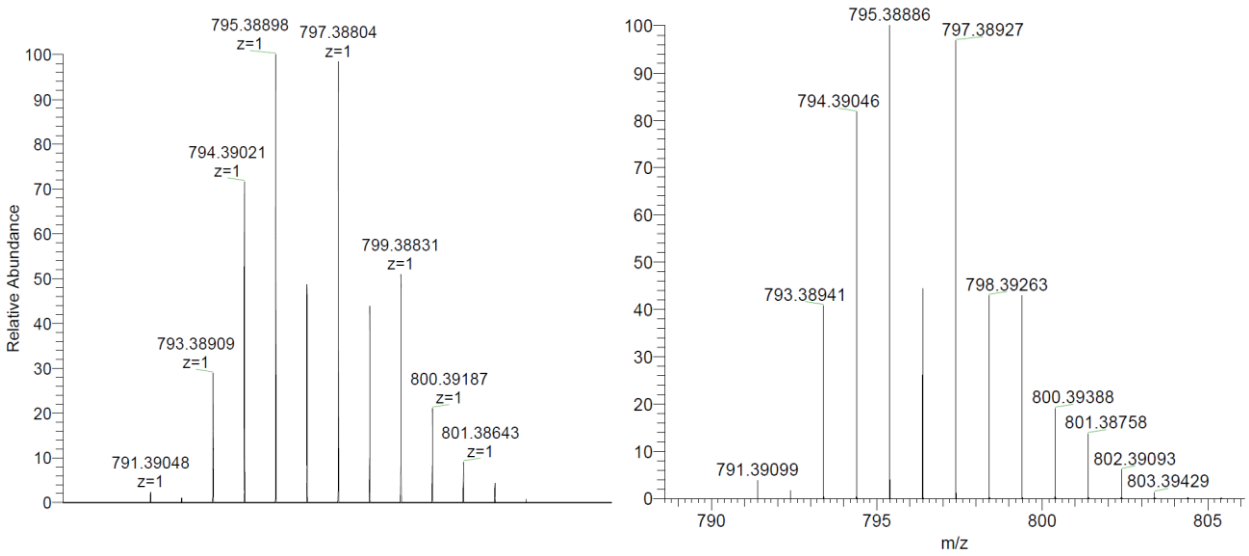

Fig. S27.
Left: Experimental HRMS-ESI spectrum of [**S5**+H]$^+$. Right: Calculated HRMS isotope pattern for [**S5**+H]$^+$.

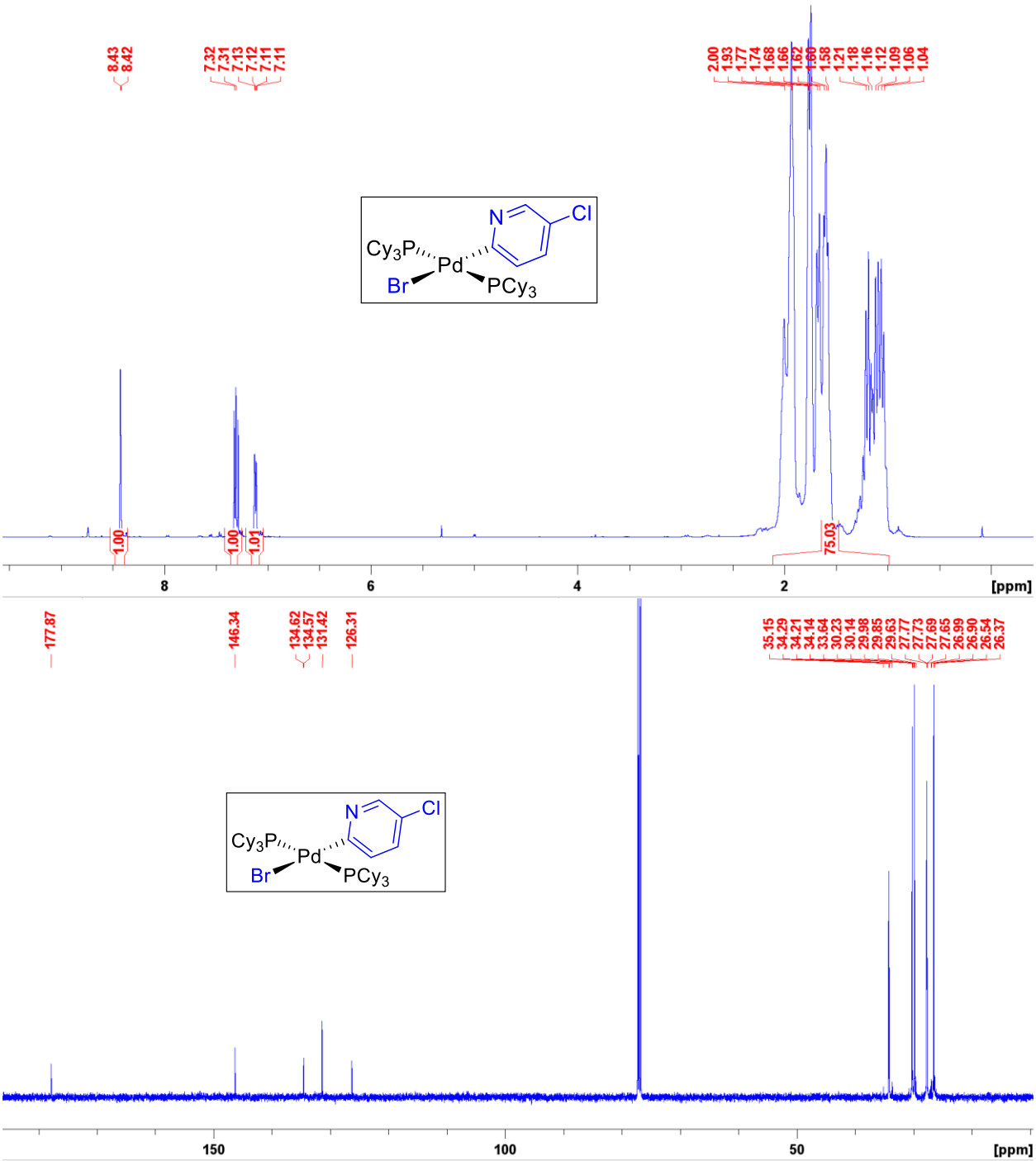

Fig. S28.
^{1}H (500 MHz, $CDCl_3$) and $^{13}C\{^{1}H\}$ (126 MHz, $CDCl_3$) NMR spectra of **S6**.

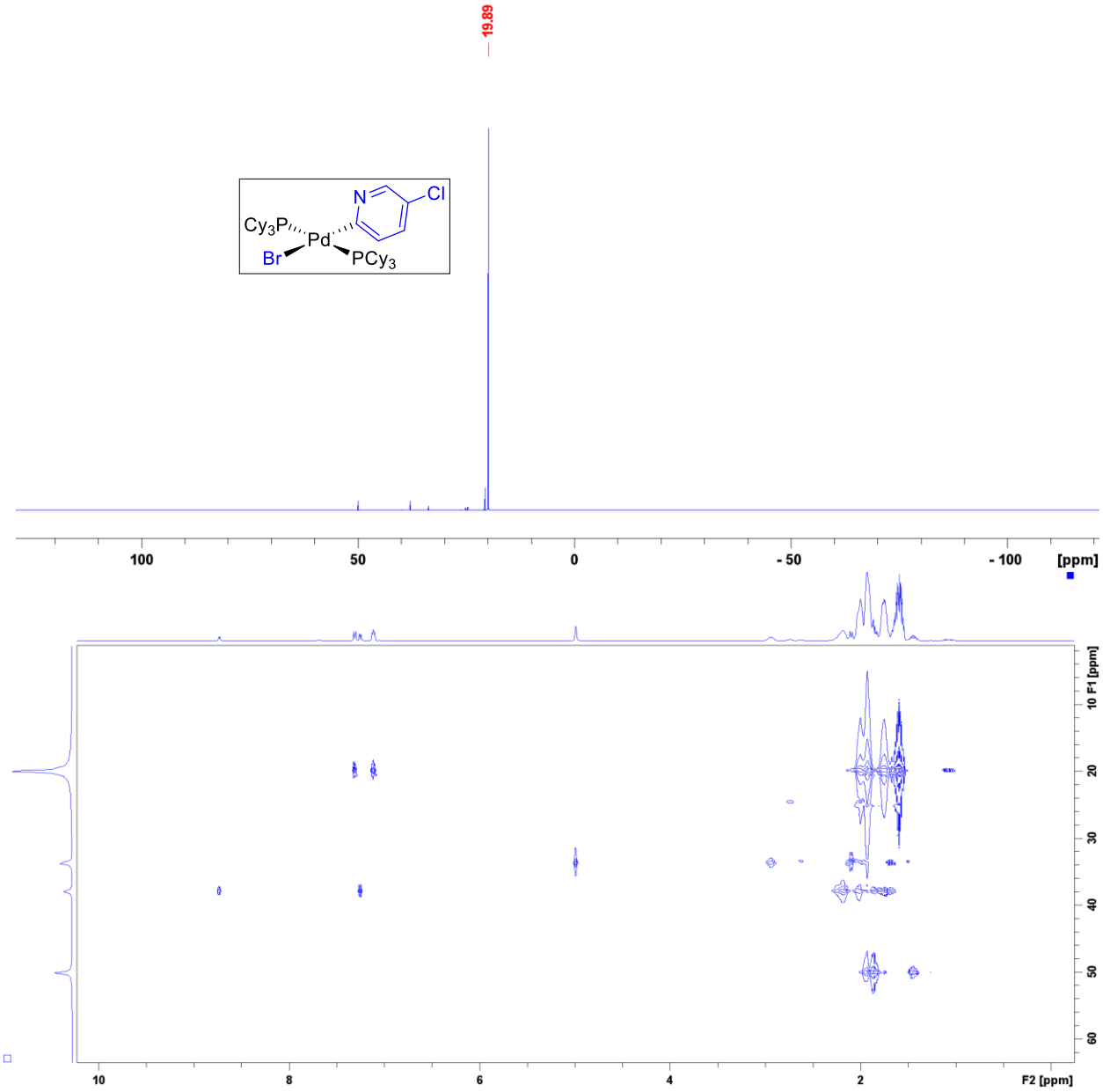

Fig. S29.
$^{31}P\{^{1}H\}$ NMR (203 MHz, $CDCl_3$) spectrum of **S6**, with accompanying long range ^{1}H-^{31}P HMBC NMR spectrum.

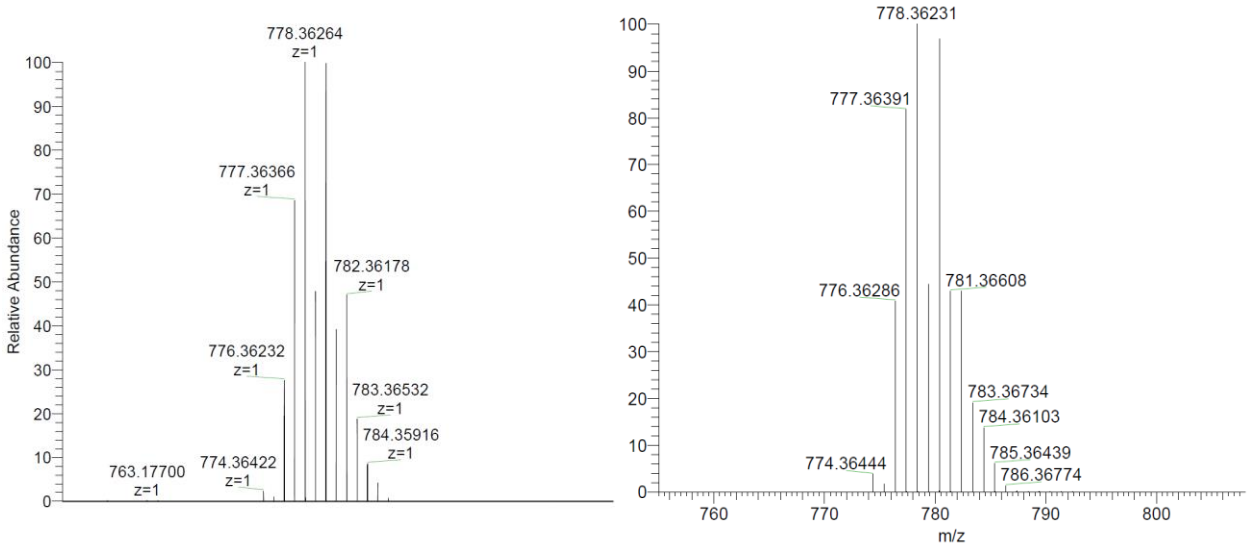

Fig. S30.
Left: Experimental HRMS-ESI spectrum of [**S6**-Br]$^+$. Right: Calculated HRMS isotope pattern for [**S6**-Br]$^+$.

Computational Determination of Molecular Descriptors

All geometry optimizations were performed using ORCA 4.0.1.2[9]. Initial substrate structures were either downloaded from the ChemSpider database[13] or generated using Avogadro version 4.1.[14] Geometry optimizations were performed in ORCA with a B3LYP/def-TVZPD approach. Wavefunction *.wfn* files were generated with the ORCA_2aim utility and imported in the Multiwfn program version 3.7[10-11] for calculation of electrostatic potential (*ESP*) and intrinsic bond strength index (*IBSI*). A-values were obtained from published tables.[12]

The molecular *ESP* was calculated at a 0.004 au isosurface of electron density. Surface properties for individual atoms were selected, including the atom-based surface area and the maximal, minimal and average *ESP* values at that surface Average *ESP* values at the reactive center (carbon) and its neighboring atom (nitrogen or carbon) were used as the electronic descriptors in construction of the oxidative addition predictive model. Electrostatic potential maps were plotted in VMD,[16] using electron density and *ESP* cube files generated by Multiwfn.

The *IBSI* was used as the bond strength descriptor between the reactive center (carbon) and the leaving group (Br, Cl, or OTf). *IBSI* is a recently proposed interpretation to quantify the bond strength of the covalent bonds.[15] The *IBSI* of the carbon-halogen bonds for each substrate was calculated using the Hirshfeld independent gradient model (IGMH) at high quality in Multiwfn.

To obtain molecular descriptors for the catalysts in the Sonogashira case study, the structures of three bisligated palladium(0) complexes $Pd(PCy_3)_2$, $Pd(P\textit{i}Pr_3)_2$ and $Pd(P\textit{t}Bu_3)_2$ were obtained from the literature.[17] The structures of the other 14 bisligated Pd(0) complexes were initially edited in Avogadro using one of the available structures as the starting point. Geometry optimizations of the 17 bisligated, 17 monoligated Pd(0) catalysts and 17 phosphine ligands were carried out using the B3LYP/def-TVZPD approach for all atoms except Pd. The LANL2DZ basis set with effective core potentials was used for Pd. Since effective core potentials are not supported by ORCA_2aim, single-point energy calculations with the all-electron relativistic ZORA-def2-TZVP basis set were carried out on the optimized geometries of Pd-containing compounds. *ESP* calculations for bisligated catalysts used a 0.01 au isosurface of electron density, whereas for monoligated catalysts and phosphine ligands a 0.004 au isosurface was used. The larger isosurface value for bisligated catalysts was due to the inability of the code to calculate surface areas of the buried Pd center. The $\%V_{bur}$ descriptor (*30*) is calculated using Sambvca (*49*).

A complete list of the molecular descriptors for the 79 oxidative addition substrates is given in Table S4. The descriptors for the 17 phosphine ligands and the corresponding PdL_2 and PdL complexes is given in Table S6.

Table S4.
Calculated molecular descriptors for the 70 (hetero)aryl halide and 9 aryl triflate substrates used in oxidative addition experiments.
** pKa of HCl, HBr and HOTf is 0.2, -4.4, -11.3, respectively.[18]

Substrate	Average ESP_1 (kJ/mol)	Average ESP_2 (kJ/mol)	$A_1 + A_2$ (kJ/mol)	*IBSI* (unitless)
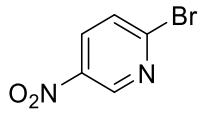 2-bromo-5-nitropyridine	98.660	-19.696	0.000	0.231
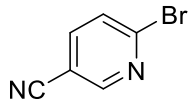 2-bromo-5-cyanopyridine	90.676	-24.540	0.000	0.229
 2-bromo-3-cyanopyridine	88.828	-30.058	0.837	0.231
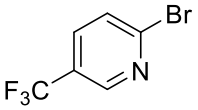 2-bromo-5-trifluoromethylpyridine	74.389	-40.404	0.000	0.227
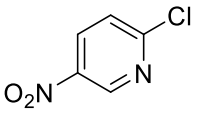 2-chloro-5-nitropyridine	105.023	-22.702	0.000	0.303
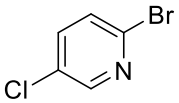 2-bromo-5-chloropyridine	55.957	-53.789	0.000	0.223
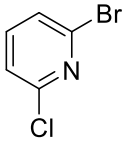 2-bromo-6-chloropyridine	57.614	-51.672	2.218	0.226
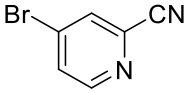 4-bromo-2-cyanopyridine	98.137	86.644	0.000	0.236
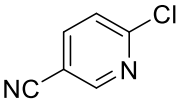 2-chloro-5-cyanopyridine	96.677	-27.765	0.000	0.304

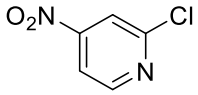 2-chloro-4-nitropyridine	97.947	-25.606	0.000	0.298
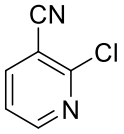 2-chloro-3-cyanopyridine	95.859	-31.214	0.837	0.304
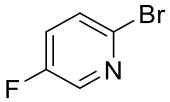 2-bromo-5-fluoropyridine	52.364	-55.903	0.000	0.223
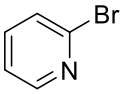 2-bromopyridine	35.522	-76.232	0.000	0.220
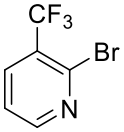 2-bromo-3-trifluoromethylpyridine	74.415	-45.460	10.460	0.222
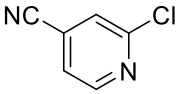 2-chloro-4-cyanopyridine	91.931	-31.338	0.000	0.305
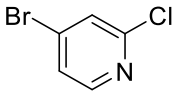 4-bromo-2-chloropyridine	68.426	52.924	0.000	0.230
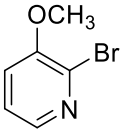 2-bromo-3-methoxypyridine	34.397	-77.970	3.138	0.224
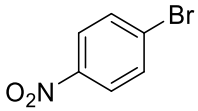 4-bromonitrobenzene	72.672	61.623	0.000	0.232
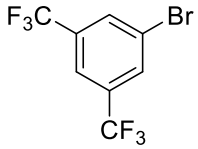 1-bromo-3,5-bis(trifluoromethyl)benzene	81.762	82.032	0.000	0.235

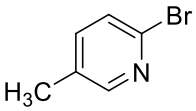 2-bromo-5-methylpyridine	24.367	-83.973	0.000	0.222
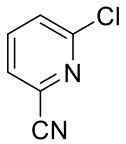 2-chloro-6-cyanopyridine	91.913	-28.075	0.837	0.301
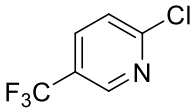 2-chloro-5-trifluoromethylpyridine	80.543	-43.848	0.000	0.288
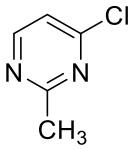 4-chloro-2-methylpyrimidine	67.990	-54.141	7.280	0.299
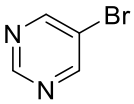 5-bromopyrimidine	77.070	79.110	0.000	0.239
 2-chloro-3-fluoropyridine	61.003	-62.007	1.046	0.302
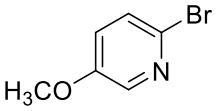 2-bromo-5-methoxypyridine	19.058	-85.678	0.000	0.217
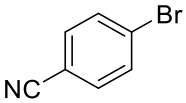 4-bromobenzonitrile	67.918	57.769	0.000	0.234
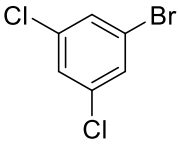 1-bromo-3,5-dichlorobenzene	51.321	43.572	0.000	0.231
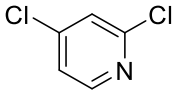 2,4-dichloropyridine	60.206	-62.712	0.000	0.306

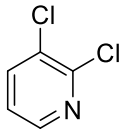 2,3-dichloropyridine	60.040	-61.379	2.218	0.303
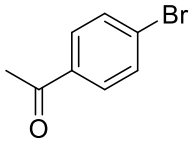 4-bromoacetophenone	38.035	22.523	0.000	0.232
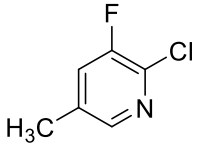 2-chloro-3-fluoro-5-methylpyridine	49.915	-70.751	1.046	0.300
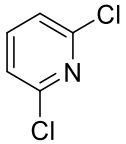 2,6-dichloropyridine	62.551	-54.769	2.218	0.295
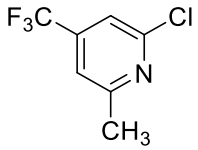 2-chloro-4-trifluormethyl-6-methylpyridine	66.410	-47.839	7.280	0.296
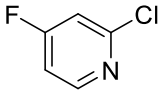 2-chloro-4-fluoropyridine	58.994	-64.978	0.000	0.294
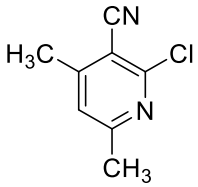 2-chloro-3-cyano-4,6-dimethylpyridine	74.392	-46.451	8.117	0.306
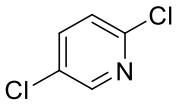 2,5-dichloropyridine	60.375	-57.739	0.000	0.294
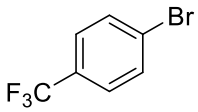 1-bromo-4-trifluoromethylbenzene	48.628	38.695	0.000	0.233

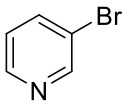 3-bromopyridine	41.774	34.990	0.000	0.234
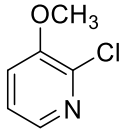 2-chloro-3-methoxypyridine	35.313	-88.282	3.138	0.287
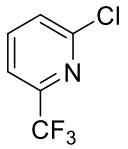 2-chloro-6-trifluoromethylpyridine	77.825	-44.139	10.460	0.284
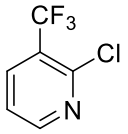 2-chloro-3-trifluoromethylpyridine	77.184	-46.988	10.460	0.300
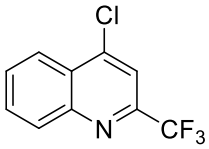 4-chloro-2-trifluoromethylquinoline	75.268	61.737	0.000	0.312
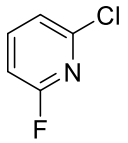 2-chloro-6-fluoropyridine	61.366	-56.026	1.046	0.296
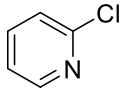 2-chloropyridine	38.816	-79.834	0.000	0.293
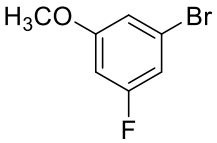 1-bromo-3-fluoro-5-methoxybenzene	28.071	19.917	0.000	0.233
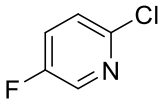 2-chloro-5-fluoropyridine	56.149	-59.580	0.000	0.293

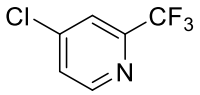 4-chloro-2-trifluoromethylpyridine	88.136	71.900	0.000	0.311
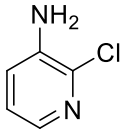 2-chloro-3-aminopyridine	23.379	-96.824	5.146	0.285
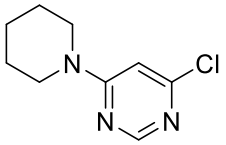 4-chloro-6-(piperidin-1-yl)pyrimidine	25.309	-104.265	0.000	0.277
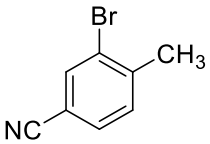 3-bromo-4-methylbenzonitrile	57.464	50.704	7.280	0.234
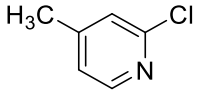 2-chloro-4-methylpyridine	28.976	-90.598	0.000	0.297
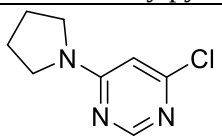 4-Chloro-6-(pyrrolidin-1-yl)pyrimidine	22.635	-106.399	0.000	0.288
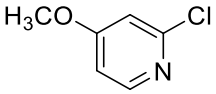 2-chloro-4-methoxypyridine	27.656	-96.650	0.000	0.287
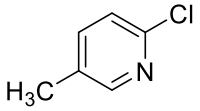 2-chloro-5-methylpyridine	27.598	-87.930	0.000	0.296
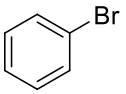 bromobenzene	8.664	-1.260	0.000	0.229
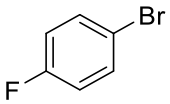 1-bromo-4-fluorobenzene	24.813	20.439	0.000	0.230

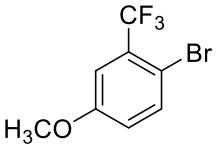 2-bromo-5-methoxy-1-trifluoromethylbenzene	28.273	22.861	10.460	0.232
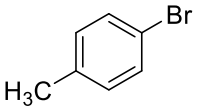 4-bromotoluene	-0.306	-8.976	0.000	0.231
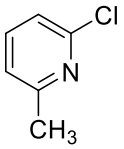 2-chloro-6-methylpyridine	29.530	-82.063	7.280	0.295
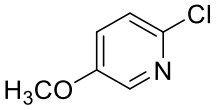 2-chloro-5-methoxypyridine	24.225	-86.190	0.000	0.287
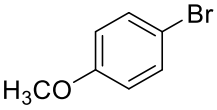 4-bromoanisole	-4.712	-10.511	0.000	0.220
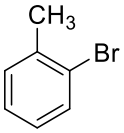 2-bromotoluene	4.239	-9.733	7.280	0.226
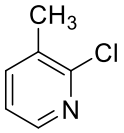 2-chloro-3-methylpyridine	34.384	-88.437	7.280	0.298
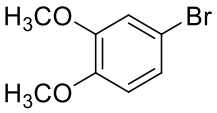 1-bromo-3,4-dimethoxybenzene	-13.889	-24.978	0.000	0.225
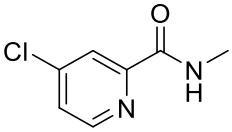 *N*-methyl-4-chloropyridine-2-carboxamide	68.474	48.636	0.000	0.311

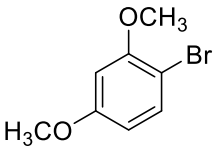 1-bromo-2,4-dimethoxybenzene	-3.385	-12.223	3.138	0.229
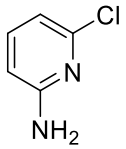 2-chloro-6-aminopyridine	12.770	-83.663	5.146	0.292
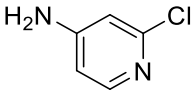 2-chloro-4-aminopyridine	6.431	-116.123	0.000	0.286
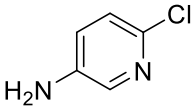 2-chloro-5-aminopyridine	10.418	-97.479	0.000	0.293
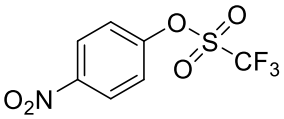 4-nitrophenyl triflate	113.204	78.161	0.000	0.424
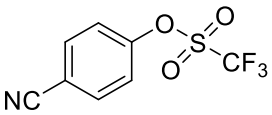 4-cyanophenyl triflate	105.487	72.186	0.000	0.409
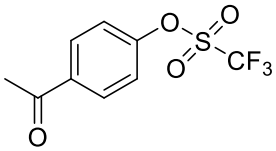 4-acetylphenyl triflate	77.539	39.481	0.000	0.439
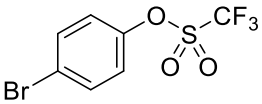 4-bromophenyl triflate	72.369	42.312	0.000	0.416
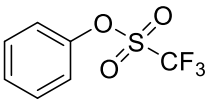 phenyl triflate	51.123	19.637	0.000	0.401
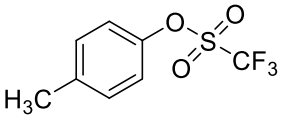 p-Tolyl triflate	41.303	11.797	0.000	0.400

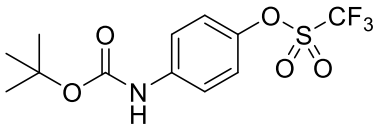 4-(N-Boc-amino)phenyl triflate	42.613	14.768	0.000	0.393
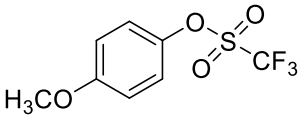 4-methoxyphenyl triflate	36.527	12.287	0.000	0.413
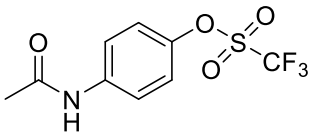 4-acetamidophenyl triflate	43.757	11.417	0.000	0.412

For substrates where ESP_2 values at the two adjacent carbon atoms are different, the smaller ESP value is used as ESP_2 in constructing the linear regression model in order to give smaller $\Delta G^{\ddagger}_{OA}$.
The ESP values at the two adjacent atoms, the predicted $\Delta G^{\ddagger}_{OA}$ using both ESP values, and the absolute difference between the two $\Delta G^{\ddagger}_{OA}$ values are shown below in Table S5 for comparison, confirming that the selection of one or the other ESP_2 value does not appreciably change the predicted $\Delta G^{\ddagger}_{OA}$.

Table S5.

Substrate	**Average *ESP₂* (kJ/mol)**	***Predicted* $\Delta G^{\ddagger}_{OA}$ (kJ/mol)**	***Absolute difference* (kJ/mol)**
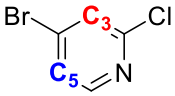 4-bromo-2-chloro-pyridine	C5: 52.924	16.868	0.372
	C3: 56.524	17.240	
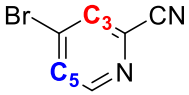 4-bromo-2-cyano-pyridine	C5: 86.644	9.566	0.464
	C3: 91.132	10.031	
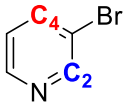 3-bromo-pyridine	C2: 34.990	26.579	0.546
	C4: 40.269	27.125	

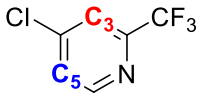 4-chloro-2-trifluoromethyl-pyridine	C5: 71.900	27.168	0.447
	C3: 76.2212	27.615	
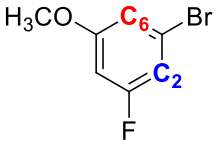 1-bromo-3-fluoro-5-methoxybenzene	C2: 19.917	30.492	0.271
	C6: 22.534	30.762	
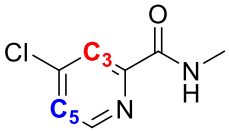 N-Methyl-4-chloropyridine-2-carboxamide	C5: 48.6364	32.838	0.932
	C3: 57.6509	33.770	
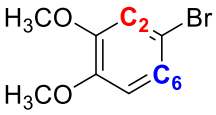 1-bromo-3,4-dimethoxybenzene	C6: -24.978	41.169	1.361
	C2: -11.822	42.530	

Table S6.
Calculated molecular descriptors for bisligated Pd(0) complexes (PdL_2), monoligated Pd(0) complexes (PdL) and phosphines (L) for the 17 ligands used in Sonogashira case study.

Phosphine ligand	PdL_2		PdL		L	
	ESP at Pd center (kJ/mol)	$\%V_{bur}$ centered at Pd	ESP at Pd center (kJ/mol)	$\%V_{bur}$ centered at Pd	ESP at P (kJ/mol)	$\%V_{bur}$ centered at P
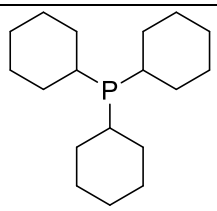 PCy_3	-72.401	49.2	37.810	36.7	-102.995	68.8
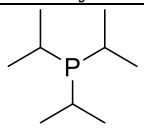 $P(iPr)_3$	-70.378	51.0	37.633	34.4	-110.492	68.6
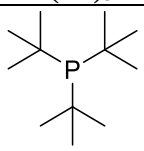 $P(tBu)_3$	-62.680	61.9	53.761	40.2	-126.782	78.0
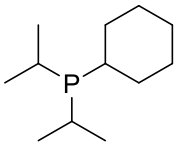 $PCy(iPr)_2$	-66.714	55.5	31.687	34.5	-114.273	69.0
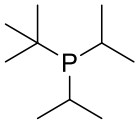 $P(tBu)(iPr)_2$	-60.957	60.2	44.907	36.7	-110.739	72.1
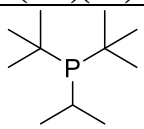 $P(iPr)(tBu)_2$	-59.244	63.9	53.804	39.4	-120.319	75.8
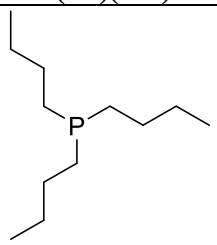 $P(nBu)_3$	-65.053	45.7	19.934	30.9	-88.809	57.7

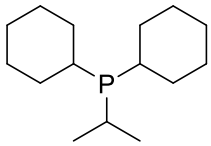 P(iPr)Cy_2	-68.618	56.8	38.392	36.5	-100.452	68.7
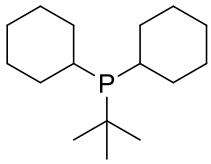 P(*t*Bu)Cy_2	-65.702	60.2	43.695	37.7	-114.880	72.5
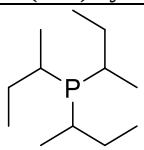 P(*s*Bu)$_3$	-63.053	59.8	36.917	34.9	-112.953	68.9
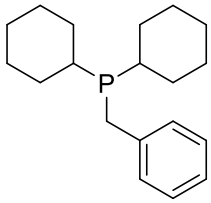 P$Bn Cy_2$	-49.272	58.4	39.637	36.2	-89.715	68.0
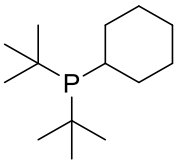 PCy(*t*Bu)$_2$	-56.902	64.4	53.408	39.5	-124.055	75.8
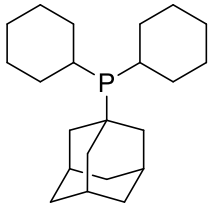 P$Ad Cy_2$	-69.809	61.1	40.893	37.7	-119.068	72.4
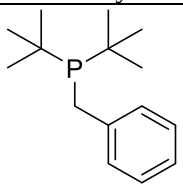 P$Bn(tBu)_2$	-54.494	59.7	46.967	36.7	-115.264	73.3

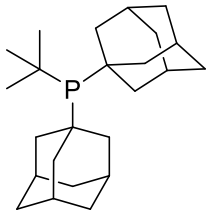 P(*t*Bu)Ad_2	-63.131	66.7	48.152	40.2	-134.066	78.1
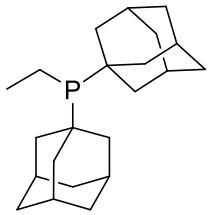 PEt$(Ad)_2$	-74.656	59.3	30.738	35.9	-127.605	72.1
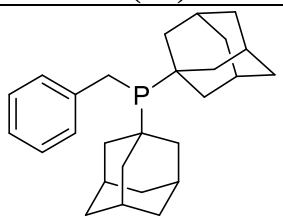 PBn$(Ad)_2$	-63.695	59.4	36.910	35.9	-119.559	73.0

Hammett Analyses of *para*-Substituted Substrates

To further validate the kinetic parameters obtained by competition experiments, we have obtained reaction constants (ρ) through construction of Hammett plots – $\log(k_Z/k_H)$ versus substituent σ values – for five sets of *para*-substituted substrates undergoing oxidative addition. These include: 5-substituted-2-chloro-pyridines, 5-substituted-2-bromo-pyridines, 4-substituted-1-bromo-benzenes, 4-substituted-2-chloropyridines and 4-substituted phenyl triflates. Substituent σ values were obtained from published tables.[19]

For oxidative addition of the 5-Z-2-Cl-pyridines, we obtain reaction constants of ρ = 4.8 in THF (Fig. S31). This is similar to the published value of ρ = 4.3 obtained for an analogous set of reactions using $Pd(PPh_3)_4$ in THF.[20]

For oxidative addition of the 5-Z-2-Br-pyridines, we obtain a reaction constant of ρ = 3.2 in THF (Fig. S32), which is smaller than the published value of ρ = 4.4 obtained for an analogous set of reactions using $Pd(PPh_3)_4$ in THF.[20]

For oxidative addition of the 4-Z-1-Br-benzenes, we obtain reaction constants of ρ = 3.4 in THF (Fig. S33). We also noted slightly worse linear correlation when using standard σ_{para} values (R^2 = 0.93). Plotting $\log(k_Z/k_H)$ versus σ_{para}^- gives better linear correlation (R^2 = 0.98), and reaction constant of ρ = 2.3 in THF (Fig. S34).

For oxidative addition of the 4-Z-2-Cl-pyridines, we plotted $\log(k_Z/k_H)$ versus both σ_{meta} and σ_{para} to assess the inductive effect of Z on the C–X position, and the resonance effect on the adjacent pyridine nitrogen. Using σ_{meta} (Fig. S35), we obtain reaction constant of ρ = 5.9 in THF, though with relatively poor linear correlation (R^2 = 0.92 in THF). In contrast, the Hammett plots using σ_{para} give better linear correlation (R^2 = 0.99 in THF), and reaction constant of ρ = 4.0 in THF (Fig. S36). This is comparable to the published value of ρ = 3.3 using $Pd(PPh_3)_4$ in THF (though this previous work only included 3 substrates).[20] The strong linear correlation for σ_{para} indicates that resonance stabilization of negative charge at N in the transition state accelerates the oxidative addition reaction. This is consistent with the proposed S_NAr-like mechanism, and further validates the inclusion of ESP_2 in our quantitative model.

For oxidative addition of the 4-Z-phenyl-triflates, we obtain reaction constant of ρ = 3.9 in THF (Fig. S37). We plotted $\log(k_Z/k_H)$ versus both σ_{para} and σ_{para}^- and noted slightly worse linear correlation when using standard σ_{para} values (R^2 = 0.93). Plotting $\log(k_Z/k_H)$ versus σ_{para}^- gives better linear correlation (R^2 = 0.98), and reaction constant of ρ = 2.3 in THF.

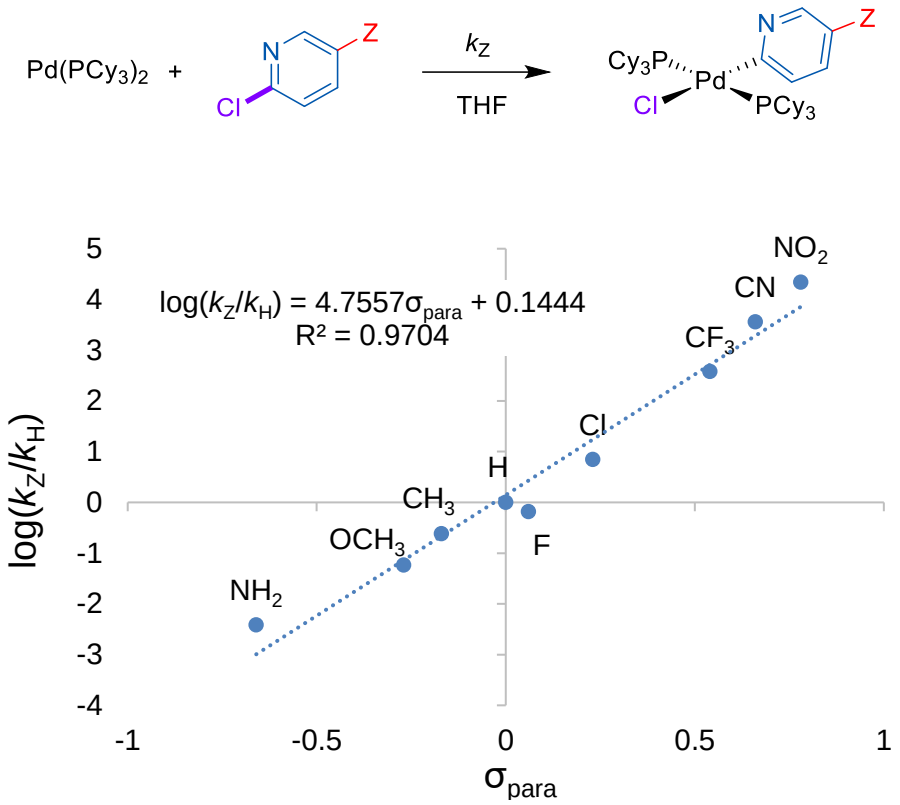

Fig. S31.
Hammett plot of log(k_Z/k_H) versus σ_{para} for oxidative addition of a group of 5-Z-2-chloropyridines.

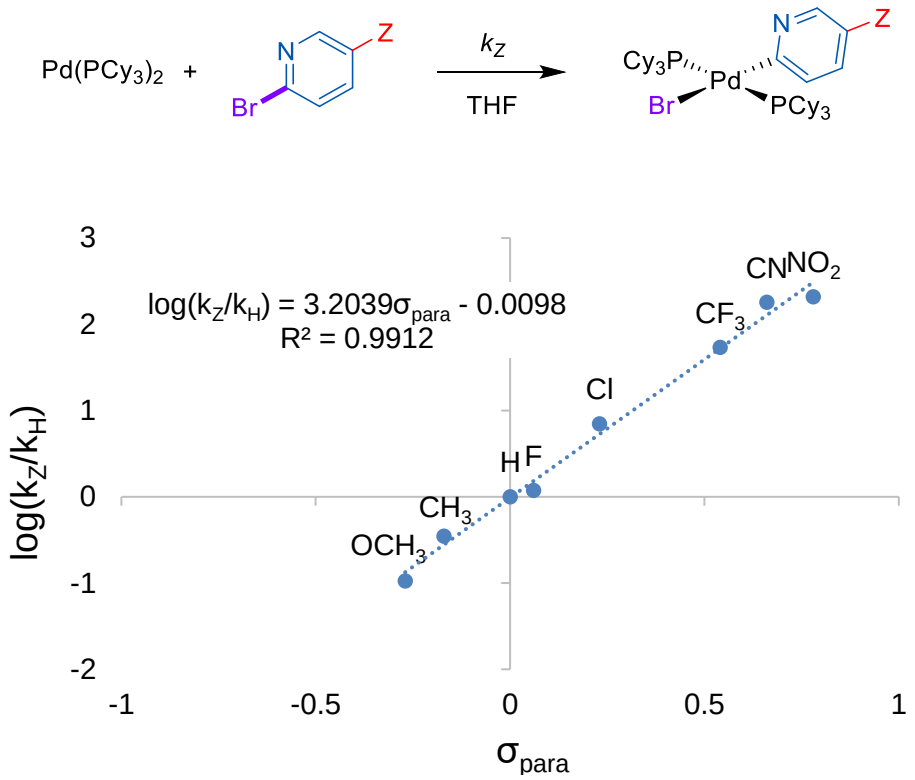

Fig. S32.
Hammett plot of log(k_Z/k_H) versus σ_{para} for oxidative addition of a group of 5-Z-2-bromopyridines.

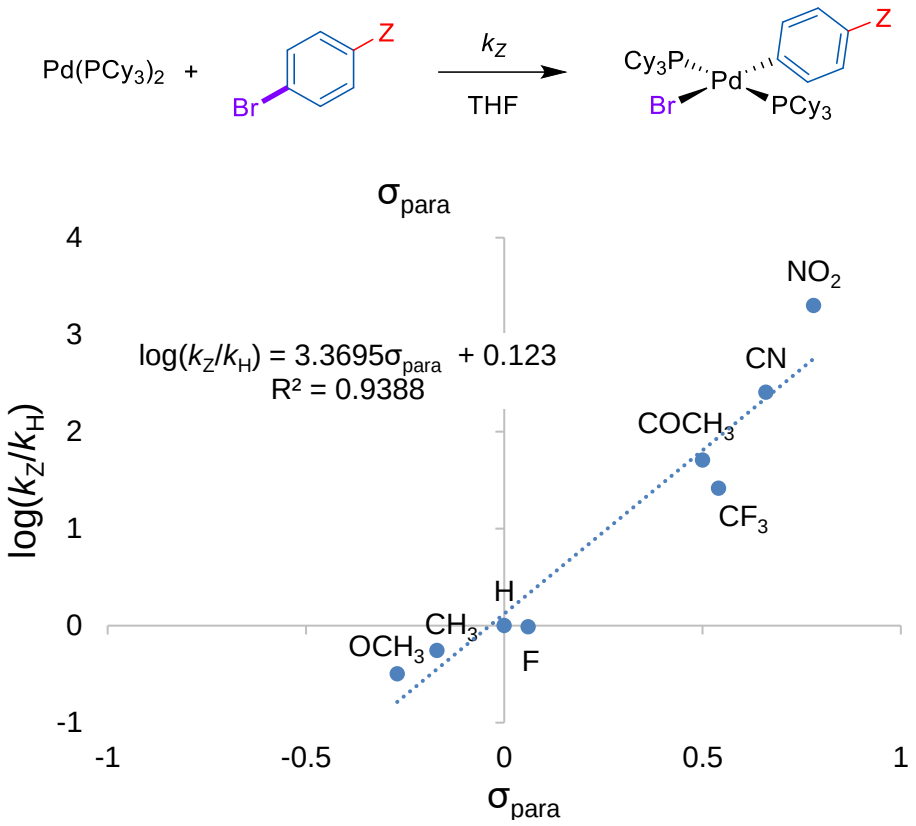

Fig. S33.
Hammett plot of log(k_Z/k_H) versus σ_{para} for oxidative addition of a group of 1-Z-4-bromobenzenes.

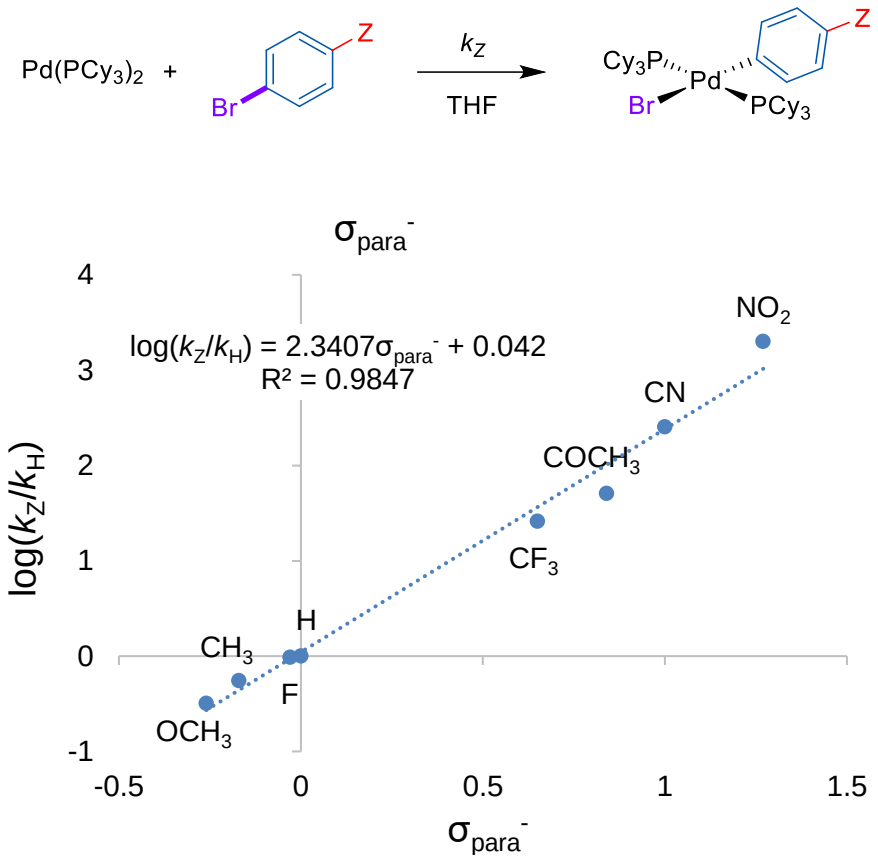

Fig. S34.
Hammett plot of log(k_Z/k_H) versus σ_{para}^- for oxidative addition of a group of 1-Z-4-bromobenzenes.

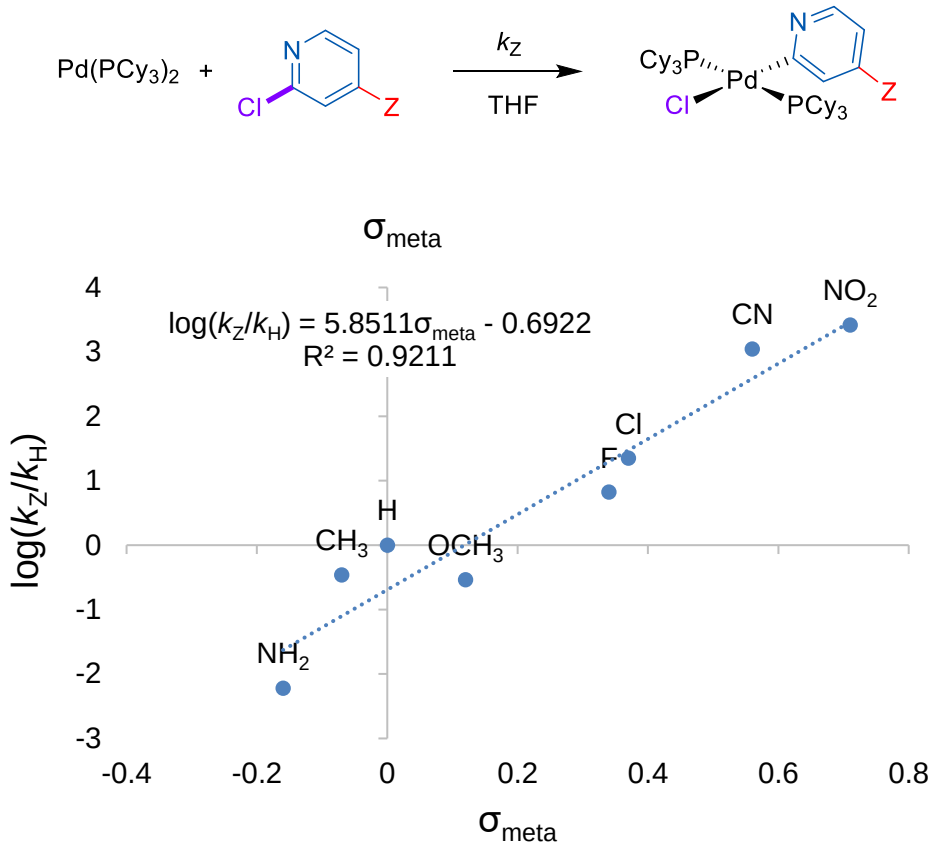

Fig. S35.
Hammett plot of log(k_Z/k_H) versus σ_{meta} for oxidative addition of a group of 4-Z-2-chloropyridines.

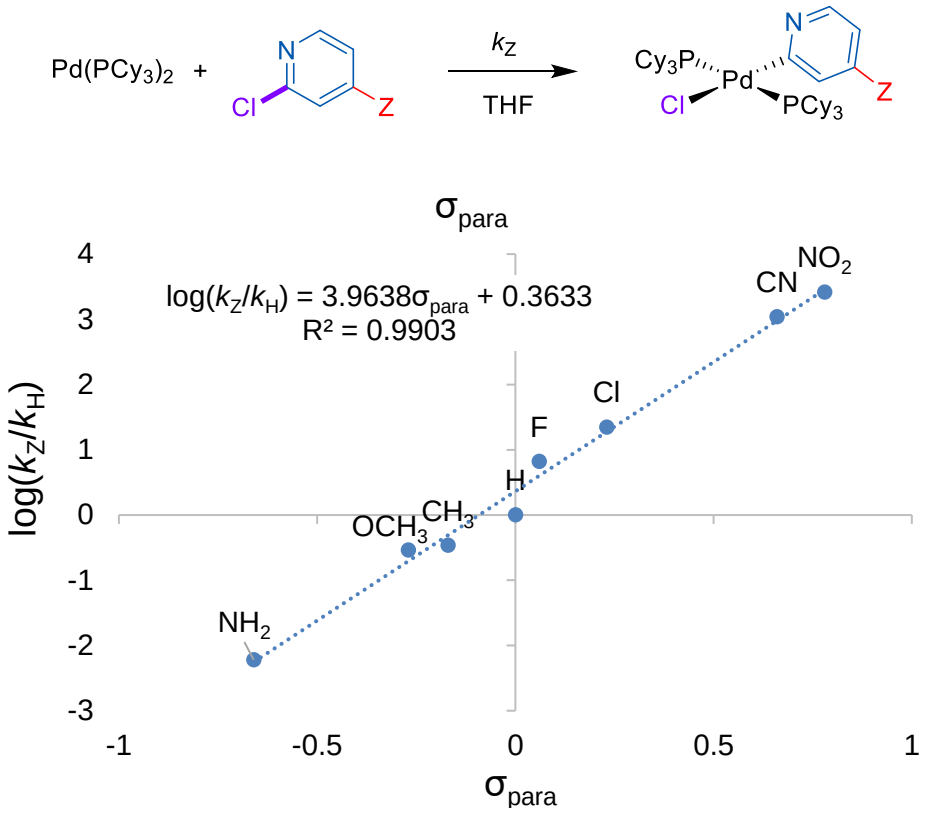

Fig. S36.
Hammett plots of log(k_Z/k_H) versus σ_{para} for oxidative addition of a group of 4-Z-2-chloropyridines.

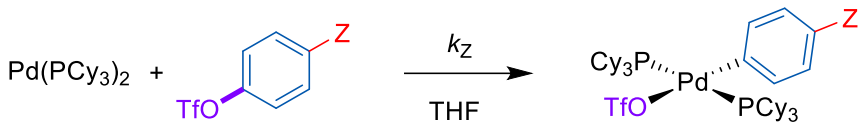

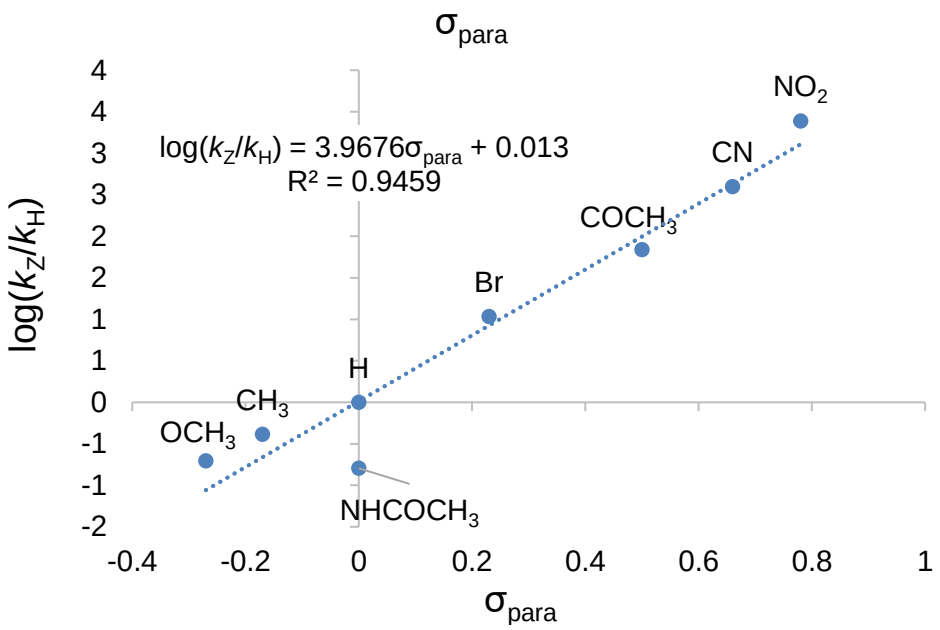

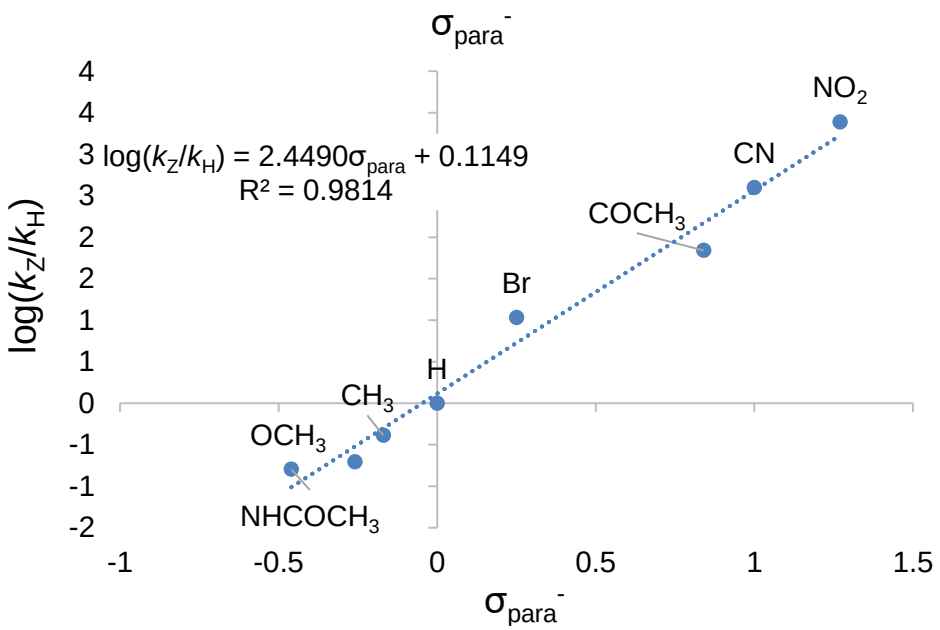

Fig. S37.
Hammett plots of log(k_Z/k_H) versus σ_{para} and σ_{para}^- for oxidative addition of a group of 4-Z-phenyl triflates.

π-Complex Intermediates and Transition States for Oxidative Addition

To assess the substrate-catalyst effects on the π-complex intermediate and oxidative addition transition states (Fig. 2A), we calculated the structures and *ESP* maps for 11 π-complexes and 6 transition states. To focus our analysis, we did not calculate the transition state for the coordination of the substrate to form the π-complex intermediate.

Transition state structures were obtained in ORCA 4.0.1.2[9] using relaxed scans with an RI BP86/def2-SVP approach with D3BJ dispersion for all atoms except for Pd, for which a def2-TZVP basis set was used. Single point calculations were then performed with a RI-B2PLYP/def2-TZVP approach with D3 dispersion to calculate TS energies. These structures were used for subsequent calculations of energies at the TZP level and average *ESP* values. An example input file to compute a geometry is provided below.

Geometry:
! RI BP86 def2-SVP def2/J D3BJ TIGHTSCF Opt Grid3 FinalGrid5
%basis newgto Pd "def2-TZVP" end end
Energy:
! RI-B2PLYP D3 def2-TZVP def2-TZVP/C TIGHTSCF

The bent geometry of the $Pd(PCy_3)_2$ starting structure (P–Pd–P bond angle of 160.3°) agrees with geometries previously reported in the literature.[17] Our π-complex intermediate structures and transition states are also consistent with previously reported geometries for related systems.[20]

To locate transition states for oxidative addition, different reaction coordinates were scanned depending on the nature of the aromatic substrate. For chlorinated pyridine substrates, the transition state of the oxidative addition step was found by stretching along the Cl-C2 bond axis to locate the "S_NAr-like" transition state. To locate the "3-centered" oxidative addition transition state for aryl bromides, we used a relaxed scan opening the C1-Pd-Br angle from the π-complex intermediate to the *cis* oxidative addition product; this *cis* complex then isomerizes to the more stable *trans* geometry (which is the experimentally observed geometry). The energies of the six intermediates and their corresponding transition states and products are given in Table S7. The simplified reaction coordinates for oxidative addition of the 2-chloropyridines and bromobenzenes are given in Figures S38 and S39 respectively. Overall, the trends in reactivity mirror those observed experimentally. One minor discrepancy is the transition state energy for 4-bromoanisole is slightly lower than for bromobenzene (3 kJ/mol difference), whereas the experimental $\Delta\Delta G^{\ddagger}$ is ~1.5 kJ/mol with bromobenzene lower than 4-bromoanisole.

Table S7.
Energies of key species in the oxidative addition pathway (kJ/mol), relative to the unbound substrate and $Pd(PCy_3)_2$.

	Energy (kJ/mol)			
Substrate	**π-complex Intermediate**	**Transition state**	**Product (*cis* geometry)**	**Product (*trans* geometry)**
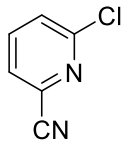 2-chloro-6-cyanopyridine	14	27	-103	-198
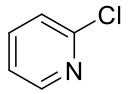 2-chloropyridine	18	36	-125	-164
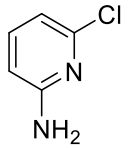 2-chloro-6-aminopyridine	45	57	-101	-179
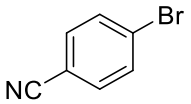 4-bromobenzonitrile	-9	15	-128	-206
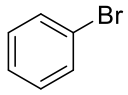 bromobenzene	11	34	-110	-190
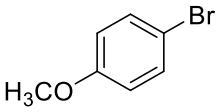 4-bromoanisole	7	31	-108	-157
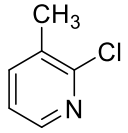 2-chloro-3-methylpyridine	-3	n/d	n/d	n/d

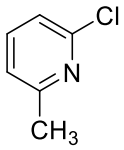 2-chloro-6-methylpyridine	9	n/d	n/d	n/d
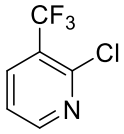 2-chloro-3-trifluoromethylpyridine	3	n/d	n/d	n/d
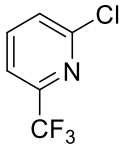 2-chloro-6-trifluoromethylpyridine	2	n/d	n/d	n/d
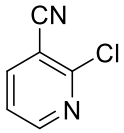 2-chloro-3-cyanopyridine	-41	n/d	n/d	n/d

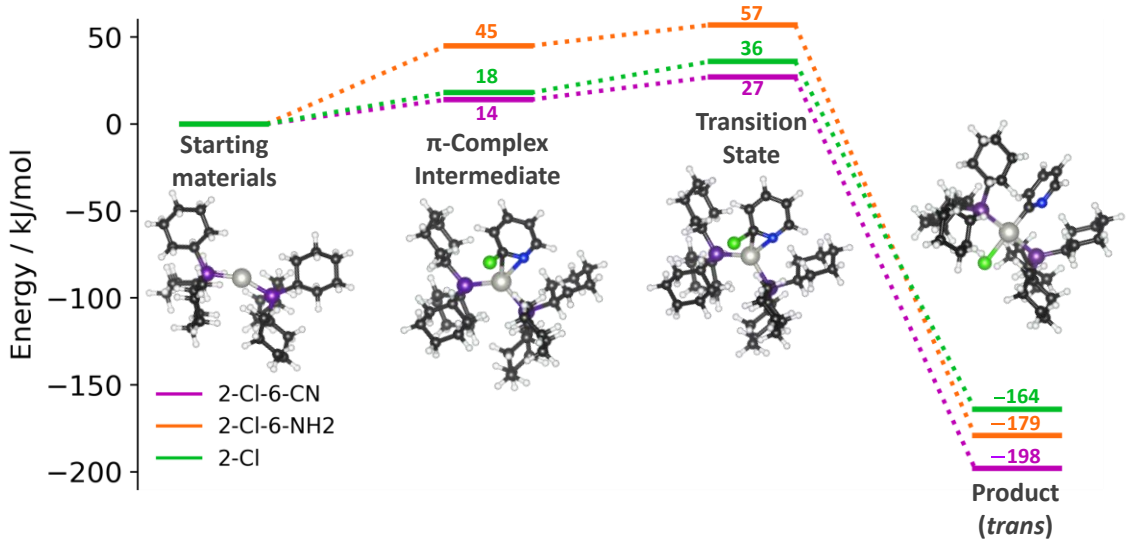

Fig. S38.
Simplified calculated reaction coordinate for oxidative addition of 2-chloro-6-cyanopyridine, 2-chloro-6-aminopyridine, and 2-chloropyridine to $Pd(PCy_3)_2$. Calculated structures for the 2-chloropyridine derivatives are shown as representative. The *cis* oxidative addition product is not shown.

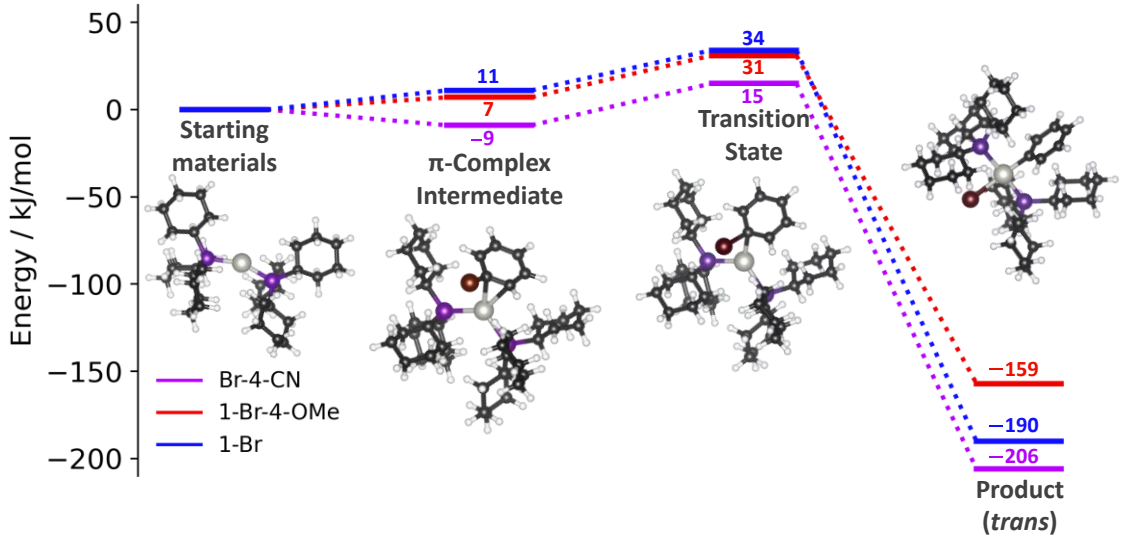

Fig. S39.
Simplified calculated reaction coordinate for oxidative addition of 4-bromobenzonitrile, 4-bromoanisole, and bromobenzene to $Pd(PCy_3)_2$. Calculated structures for the bromobenzene derivatives are shown as representative. The *cis* oxidative addition product is not shown.

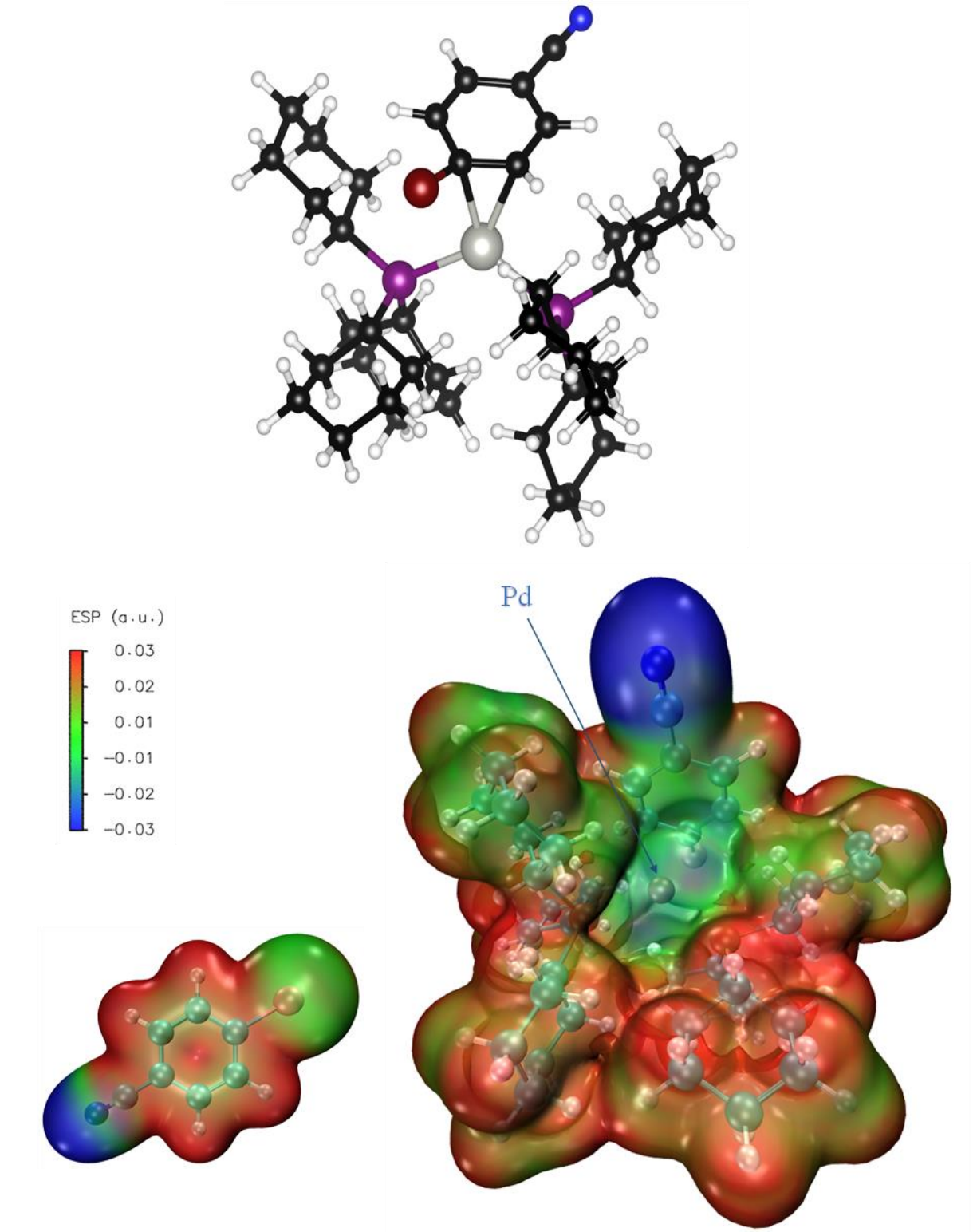

Fig. S40.
Calculated structure of the π-complex intermediate for 4-bromobenzonitrile, and *ESP* maps of the free substrate and the π-complex intermediate. ESP_{Pd} = 12.4 kJ/mol

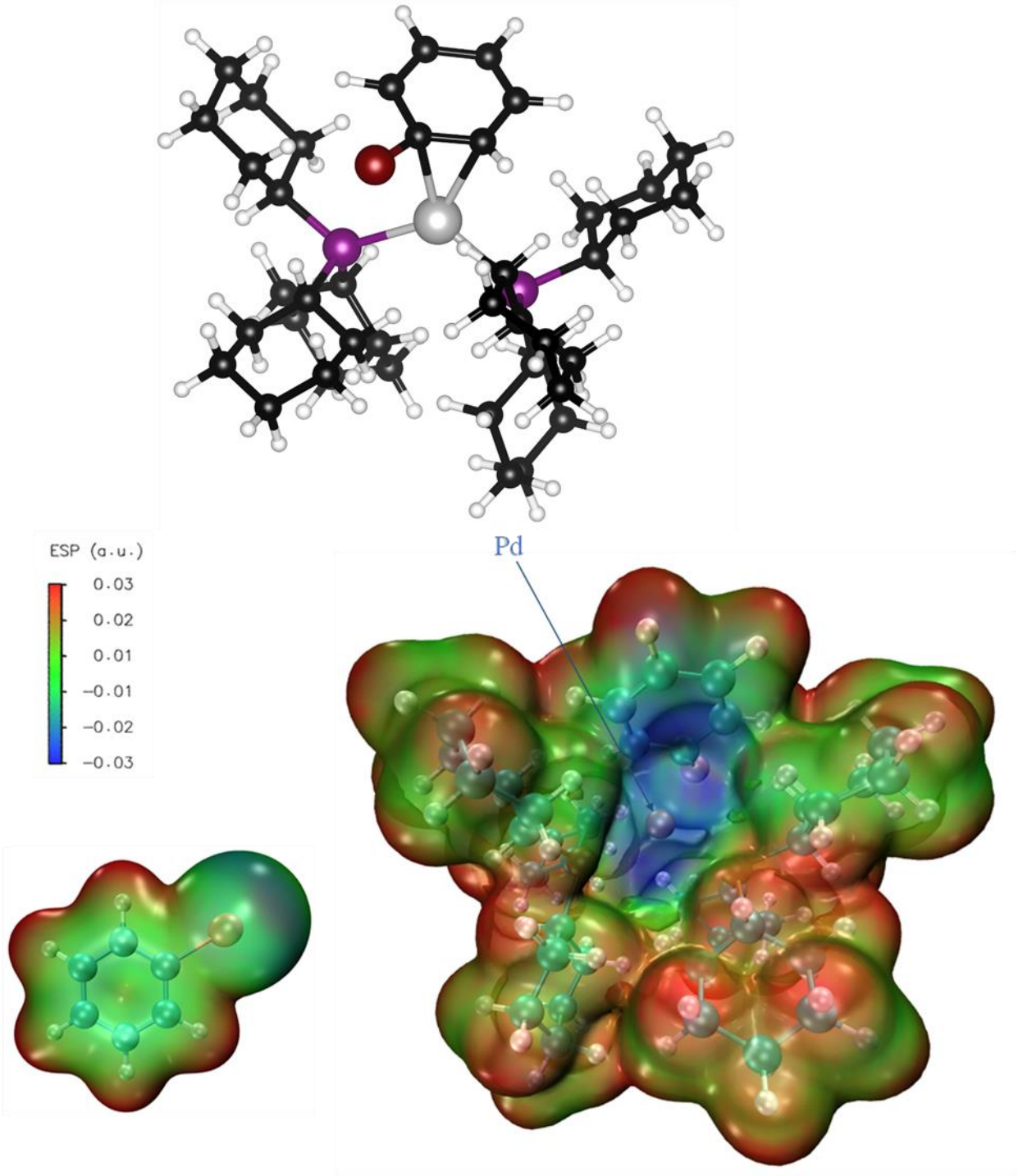

Fig. S41.
Calculated structure of the π-complex intermediate for bromobenzene, and *ESP* maps of the free substrate and the π-complex intermediate. ESP_{Pd} = -23.2 kJ/mol

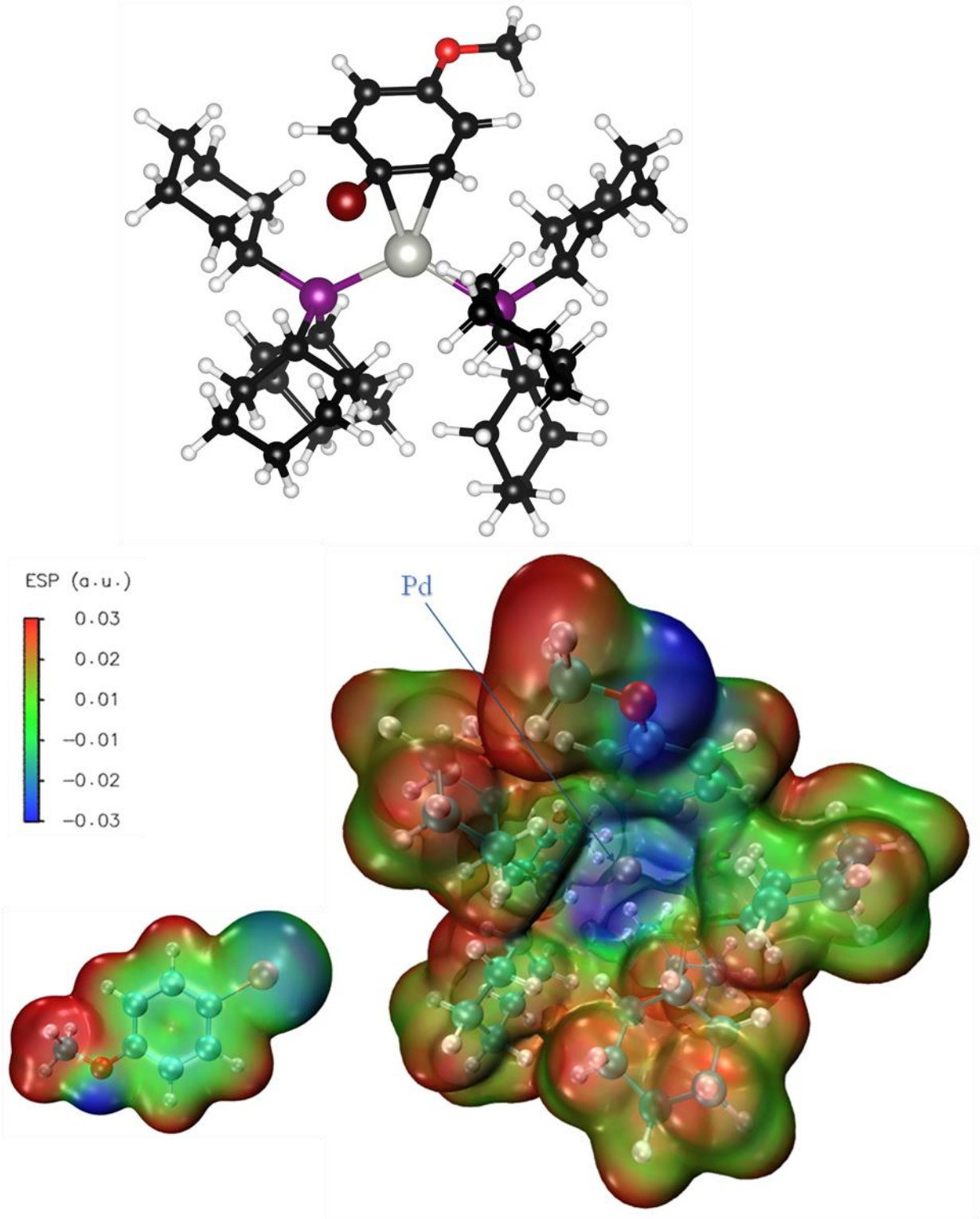

Fig. S42.
Calculated structure of the π-complex intermediate for 4-bromoanisole, and *ESP* maps of the free substrate and the π-complex intermediate. ESP_{Pd} = -27.2 kJ/mol

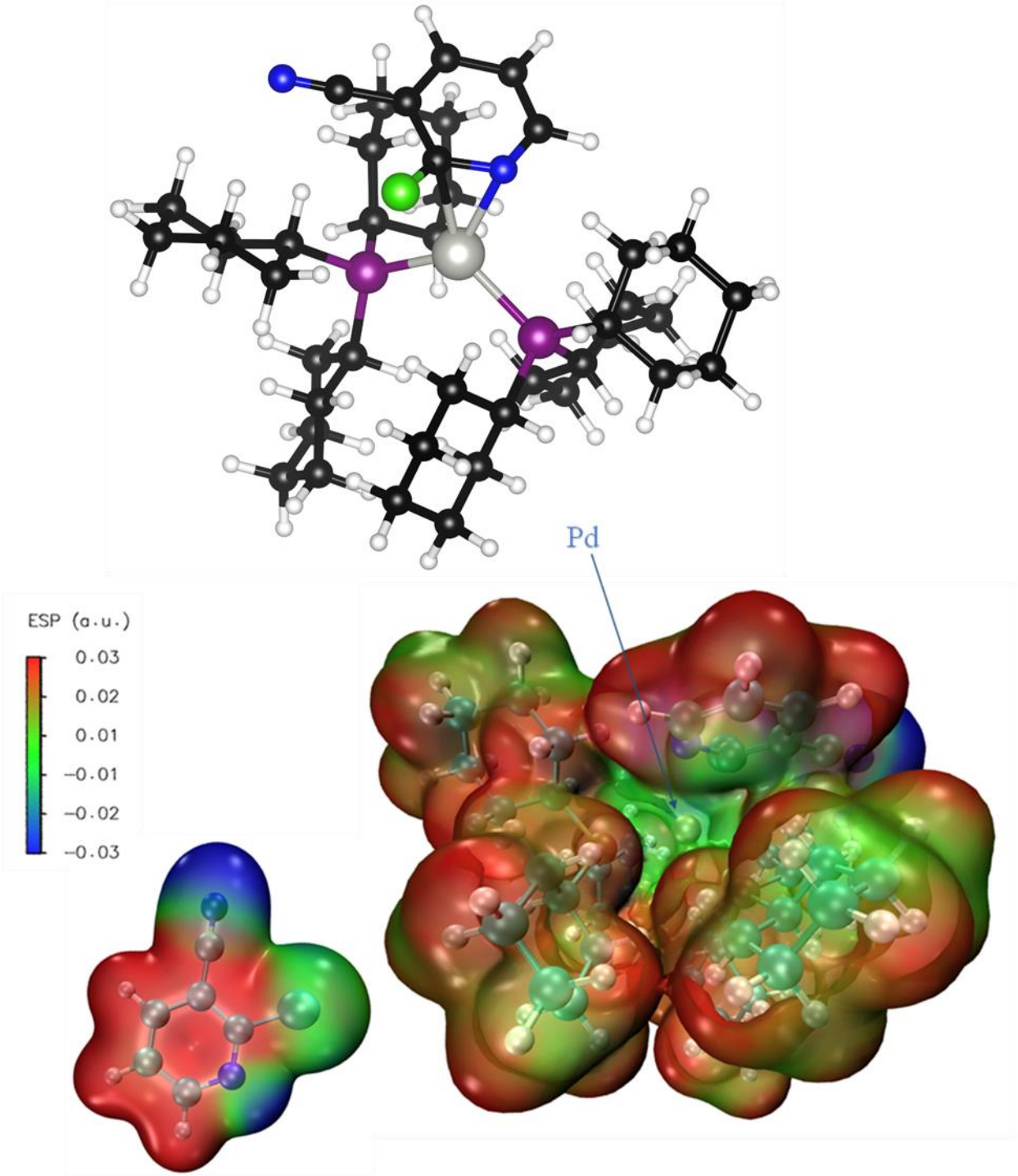

Fig. S43.
Calculated structure of the π-complex intermediate for 2-chloro-3-cyanopyridine, and *ESP* maps of the free substrate and the π-complex intermediate. ESP_{Pd} = 26.1 kJ/mol

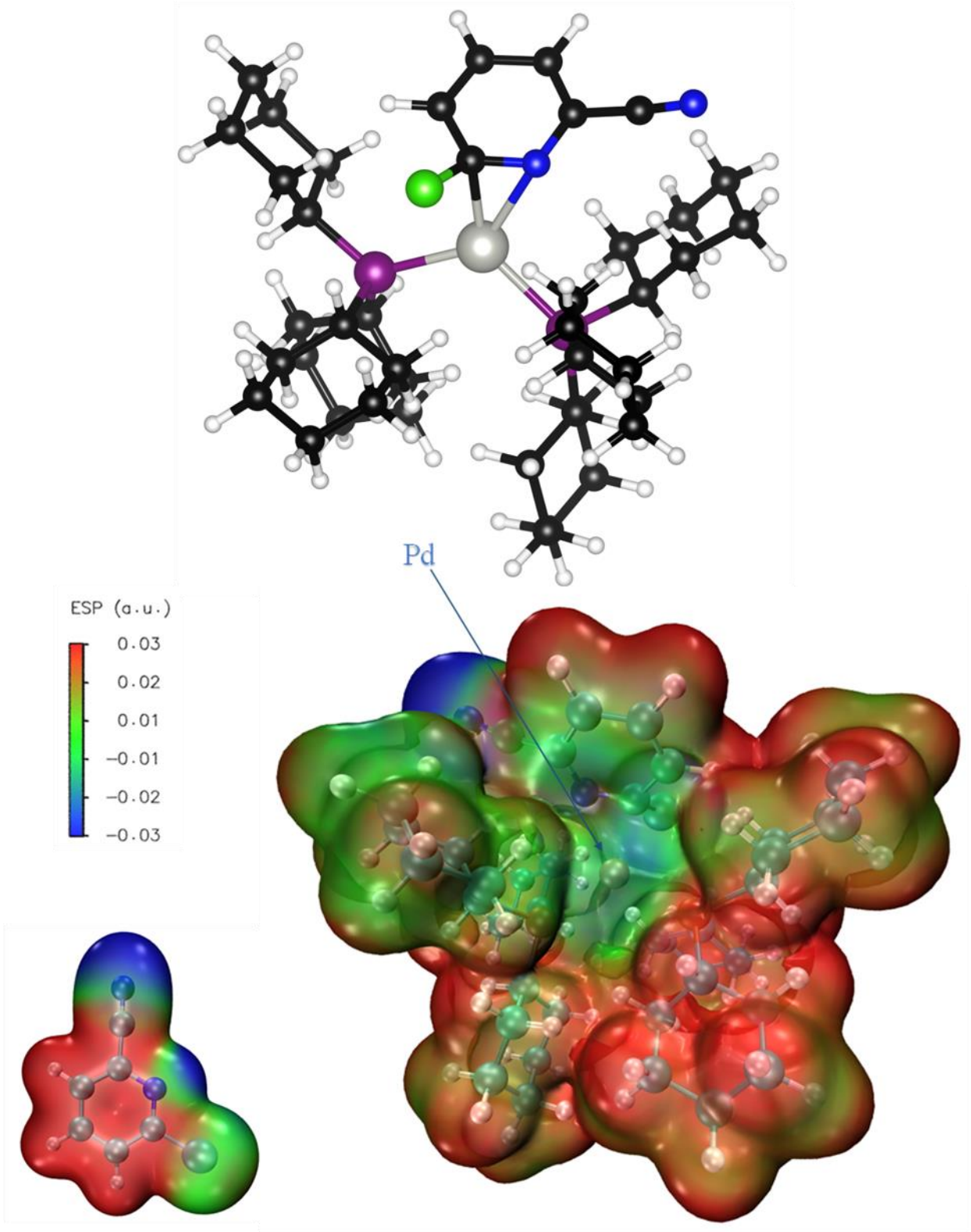

Fig. S44.
Calculated structure of the π-complex intermediate for 2-chloro-6-cyanopyridine, and *ESP* maps of the free substrate and the π-complex intermediate. ESP_{Pd} = 25.3 kJ/mol

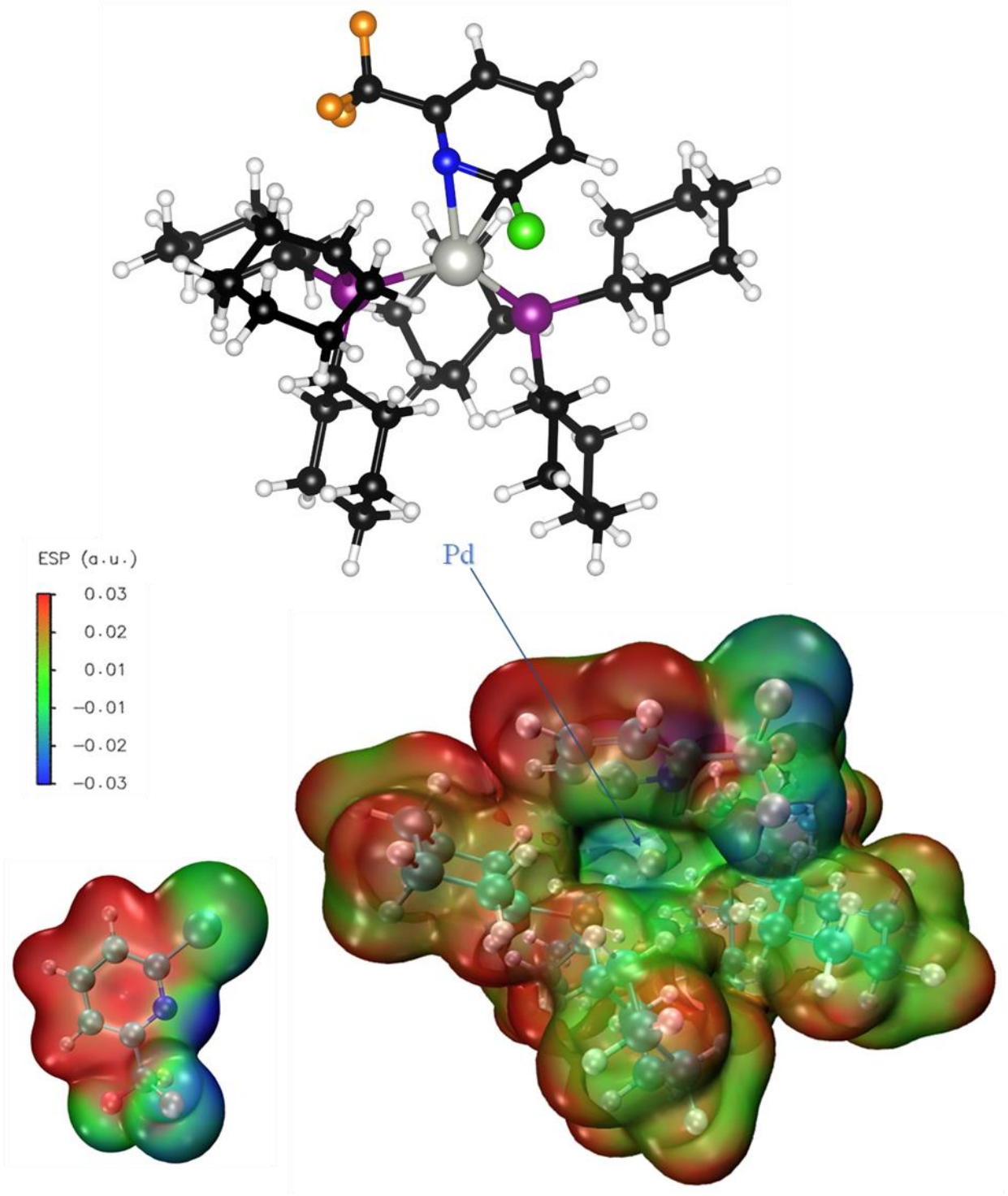

Fig. S45.
Calculated structure of the π-complex intermediate for 2-chloro-6-trifluoromethylpyridine, and *ESP* maps of the free substrate and the π-complex intermediate. ESP_{Pd} = 1.7 kJ/mol

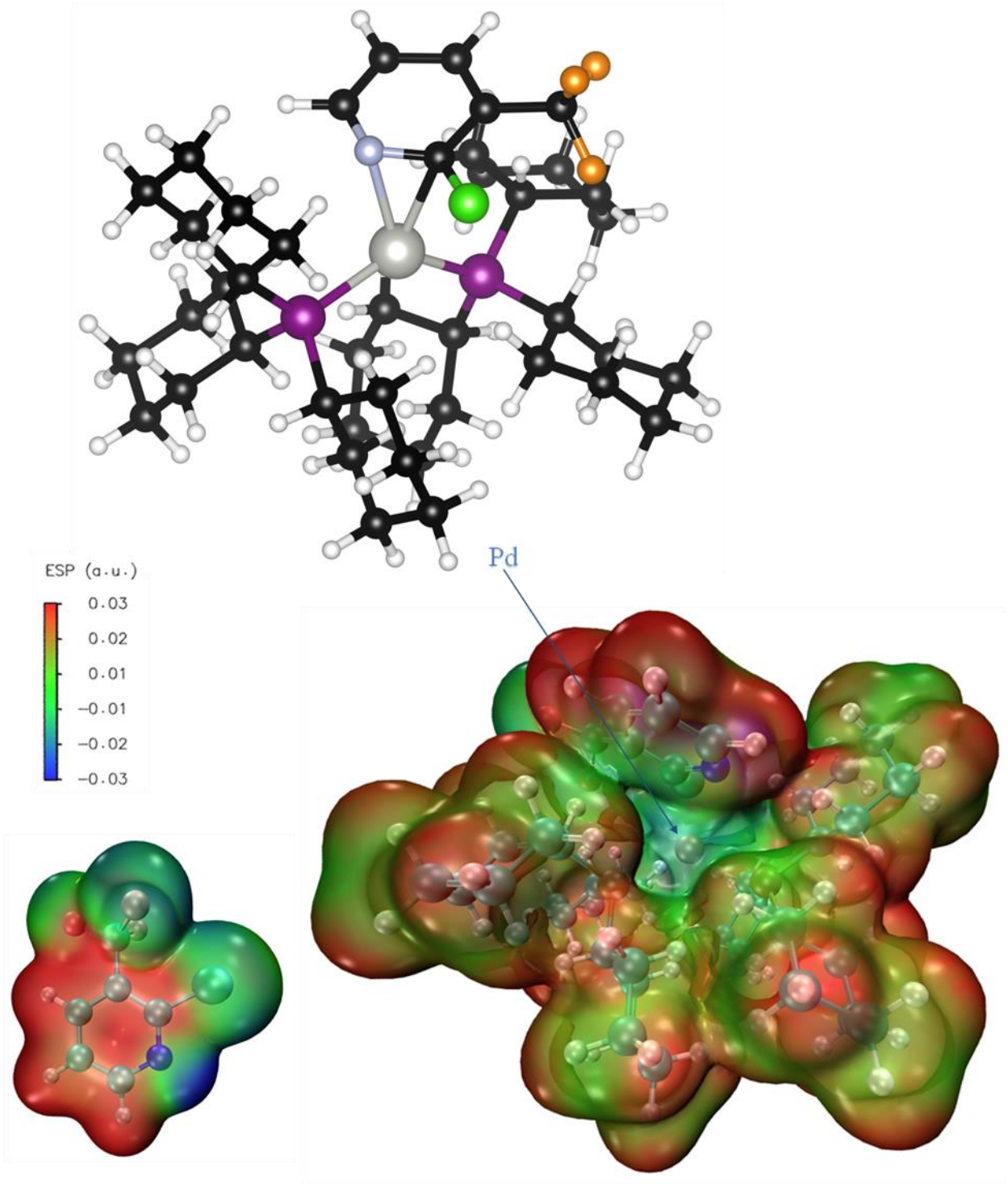

Fig. S46.
Calculated structure of the π-complex intermediate for 2-chloro-3-trifluoromethylpyridine, and *ESP* maps of the free substrate and the π-complex intermediate. ESP_{Pd} = -3.6 kJ/mol

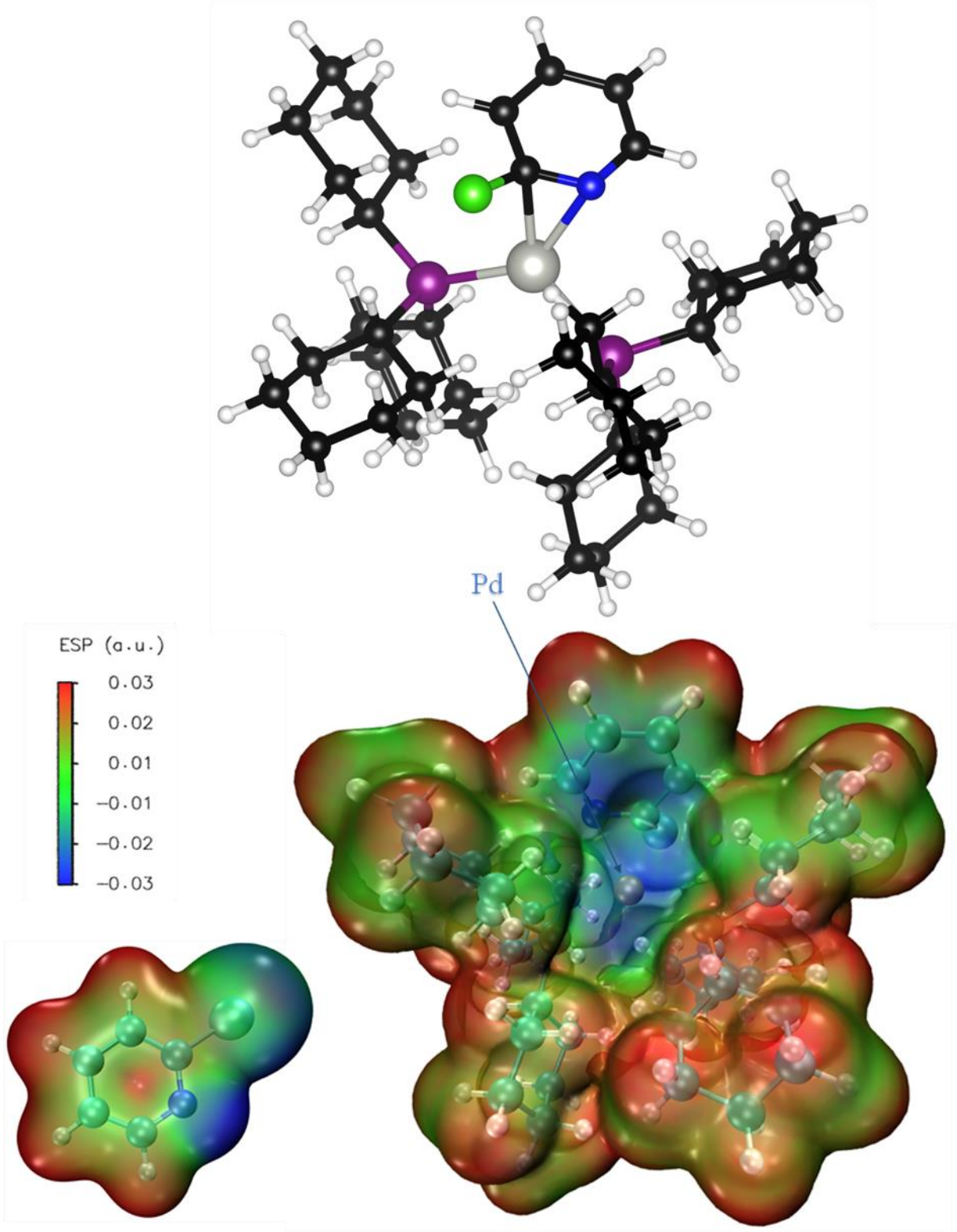

Fig. S47.
Calculated structure of the π-complex intermediate for 2-chloropyridine, and *ESP* maps of the free substrate and the π-complex intermediate. ESP_{Pd} = -11.7 kJ/mol

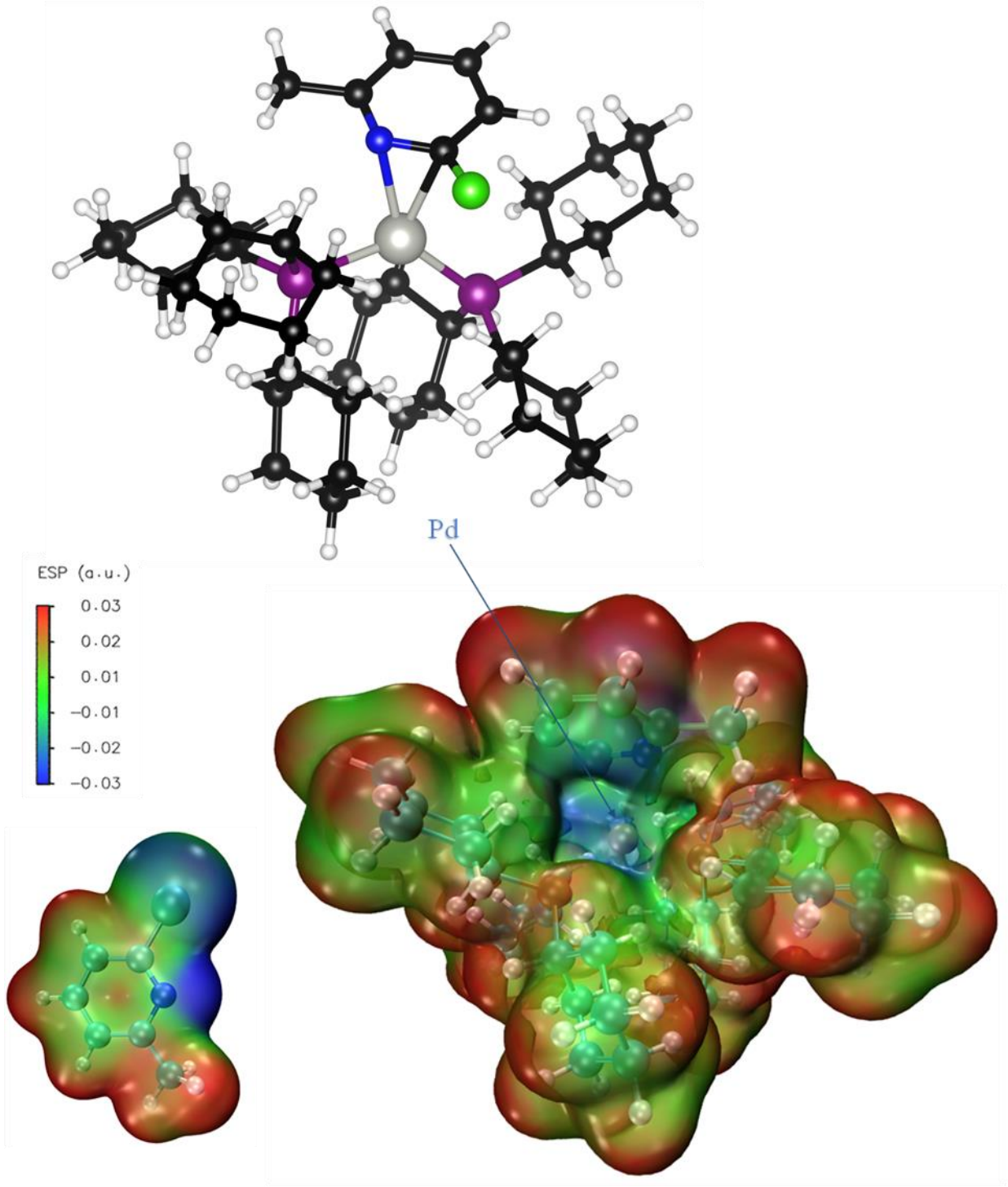

Fig. S48.
Calculated structure of the π-complex intermediate for 2-chloro-6-methylpyridine, and *ESP* maps of the free substrate and the π-complex intermediate. ESP_{Pd} = -11.3 kJ/mol

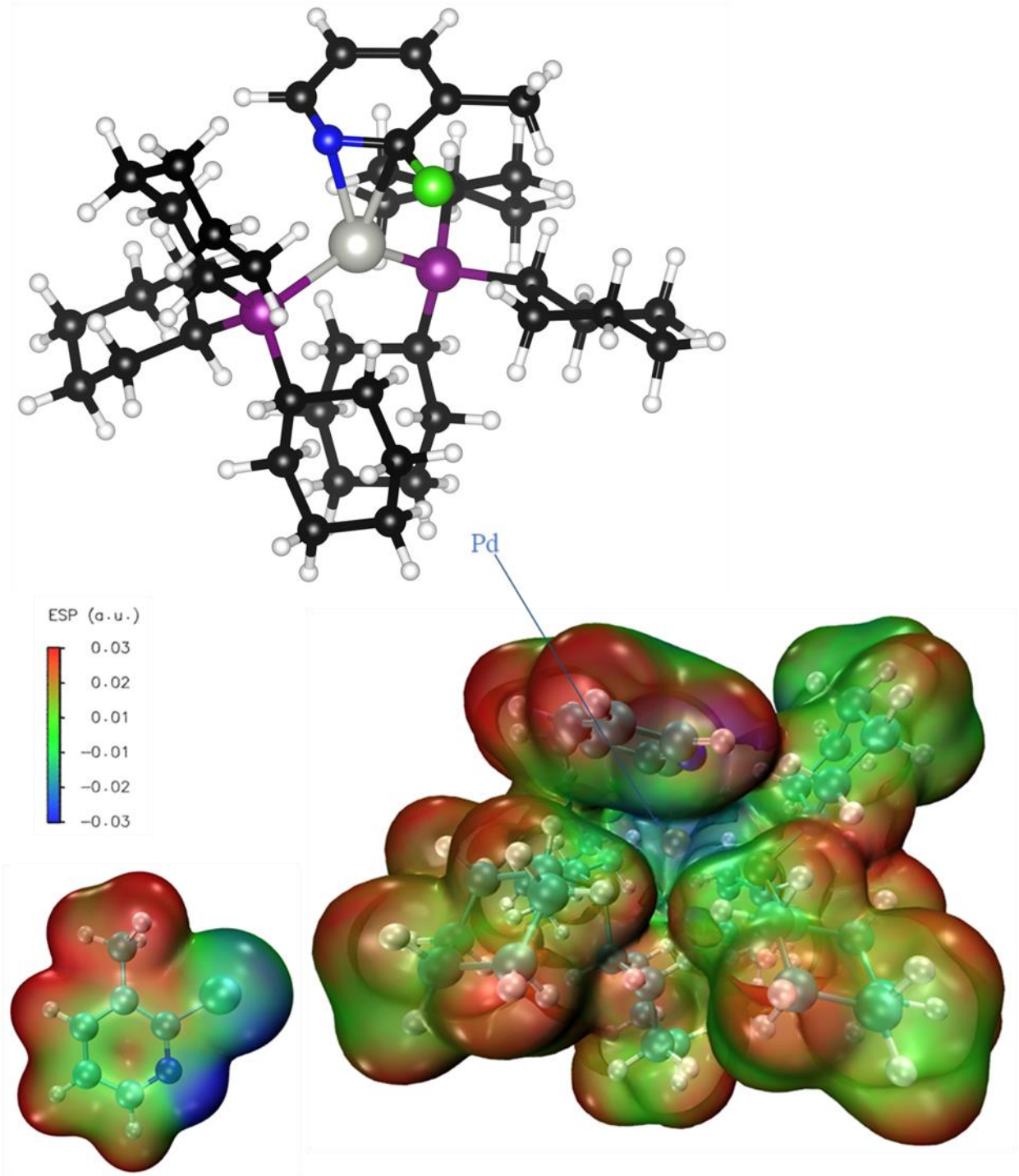

Fig. S49.
Calculated structure of the π-complex intermediate for 2-chloro-3-methylpyridine, and *ESP* maps of the free substrate and the π-complex intermediate. ESP_{Pd} = -9.7 kJ/mol

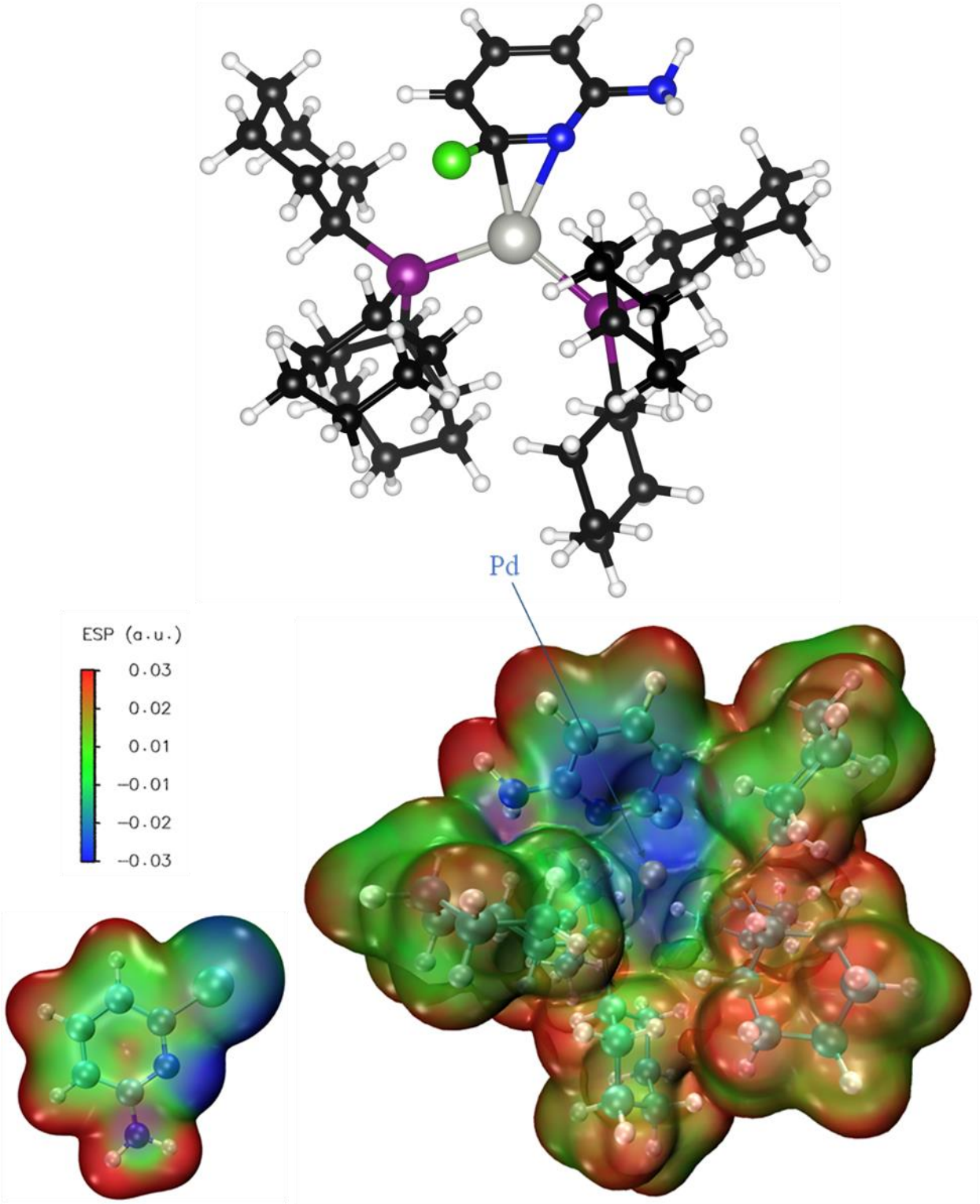

Fig. S50.
Calculated structure of the π-complex intermediate for 2-chloro-6-aminopyridine, and *ESP* maps of the free substrate and the π-complex intermediate. ESP_{Pd} = -15.0 kJ/mol

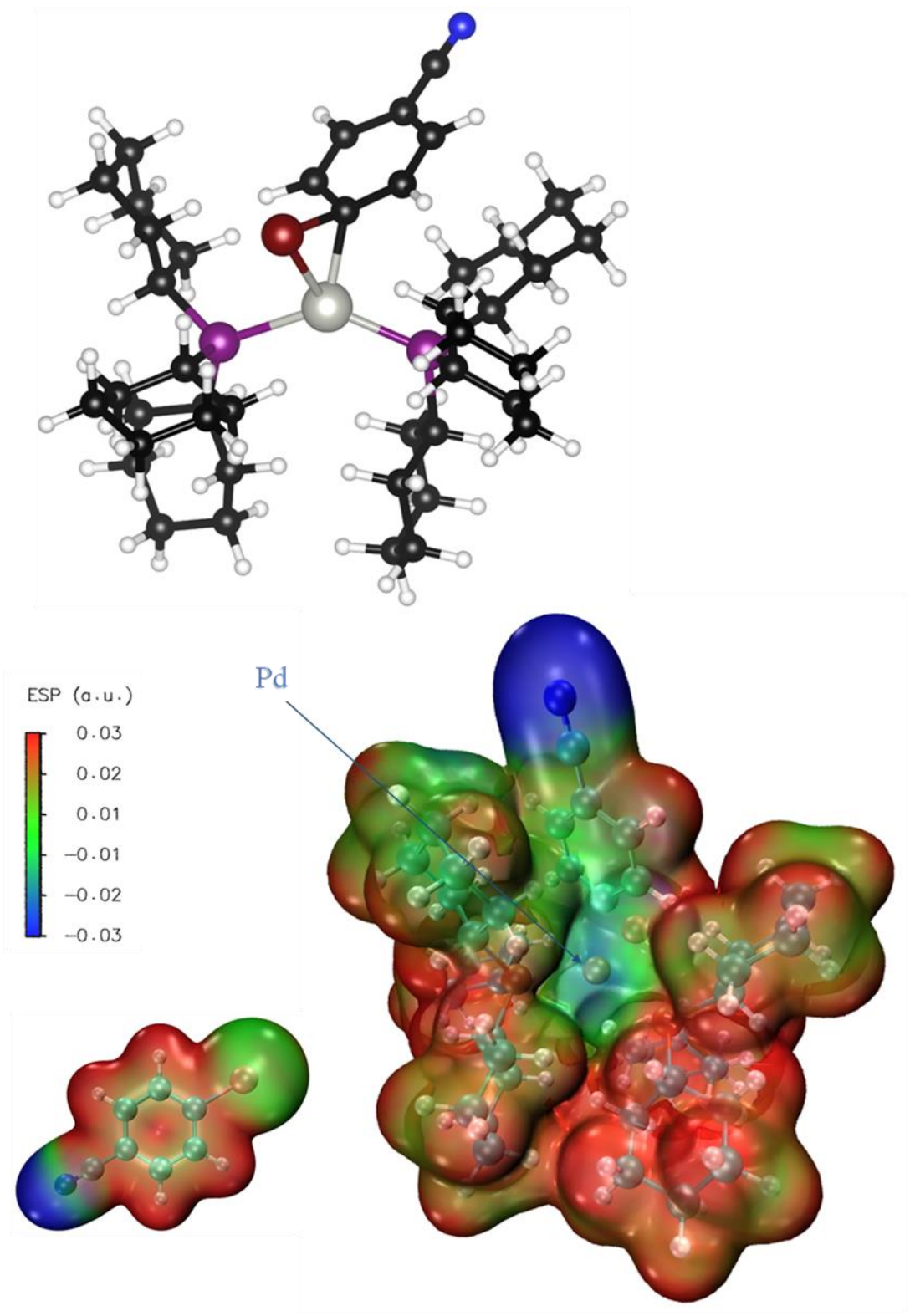

Fig. S51.
Calculated structure of the oxidative addition transition state for 4-bromobenzonitrile, and *ESP* maps of the free substrate and the transition state. ESP_{Pd} = 22.9 kJ/mol

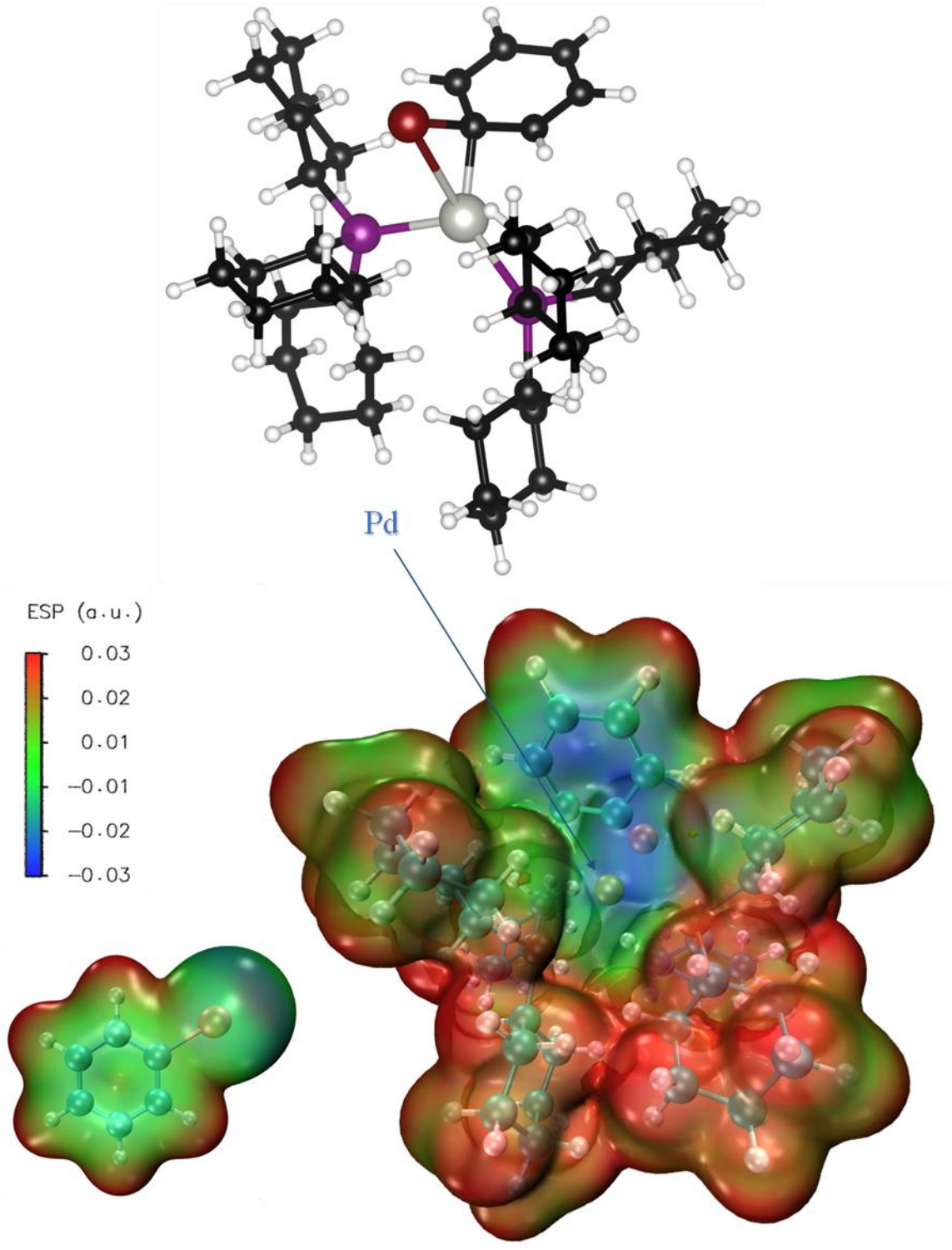

Fig. S52.
Calculated structure of the oxidative addition transition state for bromobenzene, and *ESP* maps of the free substrate and the transition state. ESP_{Pd} = 13.5 kJ/mol

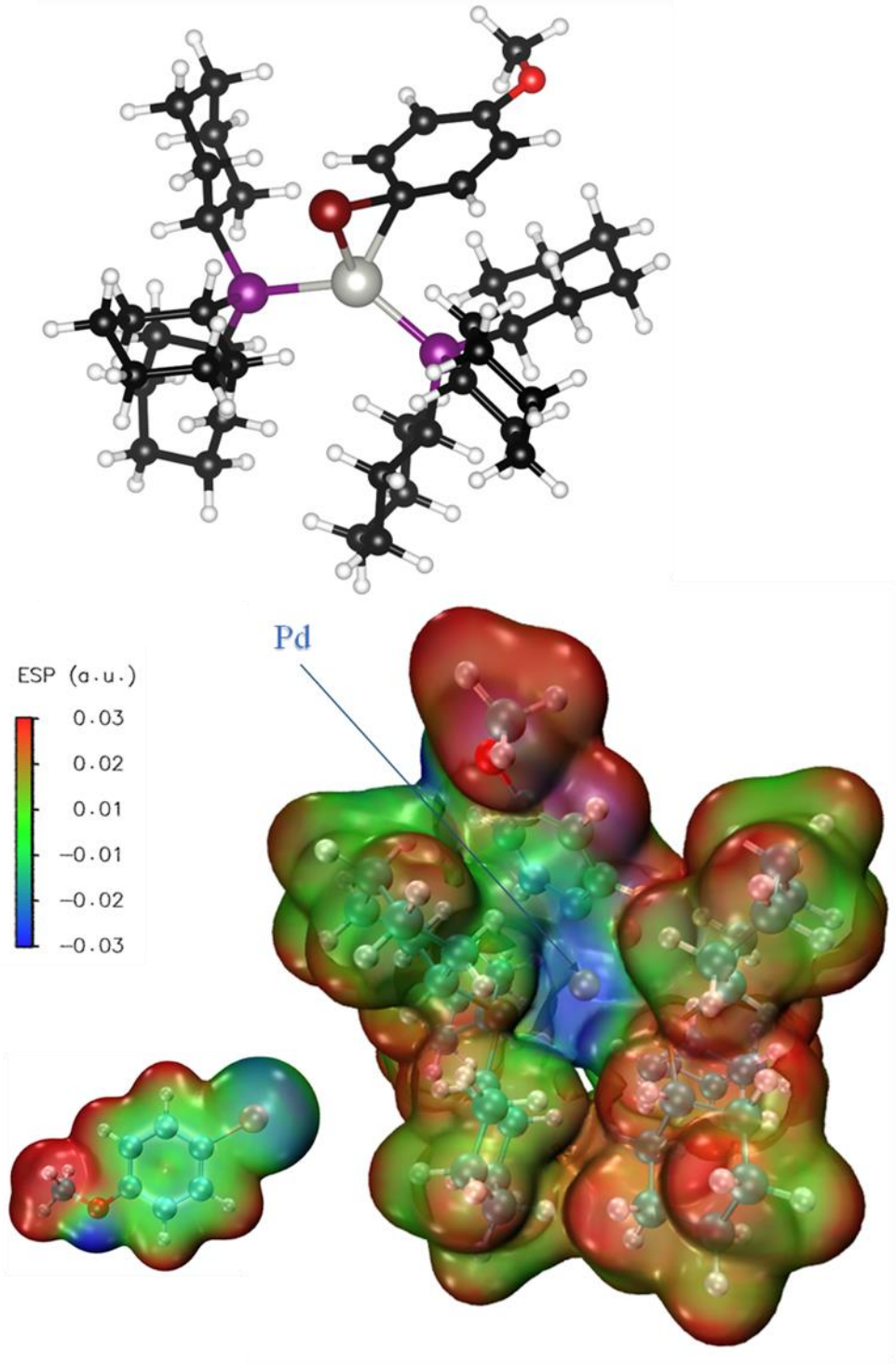

Fig. S53.
Calculated structure of the oxidative addition transition state for 4-bromoanisole, and *ESP* maps of the free substrate and the transition state. ESP_{Pd} = -29.8 kJ/mol

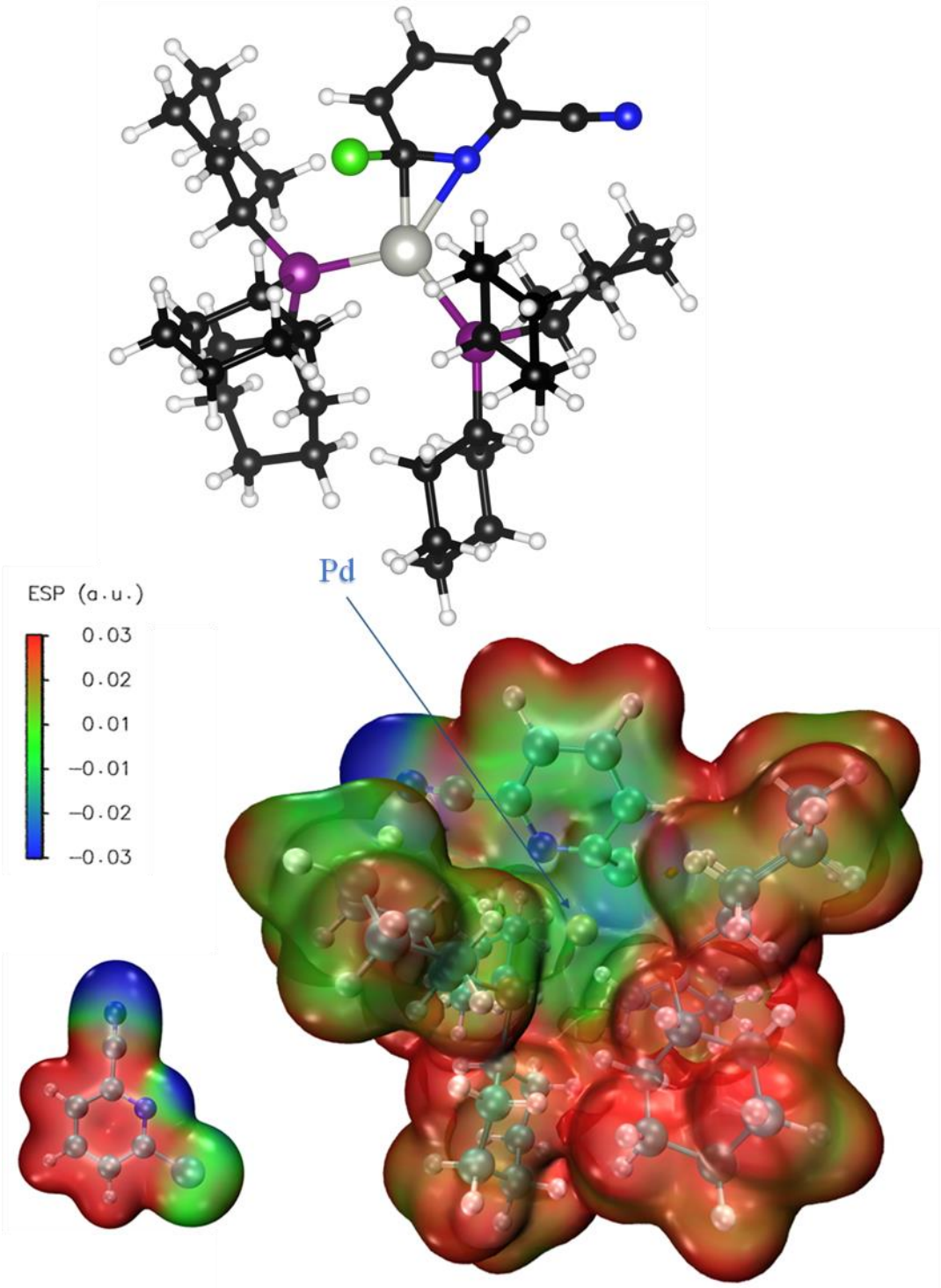

Fig. S54.
Calculated structure of the oxidative addition transition state for 2-chloro-6-cyanopyridine, and *ESP* maps of the free substrate and the transition state. ESP_{Pd} = 42.2 kJ/mol

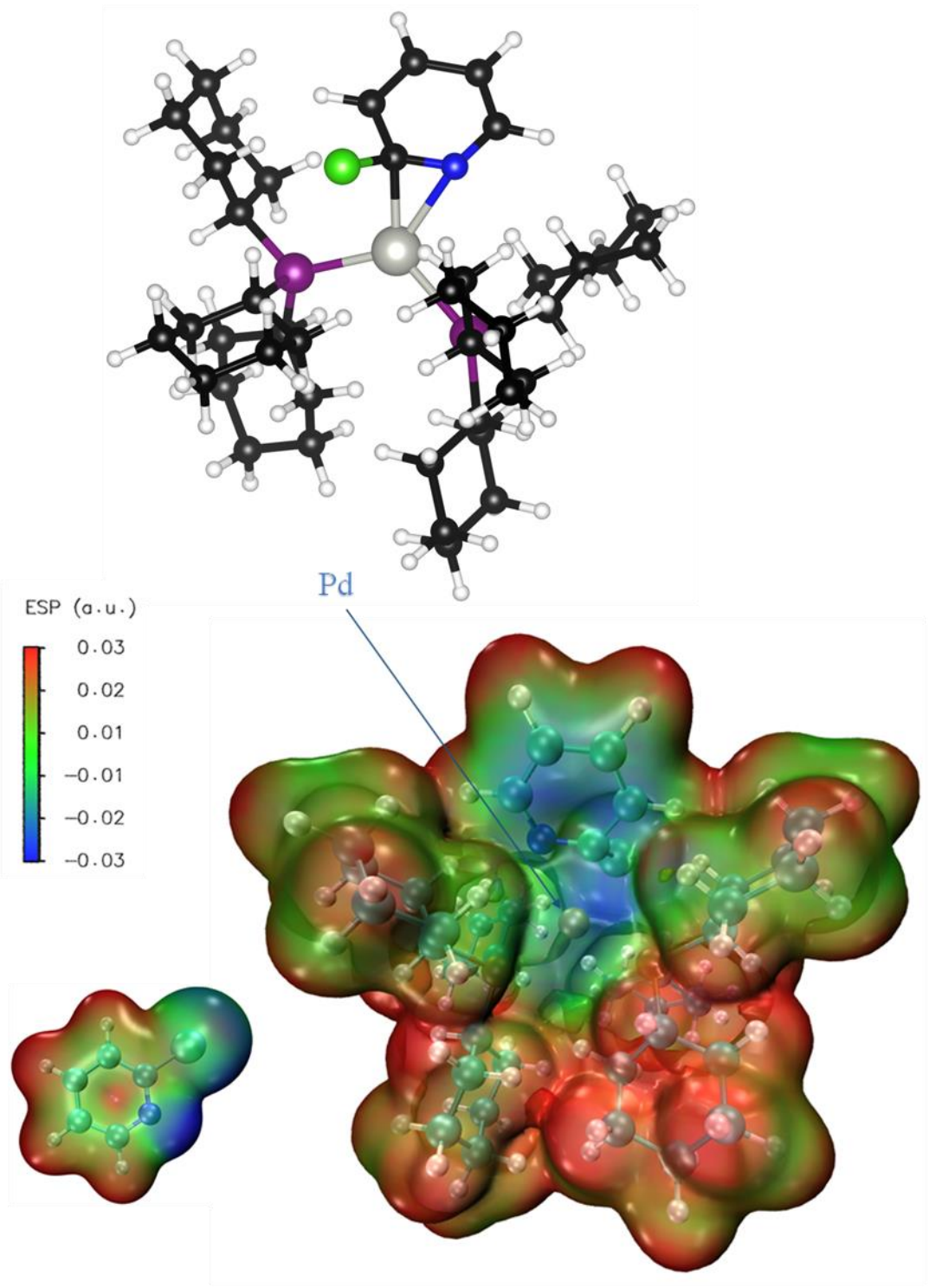

Fig. S55.
Calculated structure of the oxidative addition transition state for 2-chloropyridine, and *ESP* maps of the free substrate and the transition state. ESP_{Pd} = 7.7 kJ/mol

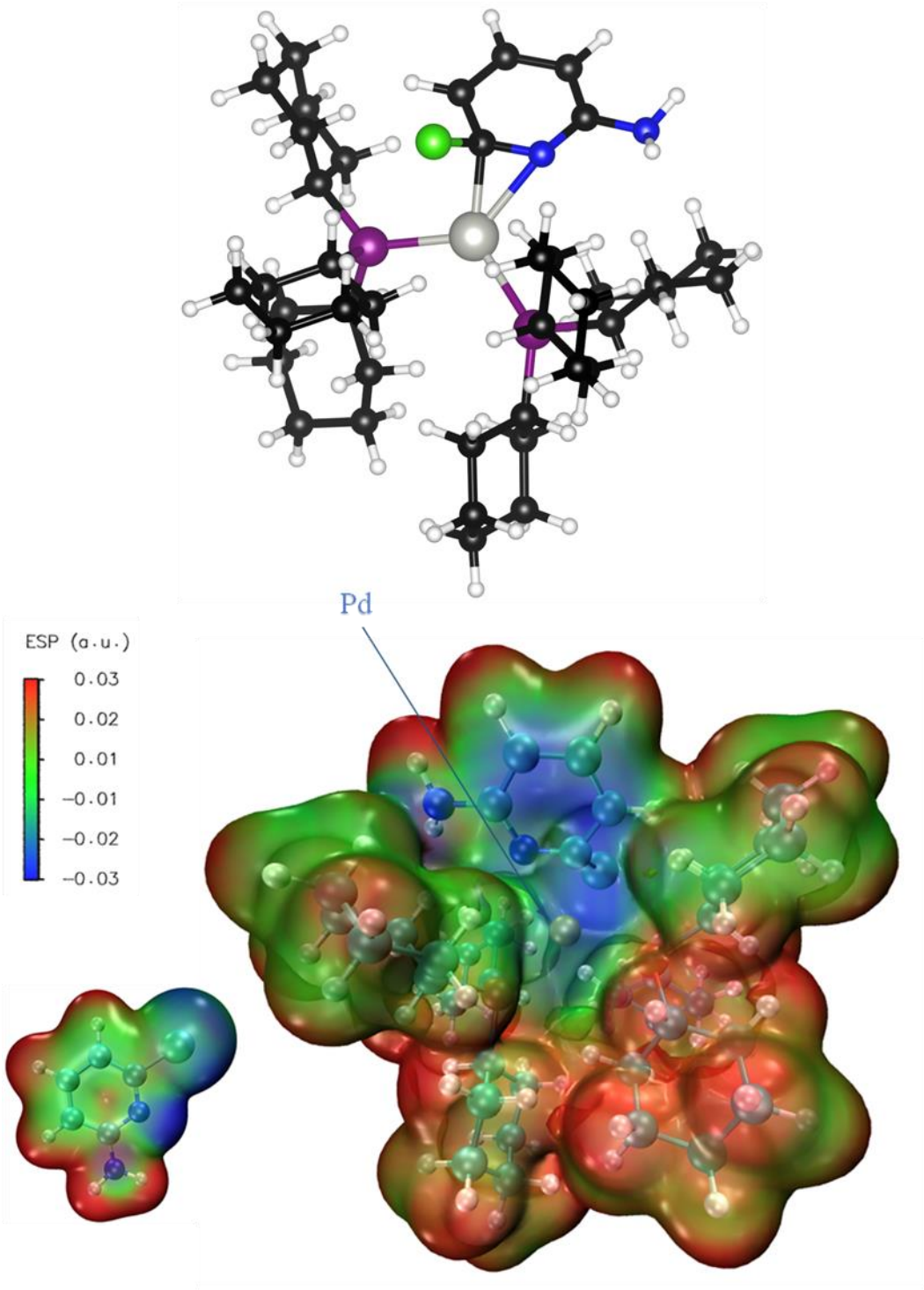

Fig. S56.
Calculated structure of the oxidative addition transition state for 2-chloro-6-aminopyridine, and *ESP* maps of the free substrate and the transition state. ESP_{Pd} = 5.8 kJ/mol

Analyzing how ESP_{Pd} relates to experimental $\Delta G^{\ddagger}_{OA}$ revealed the linear correlation from Fig. 3A. A fully labelled version of this chart is shown in Fig. S57.

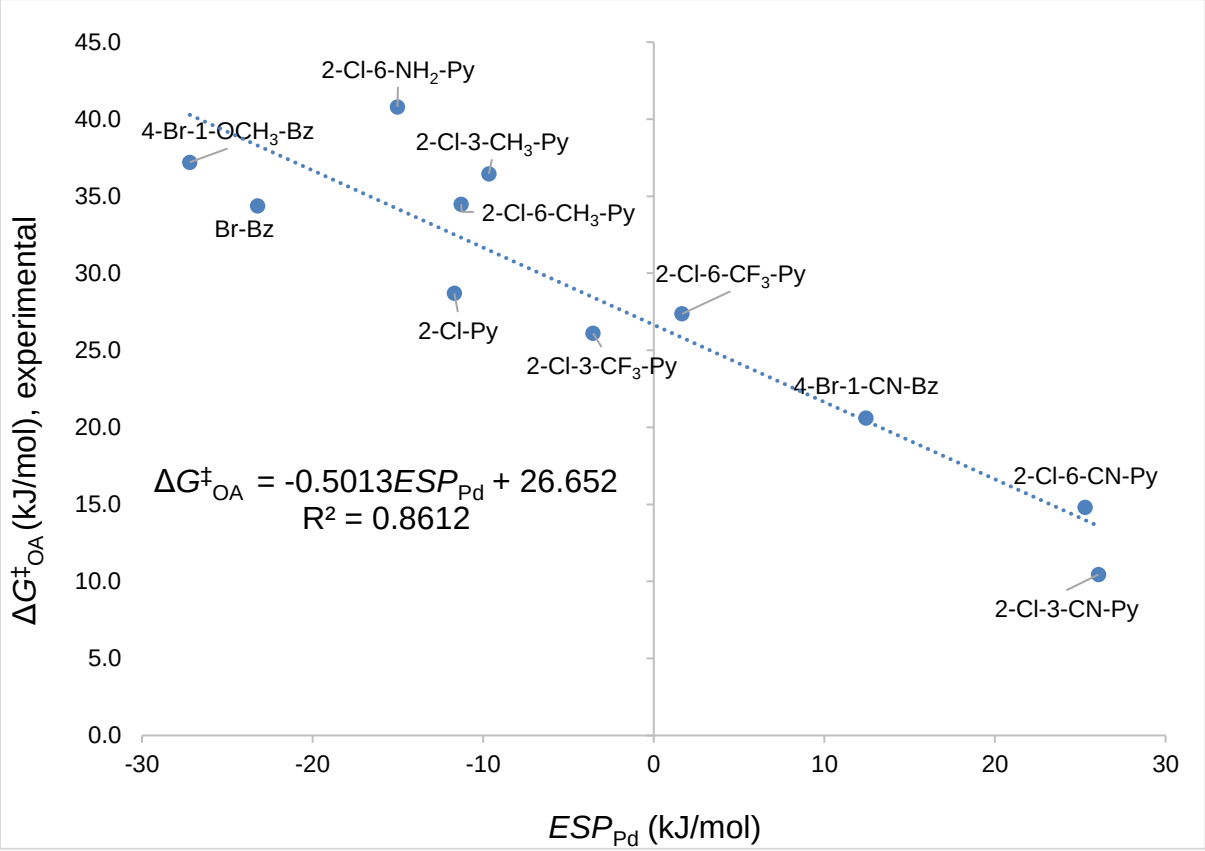

Fig. S57.
Linear correlation between observed $\Delta G^{\ddagger}_{OA}$ and ESP_{Pd} for 11 π-complex intermediates with the indicated substrates bound to Pd.

Construction of the Multivariate Linear Regression Model

The selection of the molecular descriptors used to correlate $\Delta G^{\ddagger}_{OA}$ with substrate structure was guided by the mechanistic features of oxidative addition elucidated previously, computational calculations on the π-complex intermediates and transition states, and iterative refinement of the included descriptors based on our experimental observations. As summarized in Fig. S58, there are four descriptors that lead to accurate predictions of relative oxidative addition reactivity: average molecular electrostatic potential (ESP_1) at the reactive carbon, average molecular electrostatic potential (ESP_2) at the adjacent atom to the reactive center, sum of the A-values for substituents R_1 and R_2, and the intrinsic bond strength index (*IBSI*) of the C–X (X = Cl, Br, O) bond. To make interpretation of the model easier, we multiplied the unitless *IBSI* values (~0.23-0.40) by 1000 to give values with a similar order of magnitude to bond dissociation energies (~300-450 kJ mol^{-1}). In this way, the coefficients in the multivariate linear equation more accurately represent the relative contribution of each term to the overall $\Delta G^{\ddagger}_{OA}$.

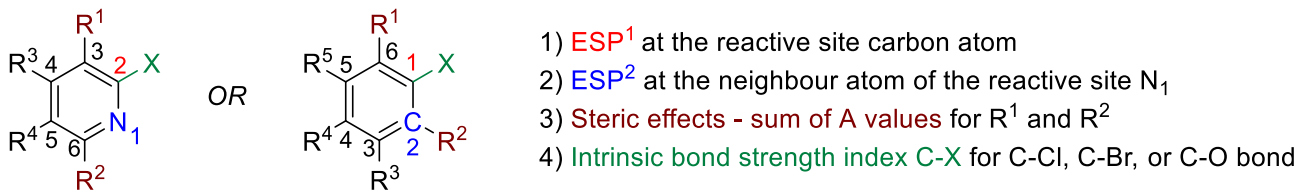

Fig. S58.
Substrate molecular descriptors to construct the oxidative addition prediction model.

The initial multivariate linear regression model constructed from these descriptors and the $\Delta G^{\ddagger}_{OA}$ of 70 (hetero)aryl halides in THF achieved excellent linear correlation with a squared correlation coefficient (R^2) of 0.92, and a mean absolute error (MAE) of 2.50 kJ/mol, and has an expected random distribution of residuals and no significant outliers as summarized in Figure S59.

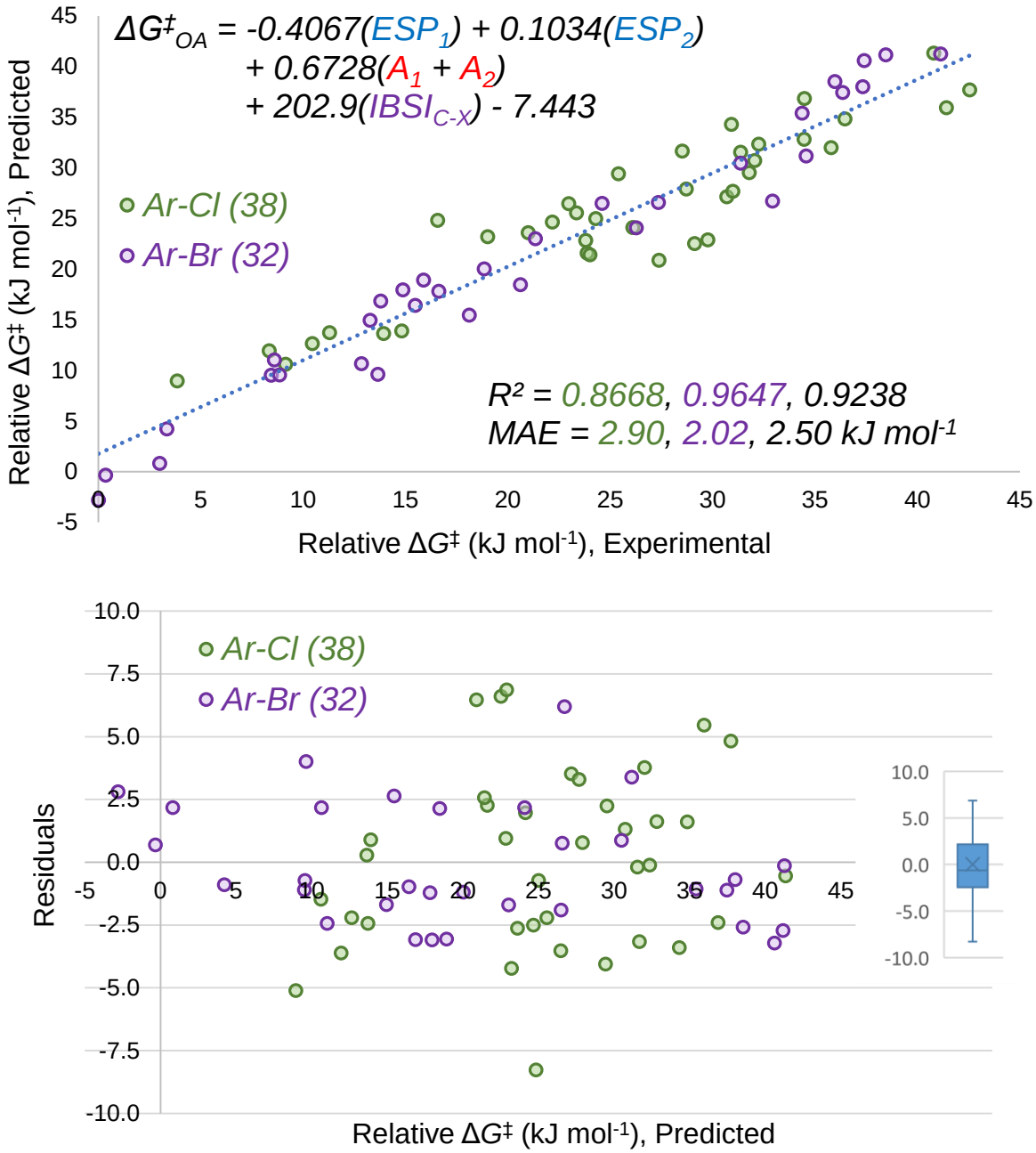

Fig. S59.
Multivariate linear regression model of $\Delta G^{\ddagger}_{OA}$ for 70 substrates, including experimental versus predicted plot (top) and predicted versus residuals plot with corresponding box plot inset (bottom).

To validate the inclusion of these descriptors and evaluate simpler potential models, we have compared the four-descriptor model to a series of alternatives (Table S8).

First, as stated in the main text and above, we discovered that the two steric A-values have approximately equal contributions when linear regression fitting is done with A_1 and A_2 as separate descriptors. This alternate, five descriptor model is shown in entry 2. An R^2 of 0.92 and a MAE of 2.46 kJ/mol were obtained from the five-variable linear regression model, which are almost

identical to those obtained from the original four-variable regression model (entry 1). The two models give the same level of prediction accuracy, and thus the steric A-values of R_1 and R_2 are treated as one summed value for simplification.

The inclusion of ESP_2 (corresponding to the adjacent atom) in the model was explored based on the nature of the S_NAr oxidative addition mechanism transition state, and the Hammett analysis on the 4-Z-2-chloropyridines (Figs. S35-S36). To confirm that both ESP_1 and ESP_2 are necessary to predict $\Delta G^{\ddagger}_{OA}$, a linear regression model was constructed with only 3 descriptors (ESP_1, A_1+A_2, *IBSI*). This model, shown in entry 3, gives poorer performance, with one 60/40 training/test split giving a Q^2 of 0.83 and a MAE of 3.91 kJ/mol for the test data.

The inclusion of the *IBSI* descriptor is necessary to create a single model that incorporates both Ar–Cl and Ar–Br substrates. Linear regression models that do not include this descriptor (entries 4-6) perform poorly with respect to linear correlation and predictive ability, with test set MAE values of 4.44-4.97 kJ/mol.

Finally, we evaluated a model that does not include steric effects (entry 7). While the descriptive statistics of this model appear to be fairly good, this is because many of the substrates in our library do not include substituents at R_1 or R_2. The all-data plot in entry 7 shows that many of the substrates with non-zero A_1+A_2 values (dark orange points) are significant systematic outliers, where the model underestimates $\Delta G^{\ddagger}_{OA}$.

Overall, the alternatives presented in Table S8 demonstrate that all of the four descriptors are necessary and sufficient to predict $\Delta G^{\ddagger}_{OA}$ for this diverse set of substrates.

Table S8.

Comparison of model performance for different combinations of molecular descriptors.

Comparison of Model Performance				
Variables	**Multivariate linear regression model performance**		**60/40 random split performance for test set**	
	R^2	MAE (KJ/mol)	Q^2	MAE (KJ/mol)
ESP_1, ESP_2, IBSI, A_1+A_2	0.92	2.50	0.91	2.77
	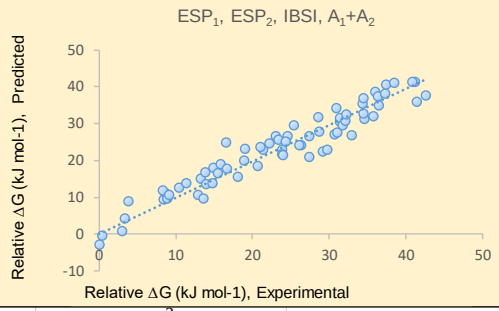		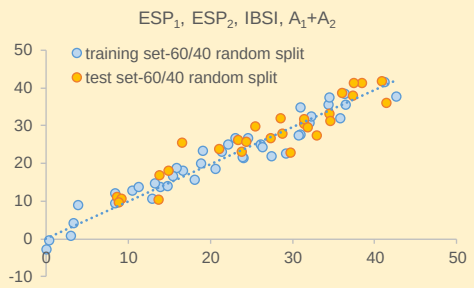	
ESP_1, ESP_2 IBSI, A_1, A_2	R^2	MAE (KJ/mol)	Q^2	MAE (KJ/mol)
	0.92	2.46	0.9	2.9
	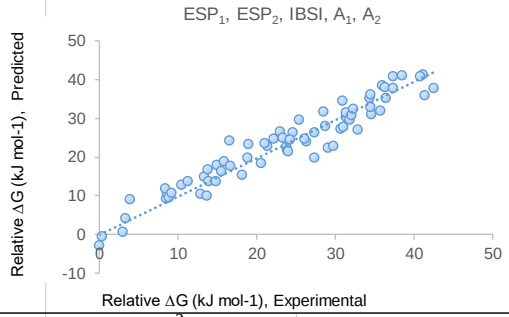		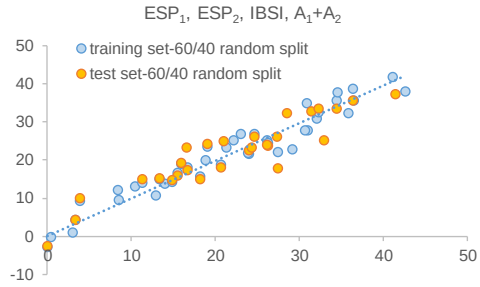	
ESP_1, IBSI, A_1+A_2	R^2	MAE (KJ/mol)	Q^2	MAE (KJ/mol)
	0.76	4.36	0.83	3.91
	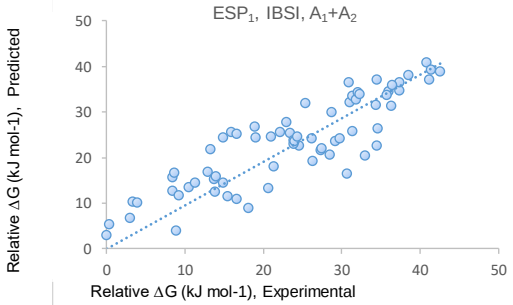		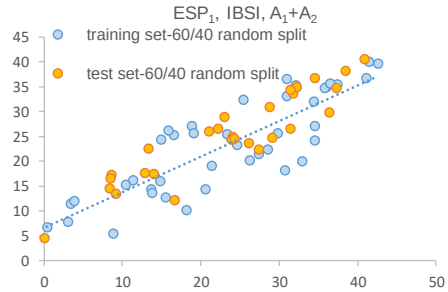	
ESP_1, ESP_2	R^2	MAE (KJ/mol)	Q^2	MAE (KJ/mol)
	0.60	5.40	0.71	4.97
	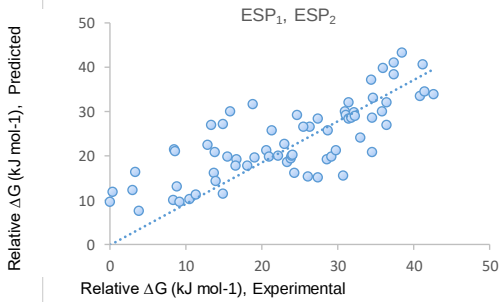		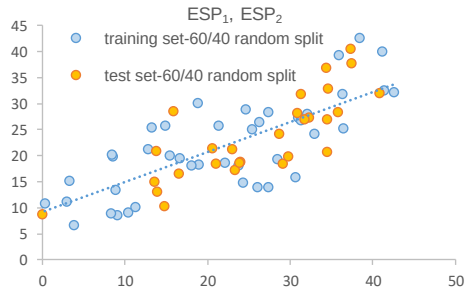	

	R^2	MAE (KJ/mol)	Q^2	MAE (KJ/mol)
ESP_1, ESP_2, A_1+A_2	0.65	5.15	0.67	4.55

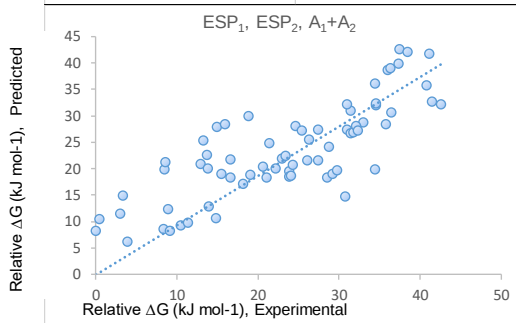

	R^2	MAE (KJ/mol)	Q^2	MAE (KJ/mol)
ESP_1	0.58	5.27	0.74	4.44

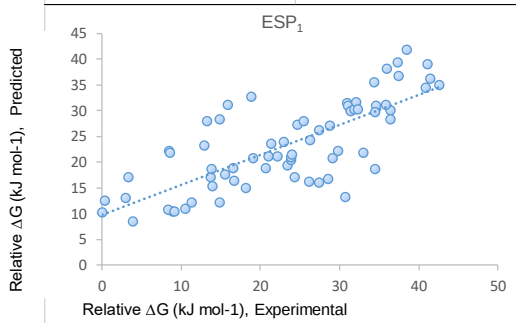

	R^2	MAE (KJ/mol)	Q^2	MAE (KJ/mol)
ESP_1, ESP_2, IBSI	0.89	2.86	0.85	3.28

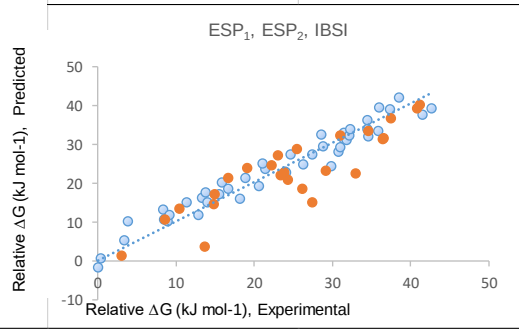

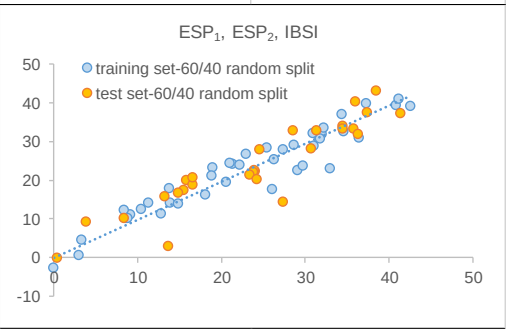

Cross Validation and Out-of-Sample Prediction

To further evaluate the linear regression model, we performed cross-validation by doing five random 60/40 training/test data splits. Excellent linear correlation was achieved between the observed and predicted $\Delta G^{\ddagger}_{OA}$, as indicated by the range of R^2 from 0.90 to 0.95 for training set, Q^2 from 0.88 to 0.91, and MAE from 2.63 kJ/mol to 3.00 kJ/mol for test set. A plot for one such 60/40 split is shown in Fig. 2D in the main text, and the plots for other four divisions are shown in Figures S60 to S63. The good agreement between the observed and predicted $\Delta G^{\ddagger}_{OA}$ obtained from this random split cross-validation has indicated that our multivariate linear regression model is appropriately fitted, without overfitting issues.

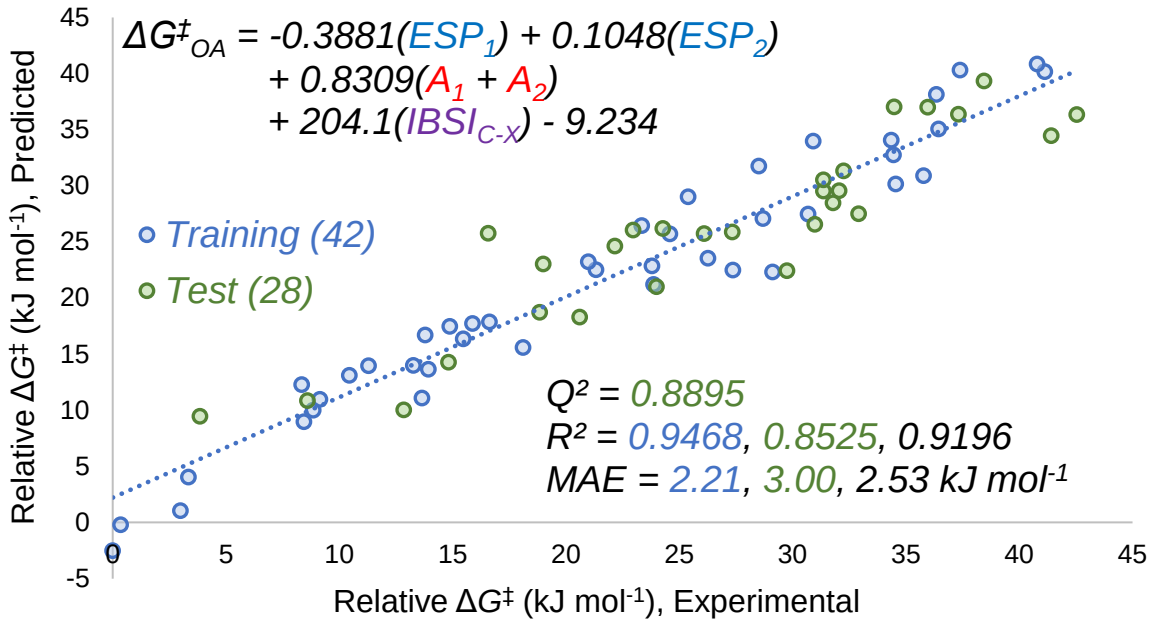

Fig. S60.
Multivariate linear regression model from one of the five 60/40 random split divisions (2/5).

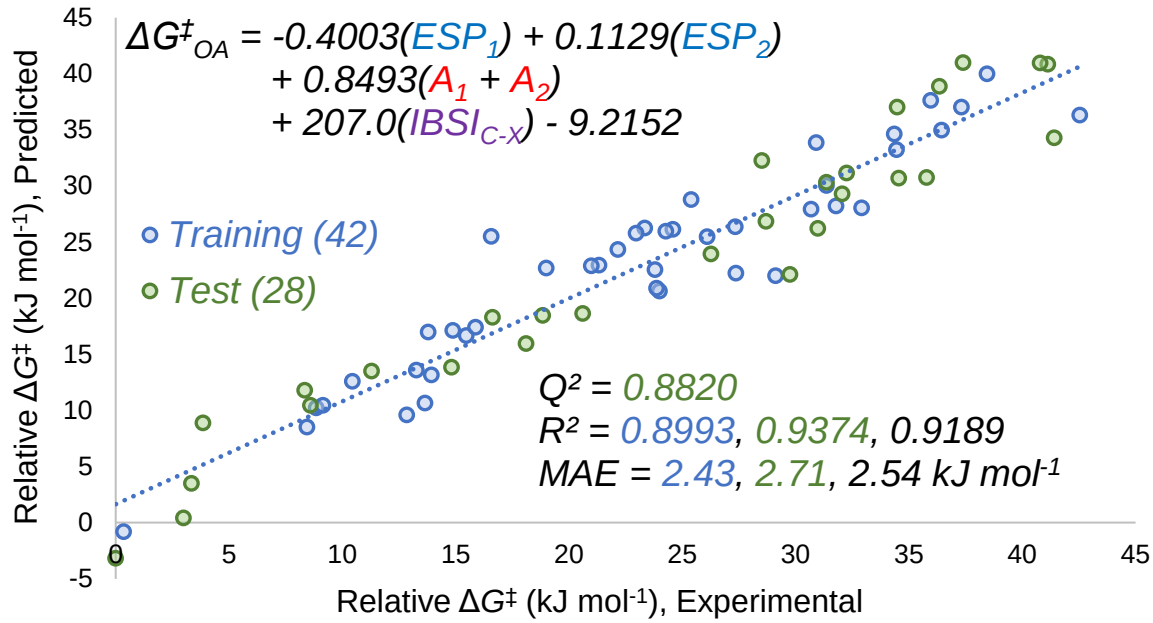

Fig. S61.
Multivariate linear regression model from one of the five 60/40 random split divisions (3/5).

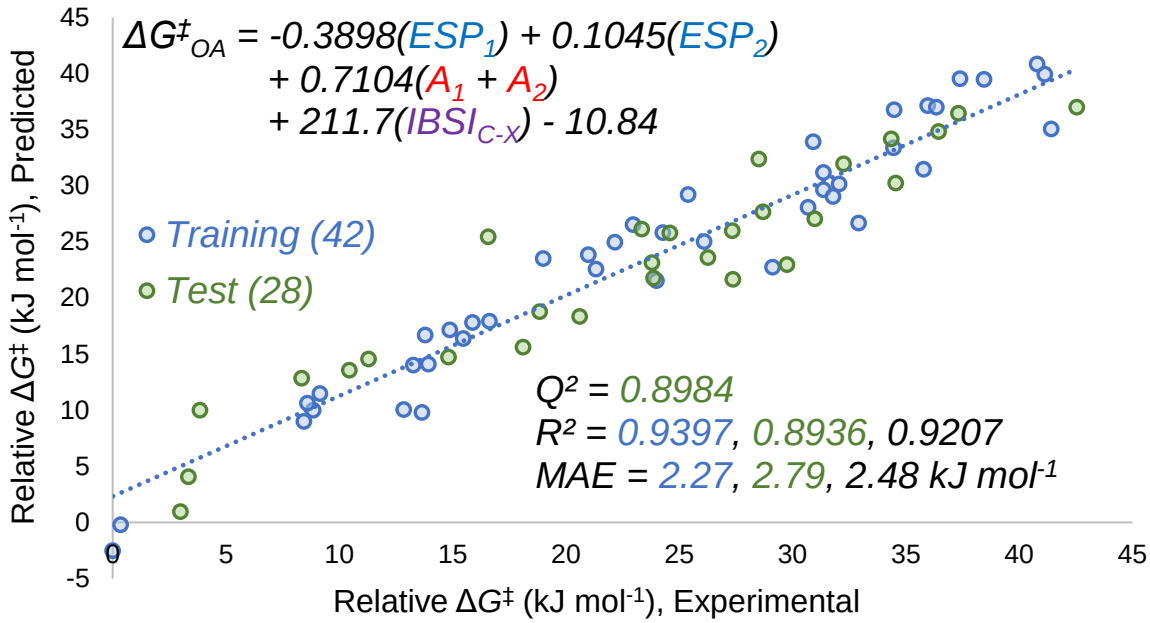

Fig. S62.
Multivariate linear regression model from one of the five 60/40 random split divisions (4/5).

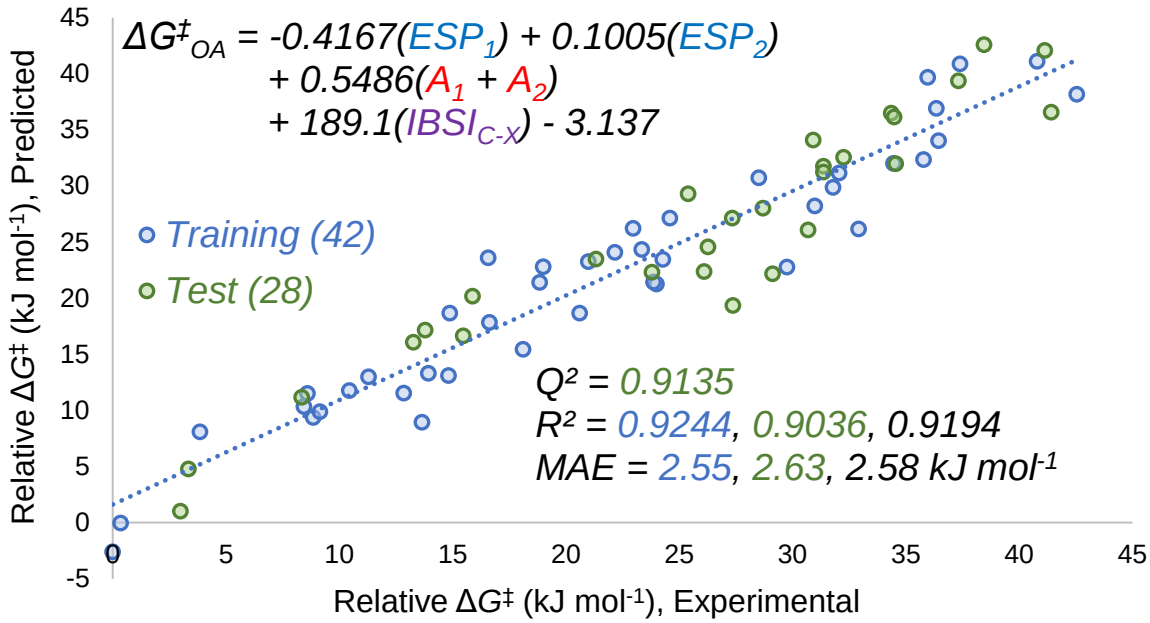

Fig. S63.
Multivariate linear regression model from one of the five 60/40 random split divisions (5/5).

The model performance was further evaluated by out-of-sample predictions. To test if the model can derive reliable prediction for molecules with a variety of structural features, we split the data set into a training set containing only the 2-halo pyridines, and a test set containing all other substrates. The model has achieved an excellent performance with a R^2 of 0.92 for the training set; a MAE of 2.68 kJ/mol and a Q^2 of 0.92 for the test set (Fig. S64).

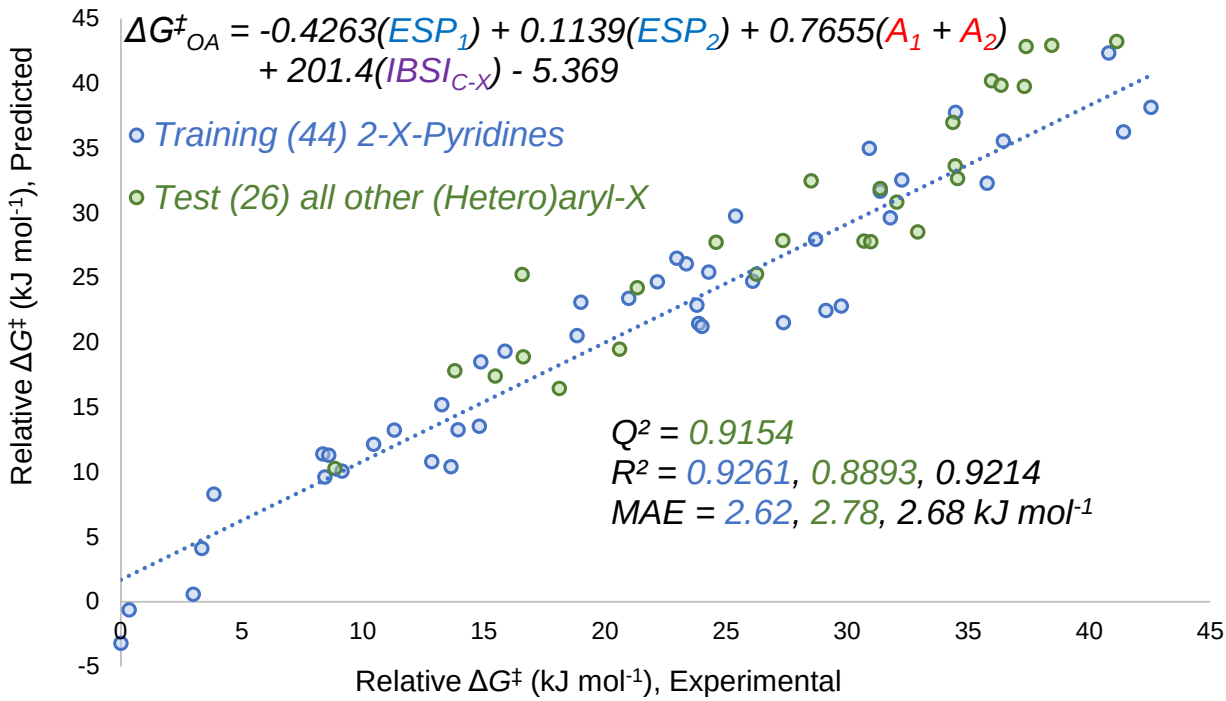

Fig. S64.
Multivariate linear regression model obtained using a training set containing all 2-halopyridines, and a test set containing all other substrates.

We performed another sample split and trained the model with just the mono-substituted (hetero)aryl halides, reserving multisubstituted (hetero)aryl halides as a test set (Fig. S65). This out-of-sample prediction has also showed an excellent performance with a R^2 of 0.92 for the training set; a MAE of 2.49 kJ/mol and a Q^2 of 0.93 for the test set.

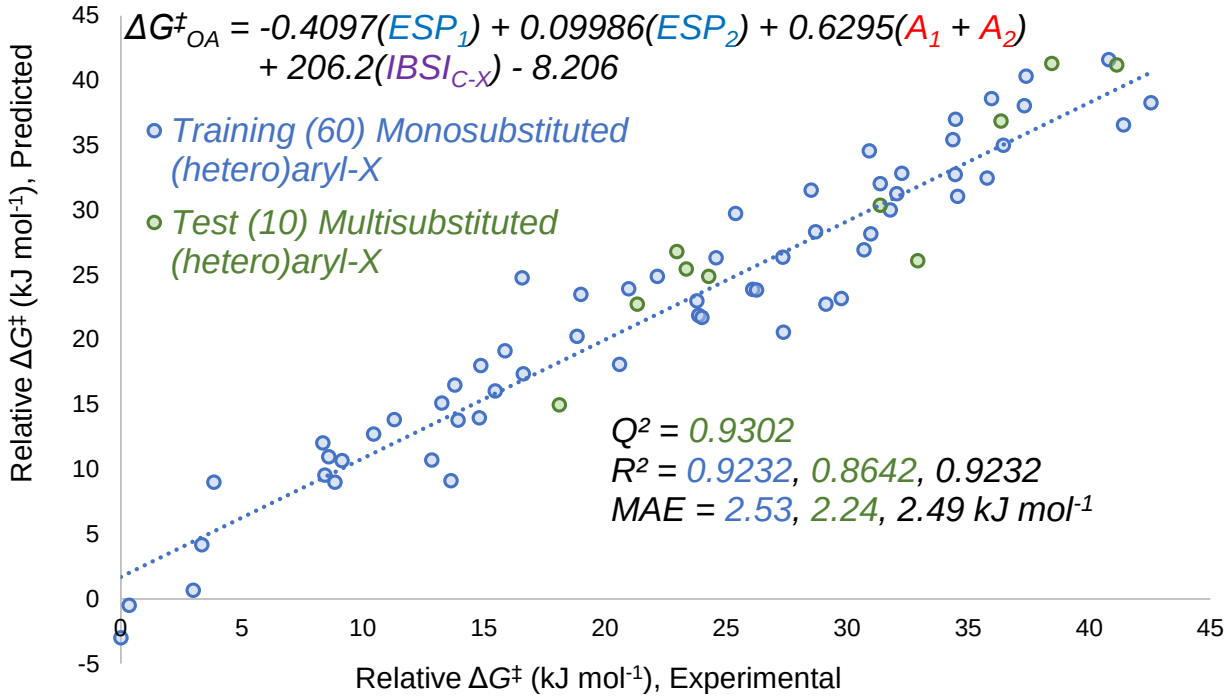

Fig. S65.
Multivariate linear regression model obtained using a training set containing all the monosubstituted (hetero)aryl halides, and a test set containing all the multisubstituted (hetero)aryl halides.

We also tested the model performance in predicting reactivity that falls outside the range of that in the training data set. We sorted the substrates by their observed $\Delta G^{\ddagger}_{OA}$ and performed out-of-sample predictions with an 80/20 (fast/slow) split (Fig. S66) and an 80/20 (slow/fast) split (Fig. S67). Both models have good predictive ability on the test set (MAE=2.90 kJ/mol, Q^2=0.87 for 80/20 (fast/slow) split; MAE=2.56 kJ/mol, Q^2=0.86 for 80/20 (slow/fast) split).

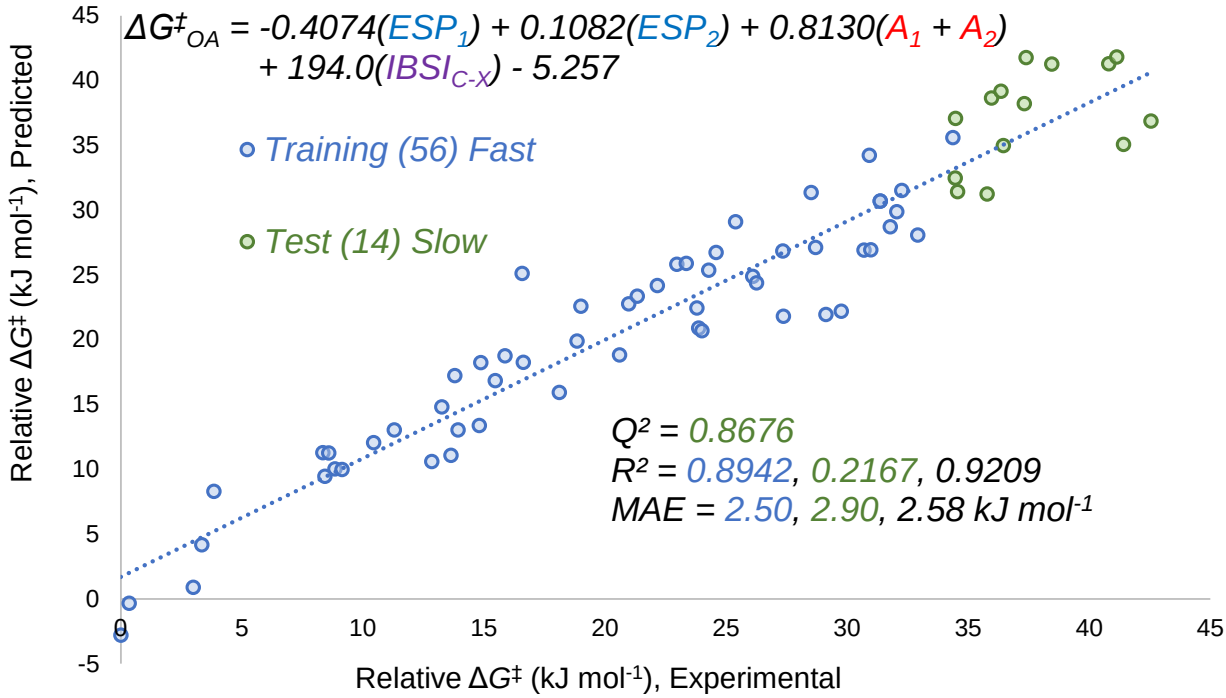

Fig. S66.
Multivariate linear regression model from the 80/20 (fast/slow) split.

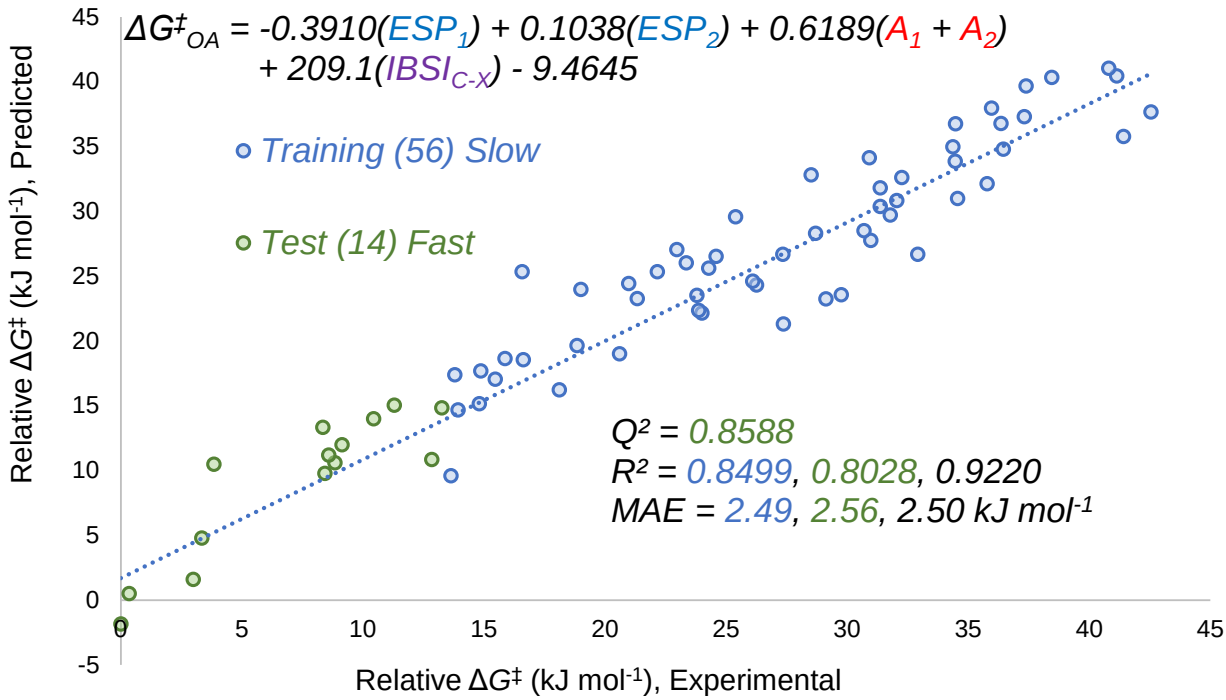

Fig. S67.
Multivariate linear regression model from the 80/20 (slow/fast) split.

Including Ar-OTf substrates into the predictive model

The inclusion of pK_a of the conjugate acid of the leaving group creates a unified predictive model that incorporates Ar-Cl, Ar-Br and Ar-OTf. The multivariate linear regression model constructed from those five descriptors (ESP_1, ESP_2, A_1+A_2, IBSI and pK_a) and the $\Delta G^{\ddagger}_{OA}$ of 79 substrates achieved excellent linear correlation with an R^2 of 0.93, and an MAE of 2.31 kJ/mol and has an expected random distribution of residuals and only one significant outlier as summarized in Figure S68.

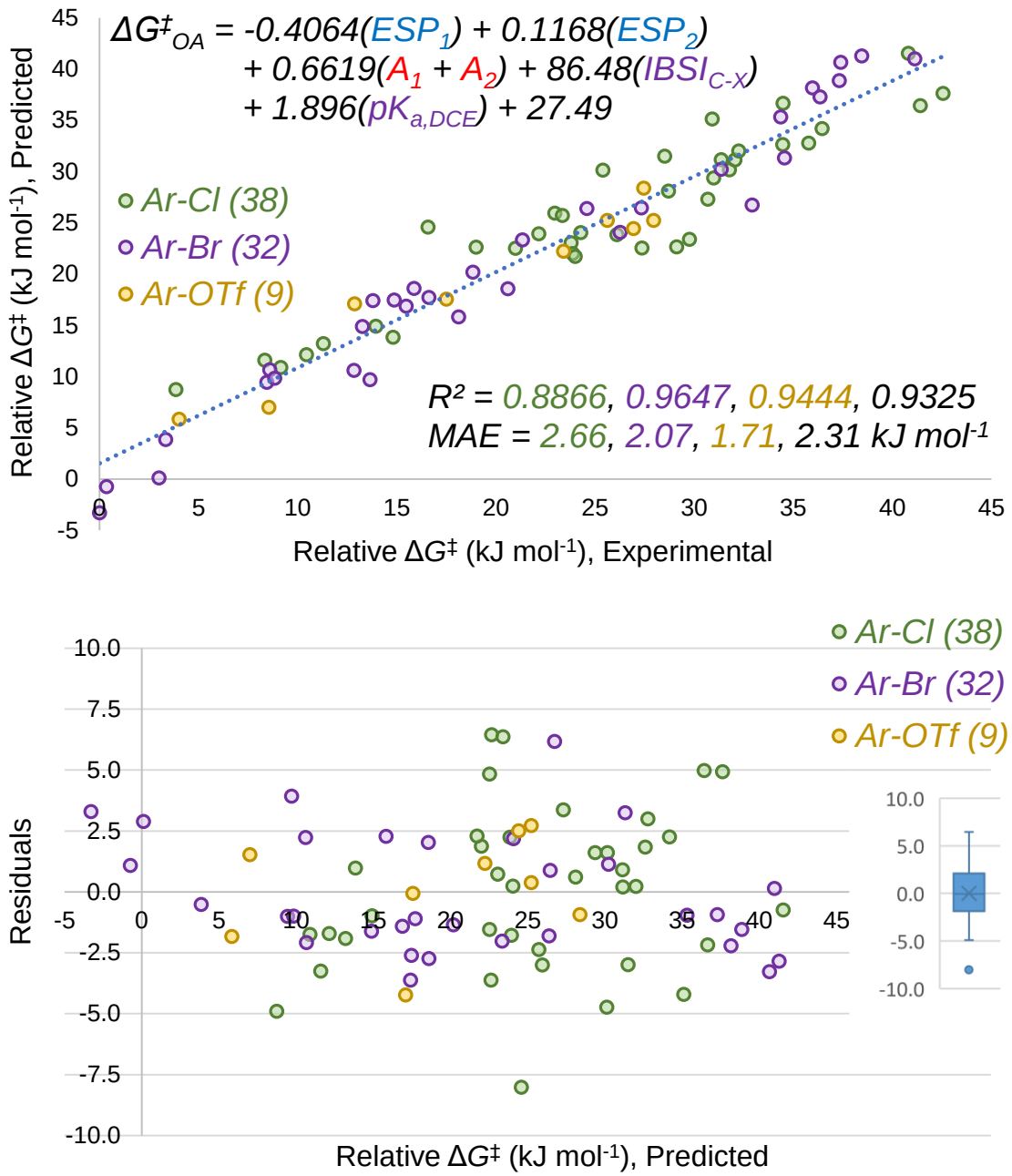

Fig. S68.
Multivariate linear regression model of $\Delta G^{\ddagger}_{OA}$ in THF for 79 substrates, including experimental versus predicted plot (top) and predicted versus residuals plot with corresponding box plot inset (bottom).

The model performance was evaluated by cross-validation with five random 60/40 training/test data splits. Excellent linear correlation was achieved between the observed and predicted $\Delta G^{\ddagger}_{OA}$, as indicated by the range of R^2 from 0.91 to 0.95 for training set, Q^2 from 0.90 to 0.93, and MAE from 2.18 kJ/mol to 2.91 kJ/mol for the test set (Figure S69 to Figure S73).

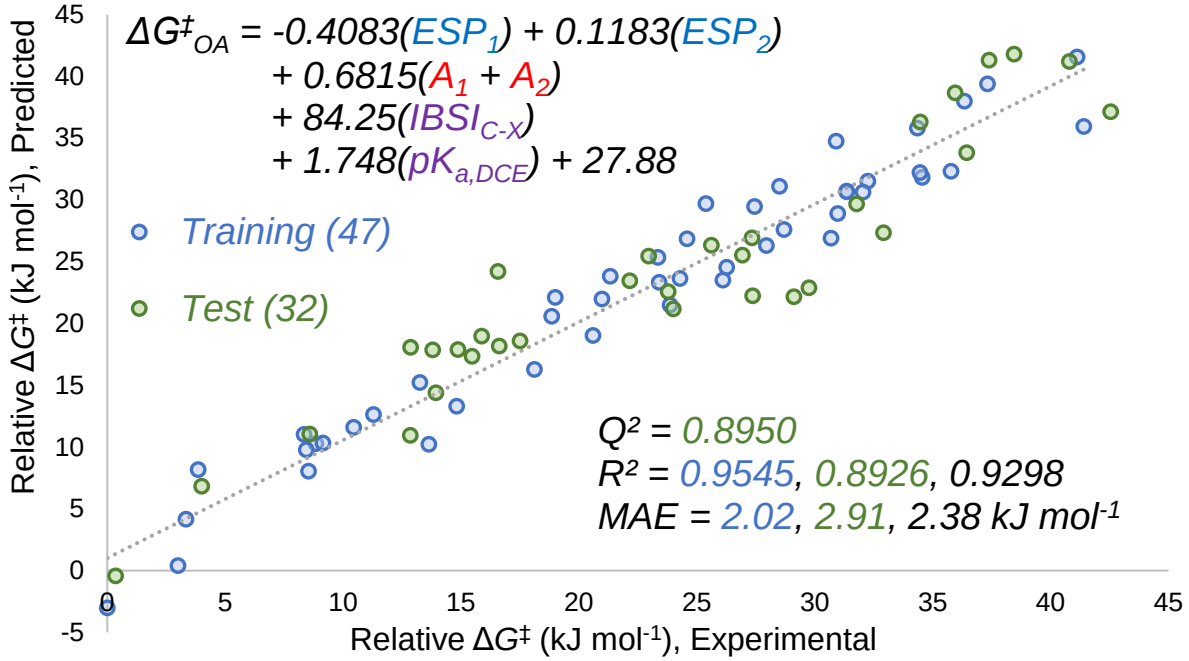

Fig. S69.
Multivariate linear regression model from one of the five 60/40 random split divisions (1/5).

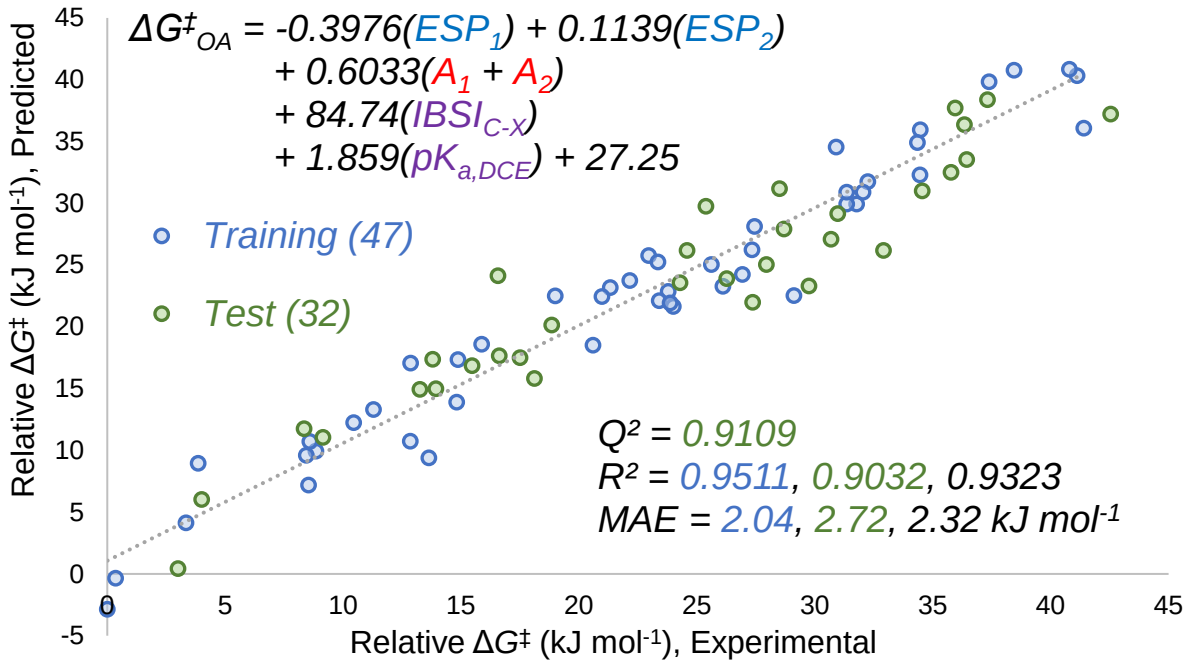

Fig. S70.
Multivariate linear regression model from one of the five 60/40 random split divisions (2/5).

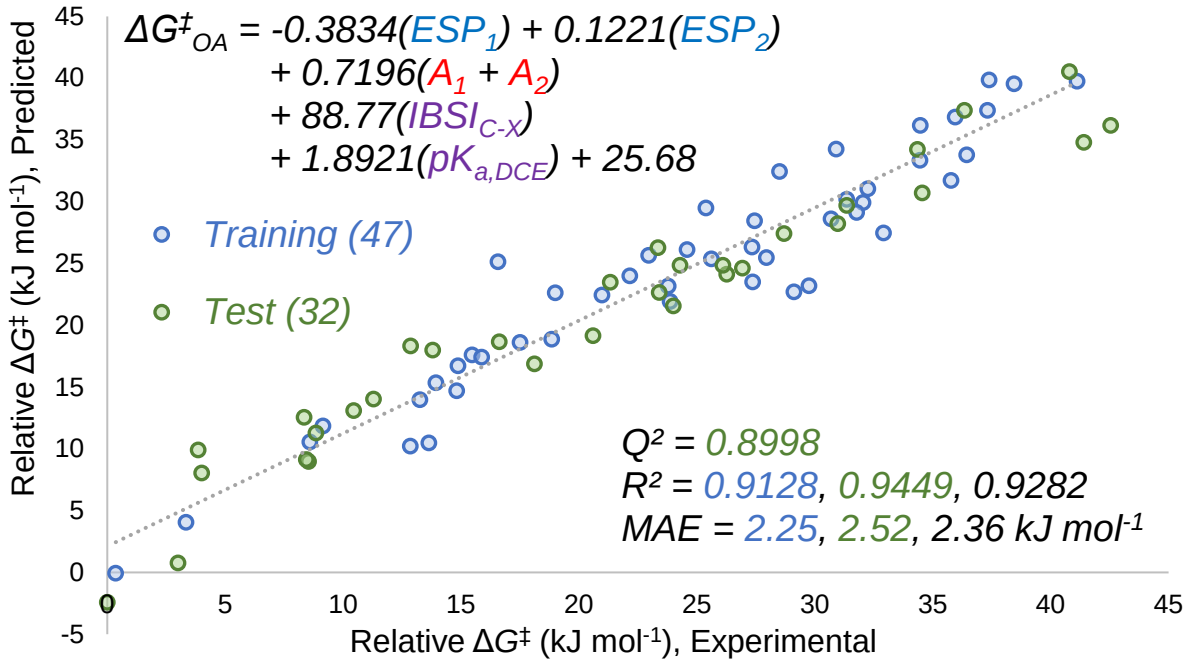

Fig. S71.
Multivariate linear regression model from one of the five 60/40 random split divisions (3/5).

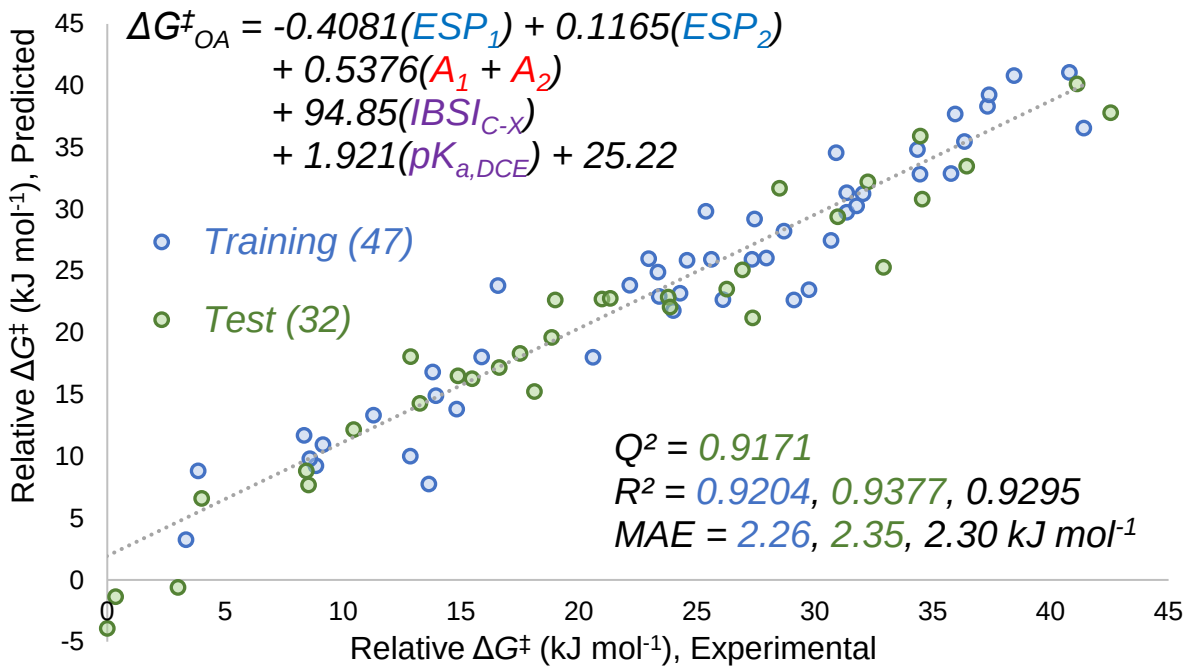

Fig. S72.
Multivariate linear regression model from one of the five 60/40 random split divisions (4/5).

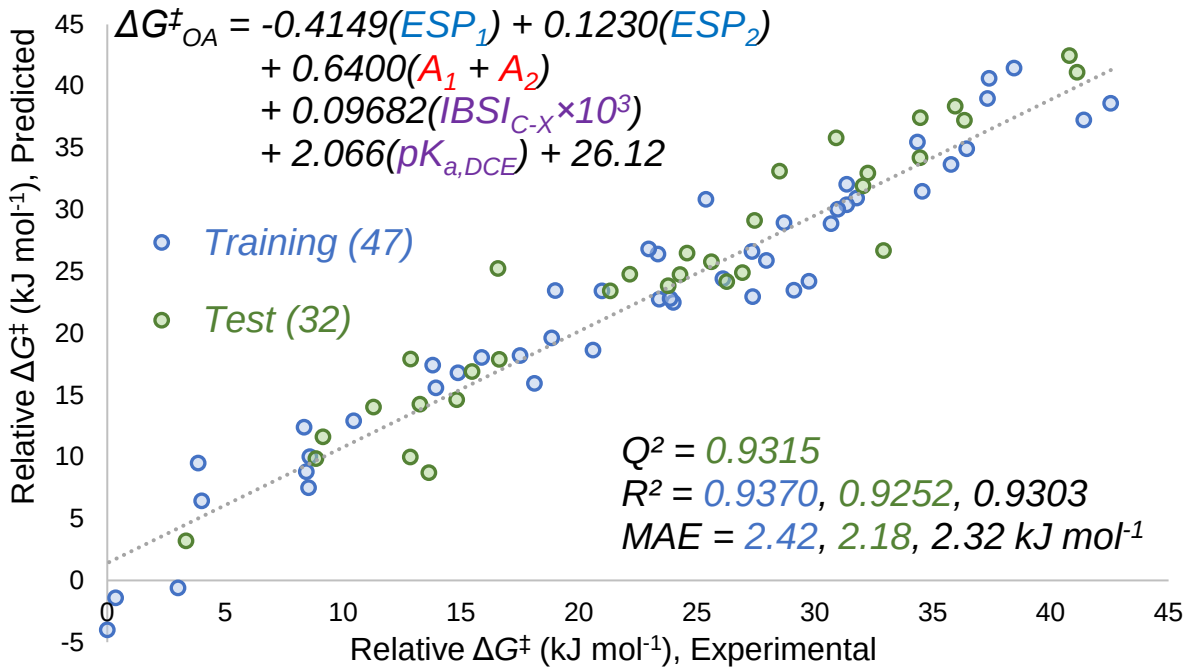

Fig. S73.
Multivariate linear regression model from one of the five 60/40 random split divisions (5/5).

Sonogashira Initial Rate Prediction Modelling

To build the predictive model for Sonogashira initial rates, we calculated the key molecular descriptors and the predicted $\Delta G^{\ddagger}_{OA}$ for each of the 29 aryl bromides in substrate sets #1 and #2 (Table S9). Linear correlations of the predicted $\Delta G^{\ddagger}_{OA}$ with ln *k* for each Sonogashira reaction using a particular phosphine are shown in Figs. S74 and S75. For the 10 phosphines in Fig. S74, only substrate set #1 is used, while the 7 phosphines in Fig. S75 include data from both substrate sets. Good to excellent linear correlations are observed (R^2 = 0.79-0.92) across the data for all 17 phosphines; only one substrate appears to be a significant outlier: 1-bromo-2,4,6-triisopropylbenzene, where the Sonogashira reaction rate is much lower than expected based on the predicted $\Delta G^{\ddagger}_{OA}$.

Table S9.
Predicted $\Delta G^{\ddagger}_{OA}$ and molecular descriptors for the Sonogashira substrates.

Aryl Bromide	Substrate Set #	Predicted $\Delta G^{\ddagger}_{OA}$ (kJ/mol)	Average ESP_1 (kJ/mol)	Average ESP_2 (kJ/mol)	$A_1 + A_2$ (kJ/mol)	*IBSI* (unitless)
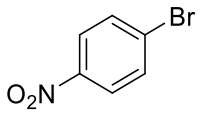 4-bromonitrobenzene	1	16.906	72.672	61.696	0.000	0.235
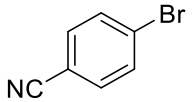 4-bromobenzonitrile	1	18.322	67.918	57.769	0.000	0.234
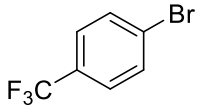 1-bromo-4-trifluoromethylbenzene	1	23.896	48.628	38.695	0.000	0.233
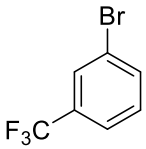 1-bromo-3-trifluoromethylbenzene	1	25.083	46.655	39.882	0.000	0.235
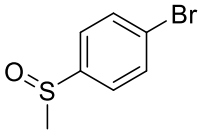 4-bromophenyl methyl sulfoxide	1	25.469	36.957	25.581	0.000	0.225
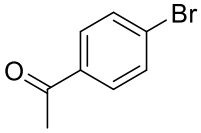 4-bromoacetophenone	1	26.265	38.035	22.523	0.000	0.232

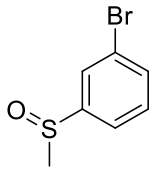 3-bromophenyl methyl sulfoxide	1	26.269	39.640	27.443	0.000	0.233
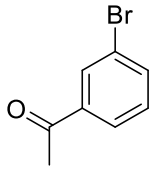 3-bromoacetophenone	1	27.495	36.584	29.131	0.000	0.232
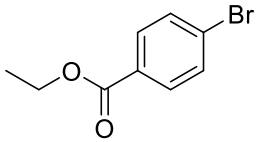 ethyl 4-bromobenzoate	1	28.910	28.942	14.829	0.000	0.231
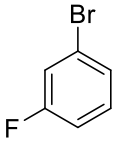 1-bromo-3-fluorobenzene	1	29.298	28.373	14.017	0.000	0.232
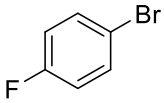 1-bromo-4-fluorobenzene	1	30.912	24.813	20.439	0.000	0.230
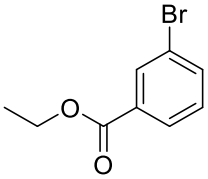 ethyl 3-bromobenzoate	1	31.530	25.643	19.356	0.000	0.235
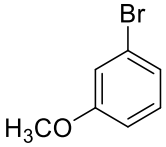 3-bromoanisole	1	34.825	9.511	-3.357	0.000	0.231
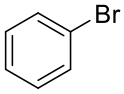 bromobenzene	1	35.115	8.664	-1.260	0.000	0.229
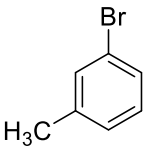 3-bromotoluene	1	37.218	0.913	-11.000	0.000	0.229

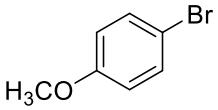 4-bromoanisole	1	37.648	-4.712	-10.511	0.000	0.220
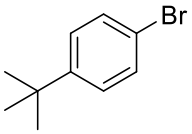 1-bromo-4-*tert*-butylbenzene	1	37.892	-2.253	-11.654	0.000	0.227
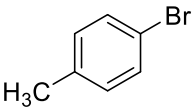 4-bromotoluene	1	38.210	-0.306	-8.976	0.000	0.231
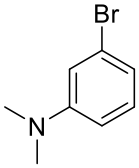 3-bromo-*N*,*N*-dimethylaniline	1	43.502	-24.157	-43.125	0.000	0.227
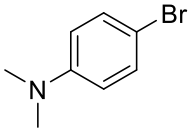 4-bromo-*N*,*N*-dimethylaniline	1	47.378	-29.162	-32.835	0.000	0.231
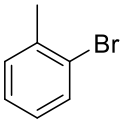 2-bromotoluene	2	40.924	4.239	-9.733	7.280	0.226
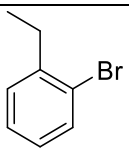 2-bromoethylbenzene	2	42.502	1.412	-12.784	7.489	0.229
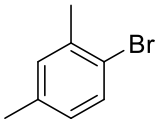 1-bromo-2,4-dimethylbenzene	2	43.701	-4.761	-17.557	7.280	0.226

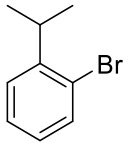 1-bromo-2-isopropylbenzene	2	44.156	1.293	2.540	9.247	0.223
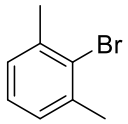 2,6-dimethyl bromobenzene	2	48.905	-1.239	1.384	14.560	0.222
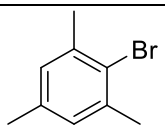 2,4,6-trimethyl bromobenzene	2	51.682	-9.080	-4.830	14.560	0.223
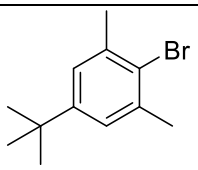 4-*tert*-butyl-2,6-dimethyl bromobenzene	2	52.164	-10.010	-6.797	14.560	0.224
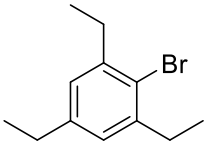 2,4,6-triethyl bromobenzene	2	52.500	-10.545	-11.238	14.979	0.226
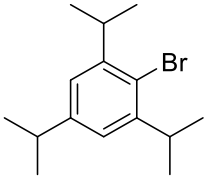 2,4,6-triisopropyl bromobenzene	2	53.561	-11.011	-12.996	18.493	0.218

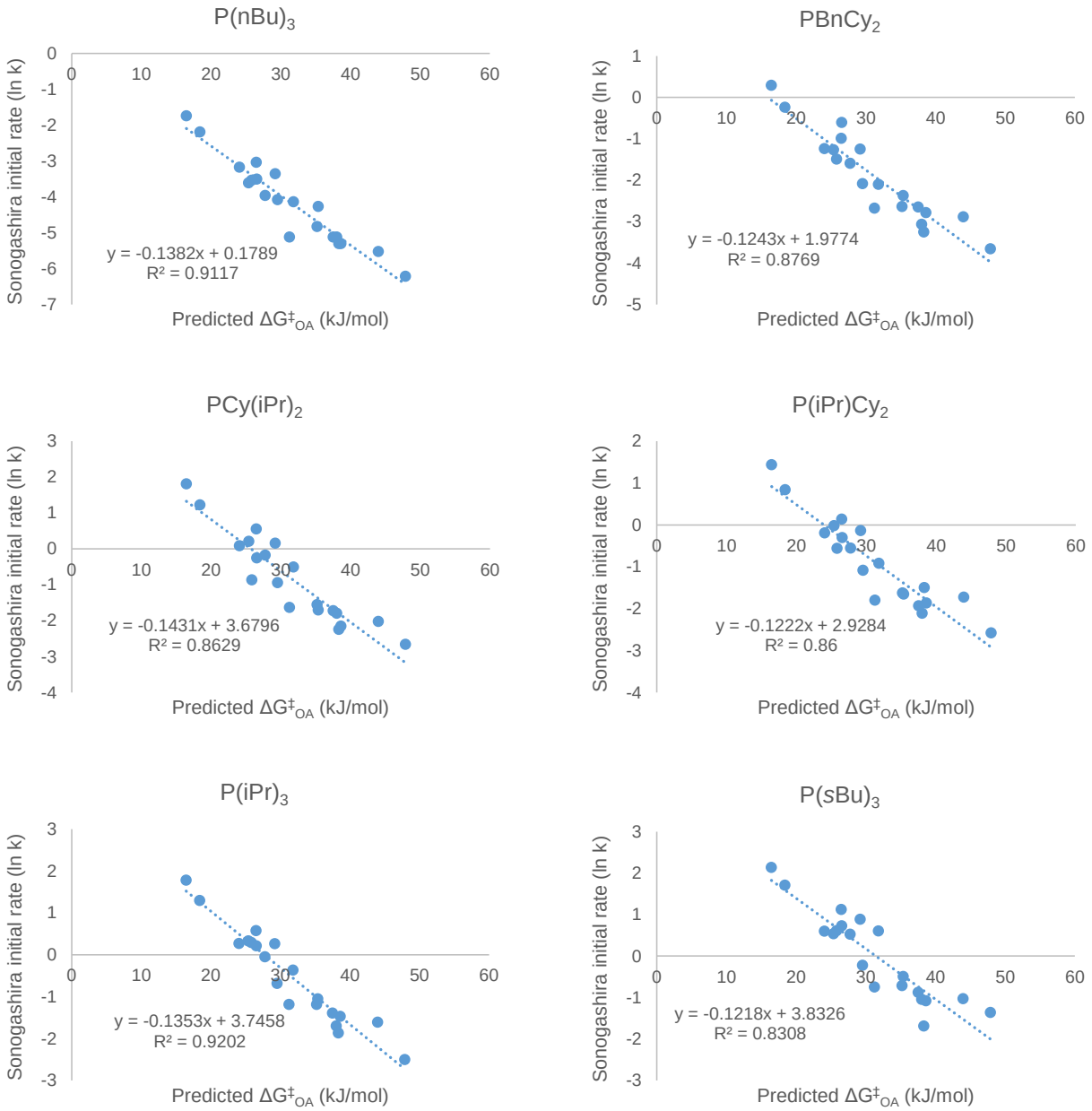

Fig. S74.
Univariate correlations between ln k for Sonogashira reactions and the predicted $\Delta G^{\ddagger}_{OA}$ for each substrate across 10 ligands used only with substrate set #1.

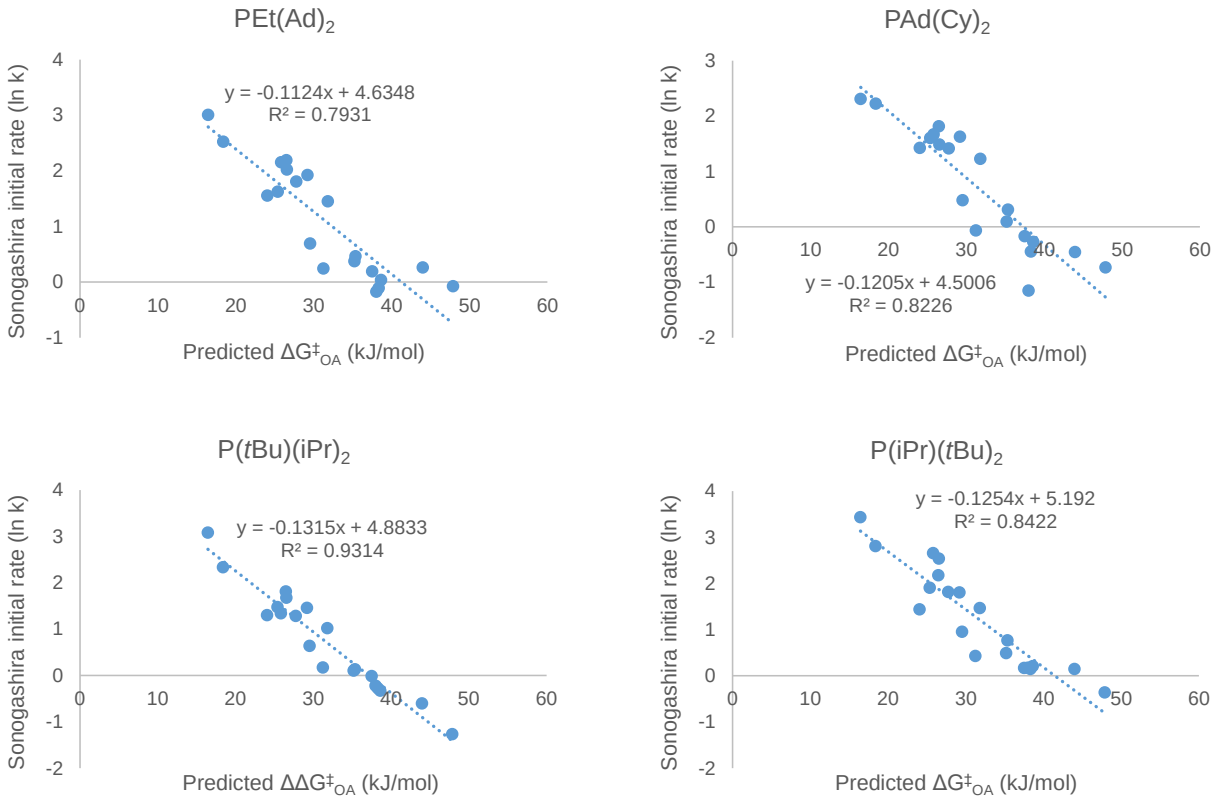

Fig. S74 continued.
Linear correlations between ln k for Sonogashira reactions and predicted $\Delta G^{\ddagger}_{OA}$ for each substrate across 10 ligands used only with substrate set #1.

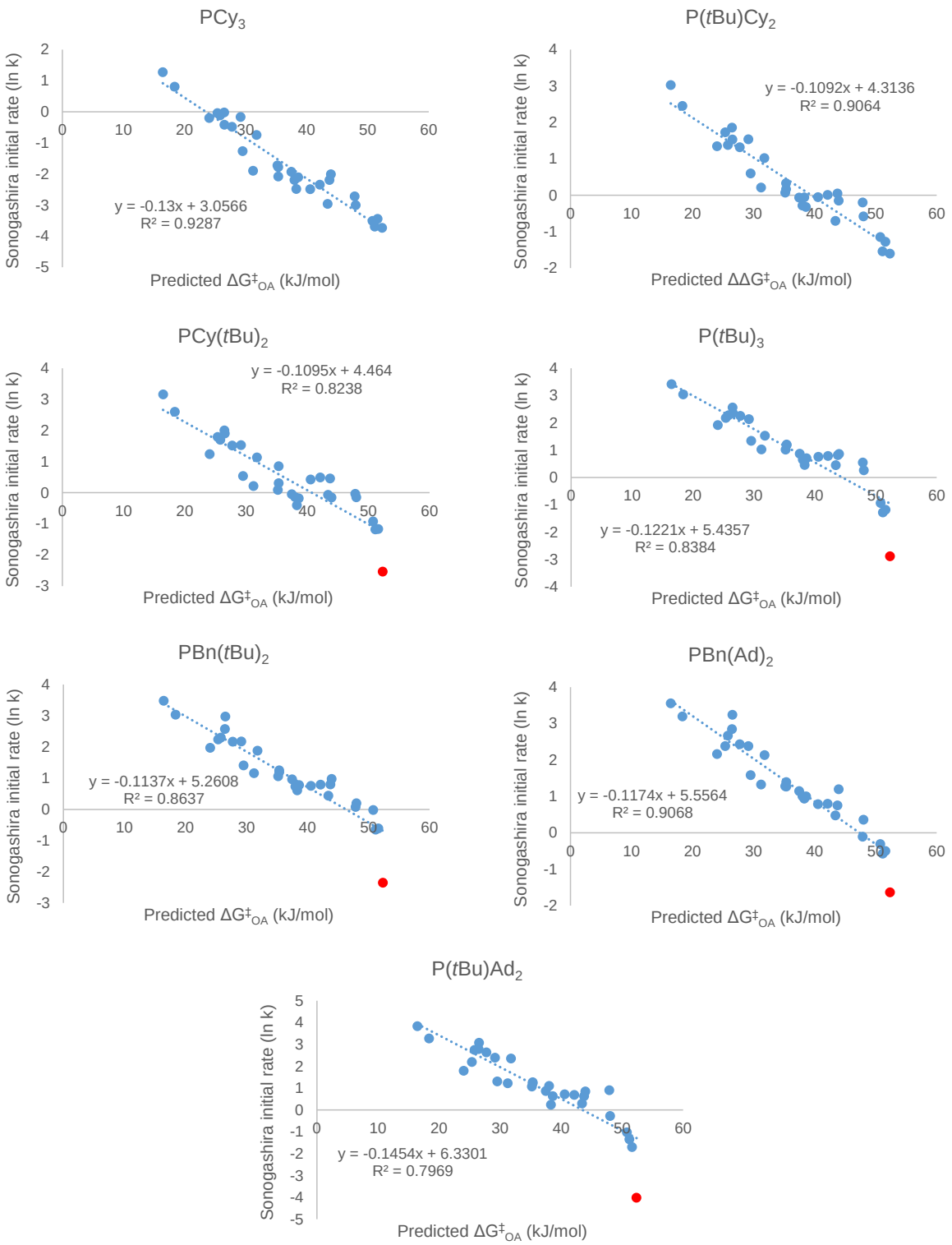

Fig. S75.
Linear correlations between ln k for Sonogashira reactions and predicted $\Delta G^{\ddagger}_{OA}$ across 7 ligands used with substrate sets #1 & #2. Red points are outliers (1-bromo-2,4,6-triisopropylbenzene), which are included in the regression analysis.

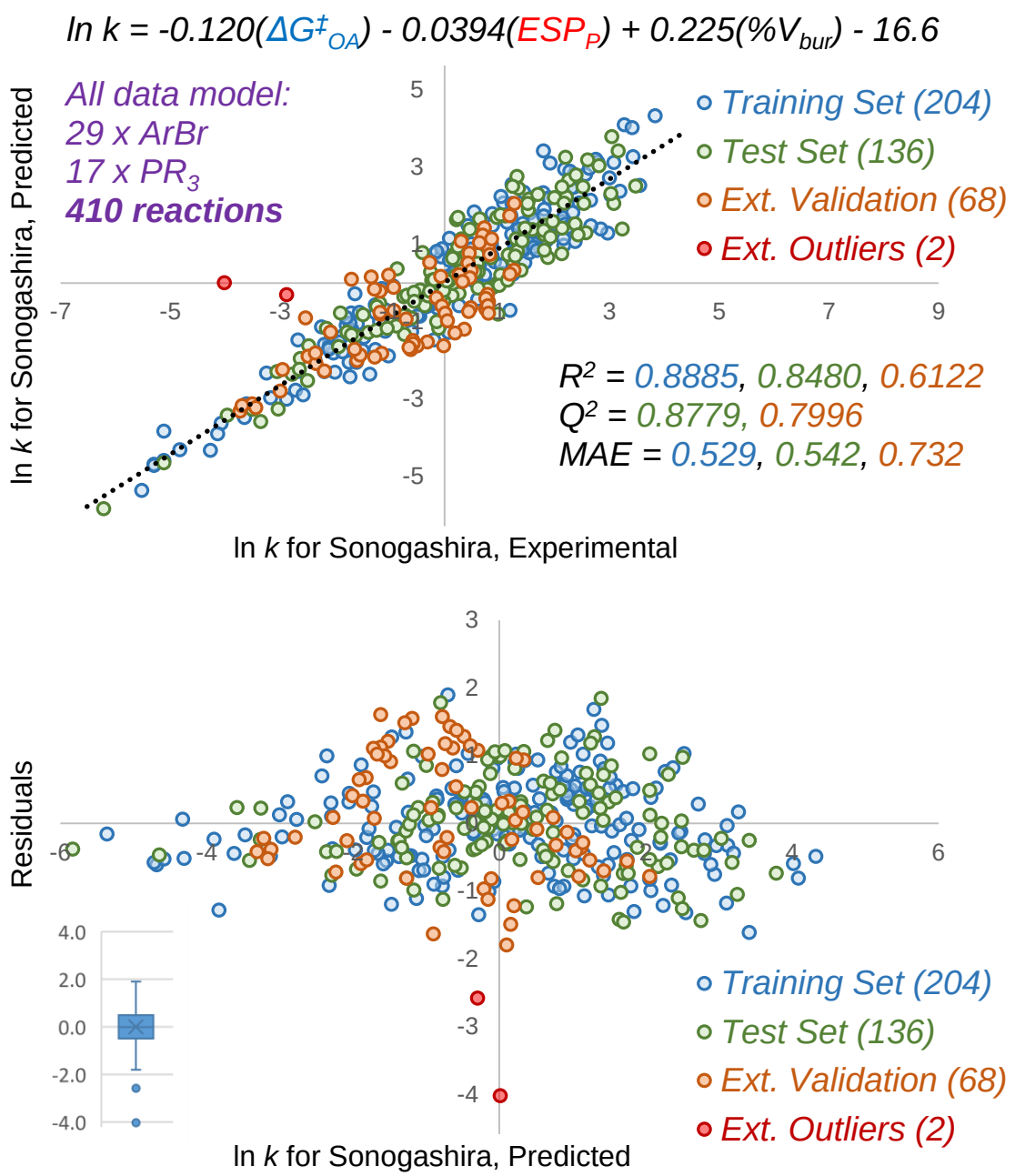

Fig. S76.
Unified Sonogashira coupling rate predictive model constructed using the electronic and steric descriptors of free phosphines and predicted $\Delta G^{\ddagger}_{OA}$ for the entire set of 410 reactions, including plot of experimental versus predicted ln k values (top) and plot of predicted versus residuals with corresponding box plot inset (bottom), showing two outliers (red data points in main plots).

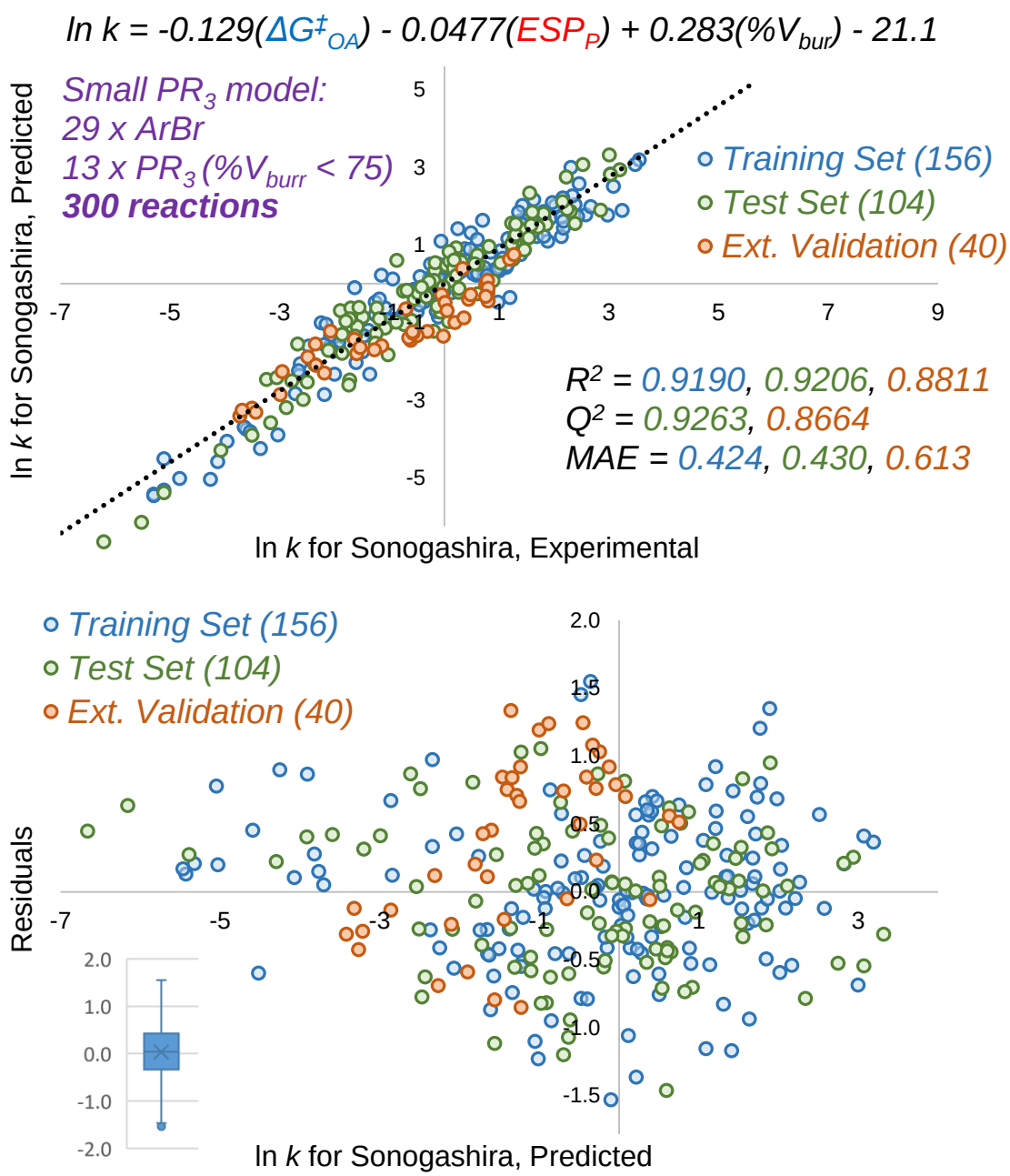

Fig. S77.
Unified Sonogashira coupling rate predictive model constructed using the electronic and steric descriptors of free phosphines and predicted $\Delta G^{\ddagger}_{OA}$ for the set of phosphines with $\%V_{bur} < 75$ (300 reactions), including plot of experimental versus predicted ln k values (top) and plot of predicted versus residuals with corresponding box plot inset (bottom), showing no significant outliers.

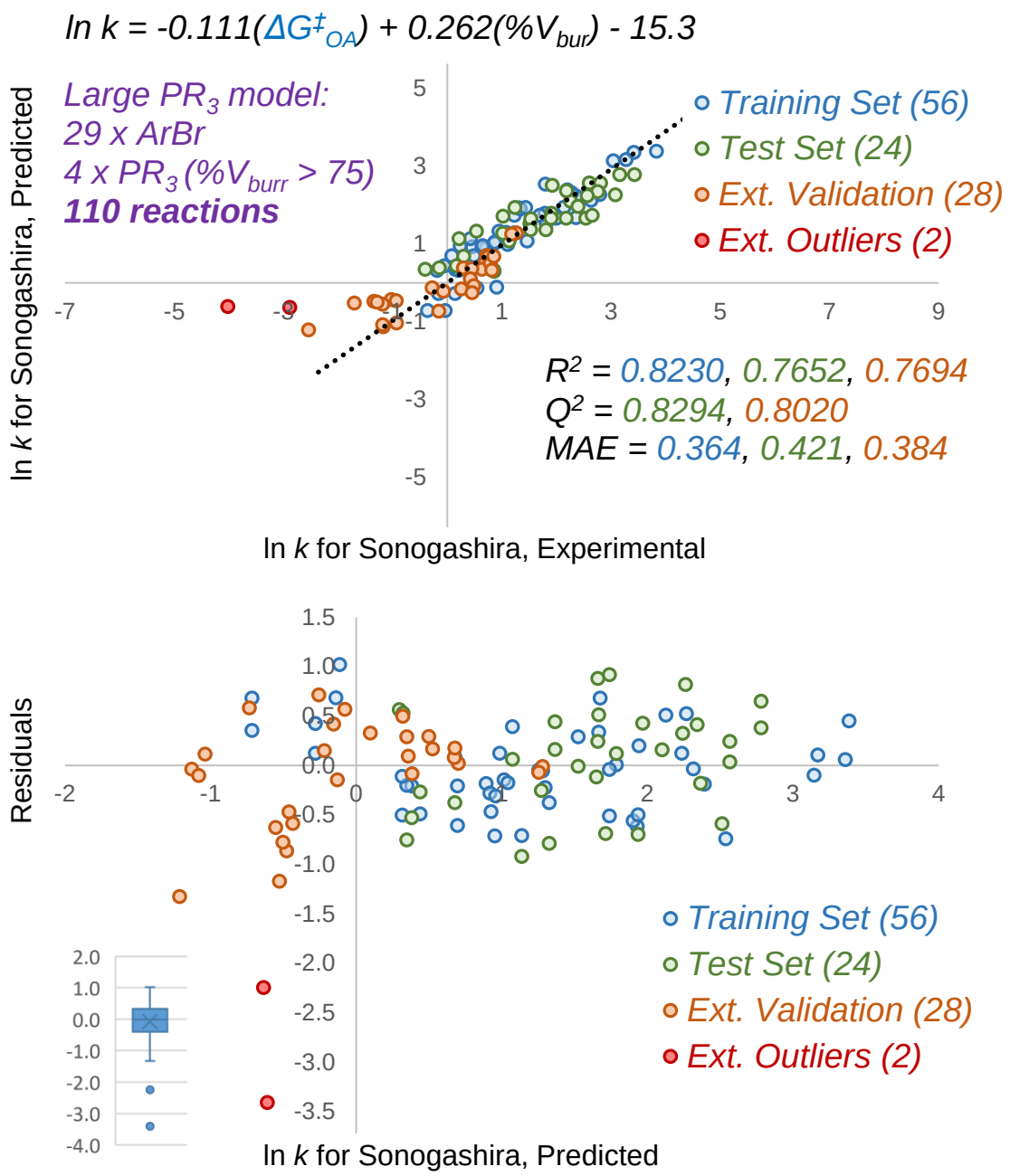

Fig. S78.
Unified Sonogashira coupling rate predictive model constructed using the electronic and steric descriptors of free phosphines and predicted $\Delta G^{\ddagger}_{OA}$ for the set of phosphines with $\%V_{bur} > 75$ (110 reactions), including plot of experimental versus predicted ln k values (top) and plot of predicted versus residuals with corresponding box plot inset (bottom), showing two outliers (red data points in main plots).

To build the unified model shown in Fig. 4 in the main text, we evaluated several molecular descriptors related to the 17 phosphine ligands. Molecular ESP values and $\%V_{bur}$ were calculated for the corresponding PdL_2 and PdL complexes, as well as the "free" phosphines (Table S6).

To evaluate these different catalyst descriptors, we constructed similar multivariate linear regression models using a combination of catalyst ESP and $\%V_{bur}$ with the predicted $\Delta G^{\ddagger}_{OA}$ for each substrate. The training/test sets were generated by a random 60/40 split of the substrate set #1 data, and the substrate #2 data was retained as an external test set. The models corresponding to catalyst descriptors for PdL_2 and PdL are shown in Figs. S79 and S80, respectively. Note that for PdL, the $\%V_{bur}$ term has a very small coefficient when included in the regression analysis; therefore, we opted to exclude it from the model shown in Fig. S77. Notably, both alternative catalyst descriptors underperform the free phosphine descriptors (Fig. 3C-E) with respect to linear correlation and predictive ability with this data set.

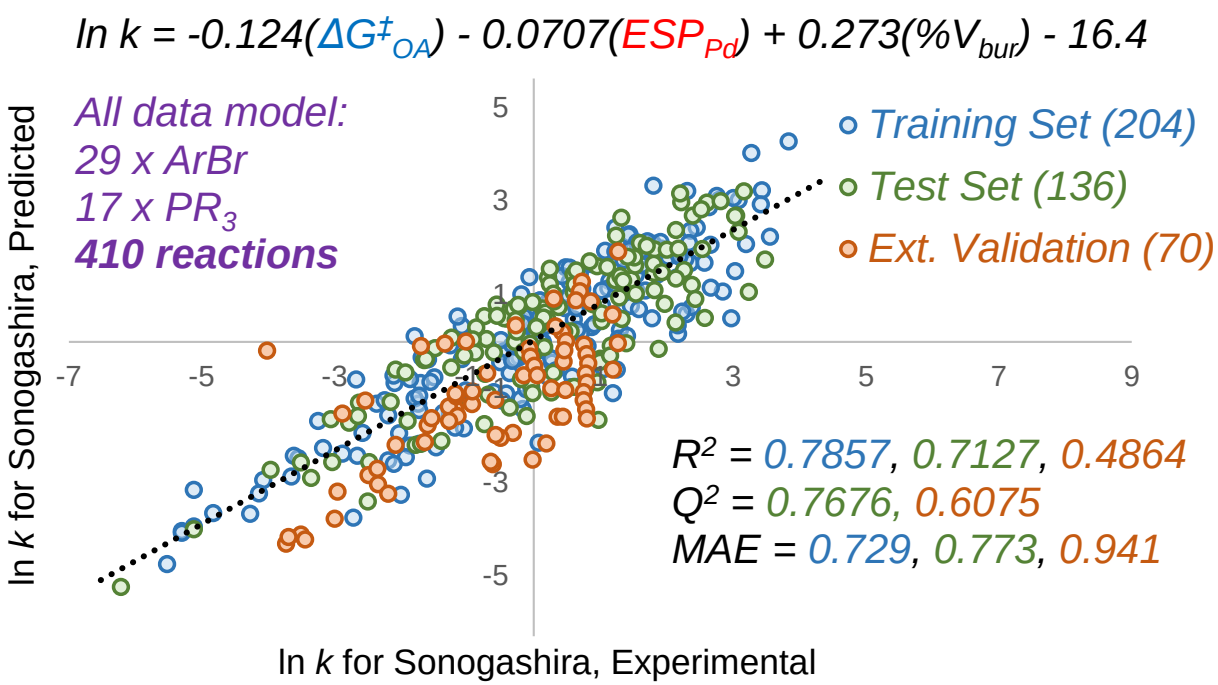

Fig. S79.
Unified Sonogashira coupling rate predictive model constructed using the electronic and steric descriptors of PdL_2 and predicted $\Delta G^{\ddagger}_{OA}$ for the entire set of 410 reactions.

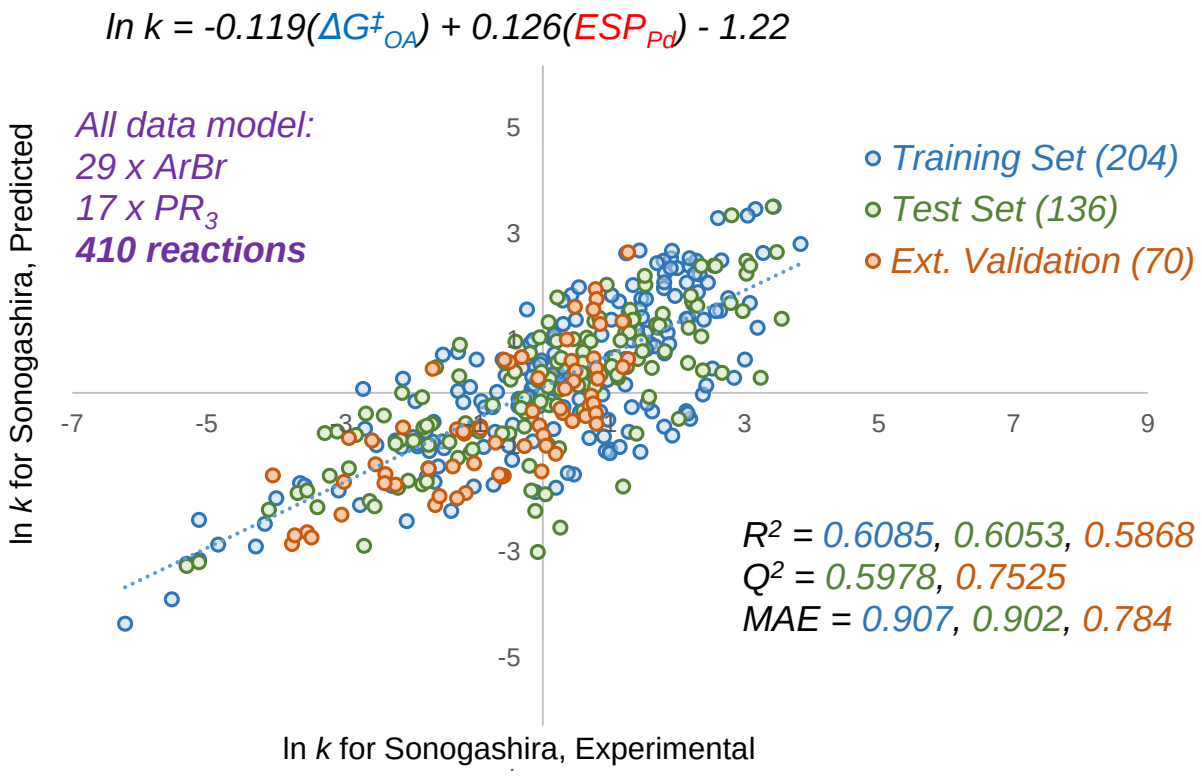

Fig. S80.
Unified Sonogashira coupling rate predictive model constructed using the electronic and steric descriptors of PdL and predicted $\Delta G^{\ddagger}_{OA}$ for the entire set of 410 reactions.

Site Selectivity Predictions

Molecular descriptors for each of the substrates shown in Table S10 were obtained following the procedure used for the oxidative addition substrates. The predicted $\Delta G^{\ddagger}_{OA}$ for each C–X (X = Cl, Br) site was calculated using the equation from Fig. 2C.

Table S10.
Molecular descriptors and predicted $\Delta G^{\ddagger}_{OA}$ for multihalogenated heterocycles. Purple sphere indicates observed major site of cross-coupling.

Heterocycle	C–X site	Predicted $\Delta G^{\ddagger}_{OA}$ (kJ/mol)	*ESP₁* (kJ/mol)	*ESP₂* (kJ/mol)	$A_1 + A_2$ (kJ/mol)	*IBSI*	Ref. for observed select.
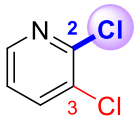	**C2**	24.7	60.0	-61.4	2.22	0.3026	(21)
	C3	38.9	63.9	57.9	2.22	0.3197	
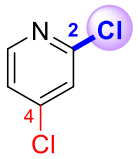	**C2**	21.2	60.2	-62.7	0.00	0.2937	(21)
	C4	31.1	72.0	56.4	0.00	0.3058	
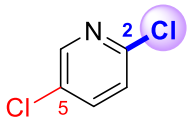	**C2**	21.6	60.4	-57.7	0.00	0.2937	(21)
	C5	35.6	63.6	66.4	0.00	0.3056	
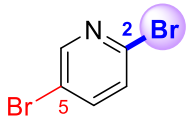	**C2**	9.5	57.0	-52.8	0.00	0.2249	(21)
	C5	21.0	64.4	61.1	0.00	0.2384	
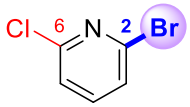	**C2**	11.0	57.6	-51.7	2.22	0.2256	(21)
	C6	22.7	64.0	-51.7	2.01	0.2966	
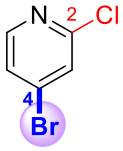	C2	21.7	60.8	-61.2	0.00	0.2966	(21)
	C4	16.9	68.4	52.9	0.00	0.2301	
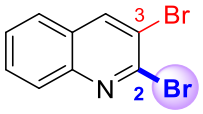	**C2**	13.0	51.6	-59.5	2.01	0.2280	(21)
	C3	26.6	53.1	53.4	2.01	0.2405	
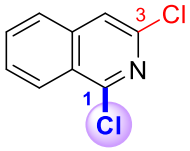	**C1**	20.6	63.0	-62.2	0.00	0.2963	(21)
	C3	28.1	45.0	-62.2	0.00	0.2972	

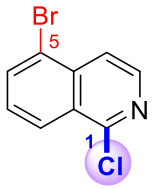	**C1**	21.0	56.8	-71.5	0.00	0.2905	(21)
	C5	24.0	49.4	39.8	0.00	0.2335	
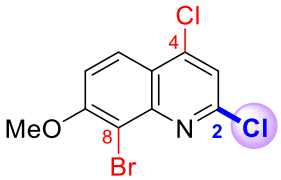	**C2**	21.7	51.6	-75.2	0.00	0.2856	(21)
	C4	34.4	66.1	45.9	2.22	0.3082	
	C8	41.0	18.8	45.8	3.14	0.2431	
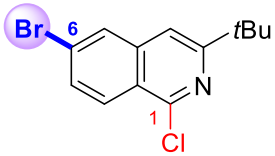	C1	38.4	48.5	-54.4	20.50	0.2828	(21)
	C6	26.4	39.3	26.3	0.00	0.2325	
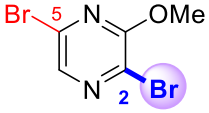	**C2**	2.8	84.5	-29.9	3.14	0.2249	(22)
	C5	8.0	71.4	-41.2	3.14	0.2298	
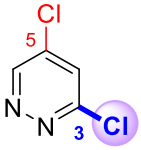	**C3**	9.5	95.2	-64.5	0.00	0.3073	(23)
	C5	20.0	111.5	92.5	0.00	0.3115	
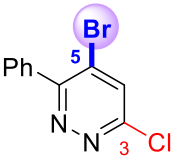	C4	17.9	91.6	87.0	11.72	0.2255	(21)
	C6	15.8	82.0	-68.5	0.00	0.3140	
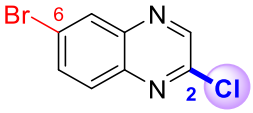	**C2**	13.8	87.9	-32.9	0.00	0.2976	(21)
	C6	24.3	49.6	42.4	0.00	0.2342	
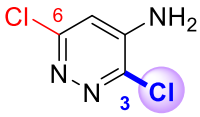	**C3**	16.5	77.2	-81.5	5.15	0.2972	(21)
	C6	19.3	58.6	-99.0	0.00	0.2999	
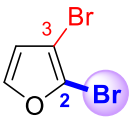	**C2**	27.3	46.5	-1.2	2.01	0.2586	(21)
	C3	33.5	29.9	14.4	2.01	0.2476	

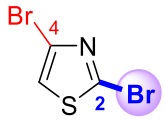	**C2**	7.6	73.7	-49.4	2.01	0.2406	(21)
	C4	17.0	47.6	-49.4	2.01	0.2344	
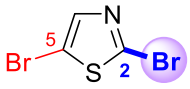	**C2**	8.8	68.5	-53.8	0.00	0.245	(21)
	C5	22.5	62.6	41.0	0.00	0.252	
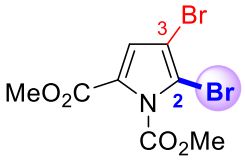	**C2**	29.9	51.9	26.5	7.03	0.2514	(21)
	C3	36.6	26.5	13.1	2.01	0.2571	
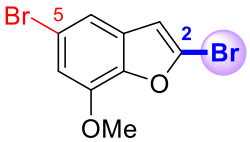	**C2**	22.4	56.8	21.0	0.00	0.2504	(21)
	C5	37.2	1.2	-4.8	0.00	0.2251	
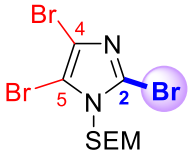	**C2**	15.7	43.4	-99.5	2.01	0.2449	(21)
	C4	30.6	12.8	-99.5	4.02	0.2506	
	C5	30.3	49.0	12.8	7.36	0.2536	
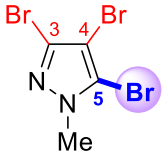	C3	26.0	31.6	-60.4	1.59	0.254	(21)
	C4	34.7	35.9	31.6	3.18	0.253	
	C5	24.6	72.0	35.9	8.70	0.255	
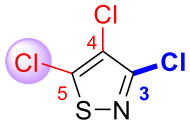	C3	22.6	83.7	-25.1	2.22	0.322	(21)
	C4	36.6	84.3	83.7	4.44	0.329	
	C5	35.4	94.9	91.0	2.22	0.348	
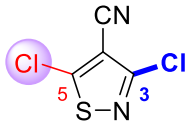	C3	11.7	115.8	4.7	0.88	0.321	(21)
	C5	21.1	134.3	120.1	0.88	0.346	

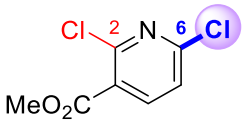	C2	24.3	71.5	-46.7	5.02	0.3073	(24)
	C6	18.9	77.1	-46.7	2.22	0.3010	
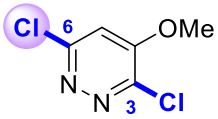	C3	12.8	94.8	-62.8	3.14	0.3114	(25)
	C6	12.1	86.9	-70.0	0.00	0.3066	
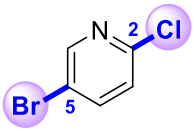	C2	21.6	61.4	-56.1	0.00	0.2949	(26, 27)
	C5	21.5	62.5	59.6	0.00	0.2376	
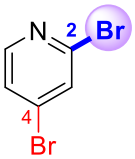	**C2**	9.1	56.1	-57.9	0.00	0.2236	(28, 29)
	C4	17.1	69.9	54.9	0.00	0.2330	
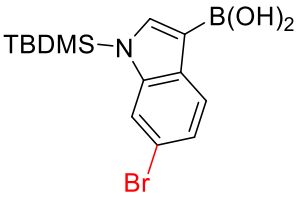		46.2	-32.7	-51.4	0.00	0.2251	(22)
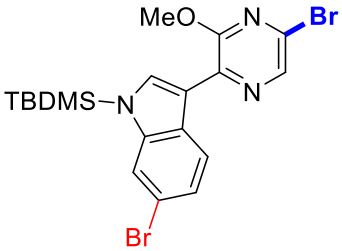	**blue**	21.0	39.6	-31.5	3.14	0.2253	(22)
	red	40.4	-12.9	-30.3	0.00	0.2256	
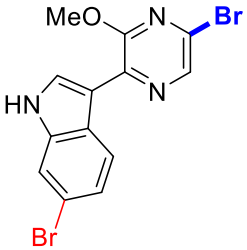	**blue**	19.3	45.4	-26.4	3.14	0.2257	(22)
	red	38.3	-5.1	-22.5	0	0.2267	
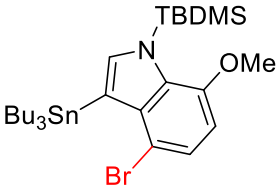		46.5	-34.6	-46.9	0	0.2204	(22)

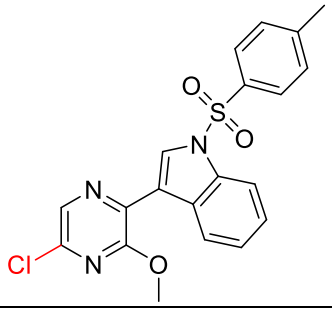		32.0	50.2	-26.3	3.14	0.2981	(30)
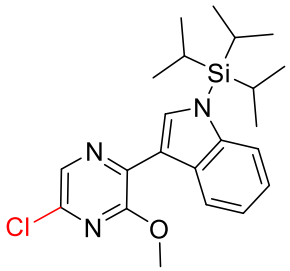		36.3	28.6	-43.0	3.14	0.2846	(30)
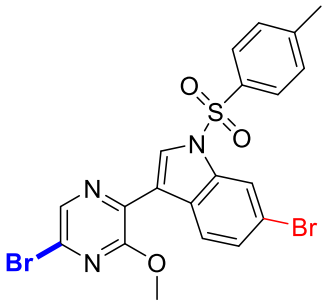	**blue**	14.3	57.9	-15.3	3.14	0.2205	(30)
	red	37.5	4.53	-7.58	0.00	0.2344	

References

(1) S. Sengmany, J. Lebre, E. Le Gall, E. Leonel, *Tetrahedron*, 2015, **71**, 4859-4867.

(2) L. Cui, Z. Zhang, X. Lu, B. Xiao, Y. Fu, *RSC Adv.*, 2016, **6**, 51932-51935.

(3) T. Taeufer, J. Pospech, *J. Org. Chem.*, 2020, **85**, 7097-7111.

(4) M. Uchiyama, Y. Kobayashi, T. Furuyama, S. Nakamura, Y. Kajihara, T. Miyoshi, T. Sakamoto, Y. Kondo, K. Morokuma, *J. Am. Chem. Soc.*, 2008, **130**, 472-480.

(5) B. Dogga, C. S. Ananda Kumar, J. T. Joseph, *Eur. J. Org. Chem.*, 2021, 309-313.

(6) T. Fantoni, S. Bernardoni, A. Mattellone, G. Martelli, L. Ferrazzano, P. Cantelmi, D. Corbisiero, A. Tolomelli, W. Cabri, F. Vacondio, F. Ferlenghi, M. Mor, A. Ricci, *ChemSusChem*, 2021, **14**, 2591-2600.

(7) C. A. Quesnelle, V. Snieckus, *Synthesis*, 2018, **50**, 4395-4412.

(8) Z. Zhu, Y. Gong, W. Tong, W. Xue, H. Gong, *Org. Lett.*, 2021, **23**, 2158–2163.

(9) F. Neese, F. Wennmohs, U. Becker, C. Riplinger, *J. Chem. Phys.*, 2020, **152**, 224108.

(10) T. Lu, F. Chen, F. *J. Comput. Chem.*, 2012, **33**, 580-592.

(11) T. Lu, F. Chen, *J. Mol. Graph. Model.*, 2012, **38**, 314-323.

(12) J. A. Hirsch, Table of Conformational Energies—1967. In Topics in Stereochemistry; John Wiley & Sons, Ltd, 1967; pp 199-222.

(13) H. E. Pence, A. Williams, *J. Chem. Educ.*, 2010, **87**, 1123-1124.

(14) M. D. Hanwell, D. E. Curtis, D. C. Lonie, T. Vandermeersch, E. Zurek, G. R. Hutchison, *J. Cheminform.*, 2012, ***4***, 17.

(15) J. Klein, H. Khartabil, J.-C. Boisson, J. Contreras-García, J.-P. Piquemal, E. Henon, *J. Phys. Chem. A*, 2020, **124**, 1850-1860.

(16) W. Humphrey, A. Dalke, K. Schulten, *J. Molec. Graphics*, 1996, **14**, 33-38.

(17) B. A. Anjali, C. H. Suresh, *ACS Omega*, 2017, **2**, 4196-4206.

(18) E. Paenurk, K. Kaupmees, D. Himmel, A. Kütt, I. Kaljurand, I. A. Koppel, I. Krossing, I. Leito, *Chem. Sci.*, 2017, **8**, 6964-6973.

(19) C. Hansch, A. Leo, R. W. Taft, *Chem. Rev.*, 1991, **91**, 165-195.

(20) B. U. W. Maes, S. Verbeeck, T. Verhelst, A. Ekomi, N. von Wolff, G. Lefàvre, E. A. Mitchell, A. Jutand, *Chem. Eur. J.*, 2015, **21**, 7858-7865.

(21) J. Almond-Thynne, D. C. Blakemore, D. C. Pryde, A. C. Spivey, *Chem. Sci.*, 2017, **8**, 40-62.

(22) C.-G. Yang, G. Liu, B. Jiang, *J. Org. Chem.*, 2002, **67**, 9392-9396.

(23) X. Dai, Y. Chen, S. Garrell, H. Liu, L.-K. Zhang, A. Palani, G. Hughes, R. Nargund, *J. Org. Chem.*, 2013, **78**, 7758-7763.

(24) W. Yang, Y. Wang, J. R. Corte, *Org. Lett.*, 2003, **5**, 3131-3134.

(25) E. Blaise, A. E. Kümmerle, H. Hammoud, J. X. de Araújo-Júnior, F. Bihel, J.-J. Bourguignon, M. Schmitt, *J. Org. Chem.*, 2014, **79**, 10311-10322.

(26) J. Ji, T. Li, W. H. Bunnelle, *Org. Lett.*, 2003, **5**, 4611-4614.

(27) M. H. Keylor, Z. L. Niemeyer, M. S. Sigman, K. L. Tan, *J. Am. Chem. Soc.*, 2017, **139**, 10613-10616.

(28) C. Sicre, J.-L. Alonso-Gómez, M. M. Cid, *Tetrahedron*, 2006, **62**, 11063-11072.

(29) N. W. J. Scott, M. J. Ford, N. Jeddi, A. Eyles, L. Simon, A. C. Whitwood, T. Tanner, C. E. Willans, I. J. S. Fairlamb, *J. Am. Chem. Soc.*, 2021, **143**, 9682-9693.

(30) N. K. Garg, R. Sarpong, B. M. Stoltz, *J. Am. Chem. Soc.*, 2002, **124**, 13179-13184.